

UNIVERSITY OF LJUBLJANA  
FACULTY OF MATHEMATICS AND PHYSICS  
DEPARTMENT OF PHYSICS

Klemen Čotar

**NASLOV DOKTORSKE DISERTACIJE V  
ANGLEŠKEM JEZIKU**

DOCTORAL THESIS

ADVISER: prof. dr. Tomaž Zwitter

Ljubljana, 2020



UNIVERZA V LJUBLJANI  
FAKULTETA ZA MATEMATIKO IN FIZIKO  
ODDELEK ZA FIZIKO

Klemen Čotar

**NASLOV DOKTORSKE DISERTACIJE V  
SLOVENSKEM JEZIKU**

DOKTORSKA DISERTACIJA

MENTOR: prof. dr. Tomaž Zwitter

Ljubljana, 2020



## **Zahvala**

Na tem mestu zapišite, komu se zahvaljujete za pomoč pri nastanku doktorske diplome.



## **Naslov v slovenskem jeziku**

### **IZVLEČEK**

Kratek izvleček v slovenskem jeziku, do 300 besed.

**Ključne besede:**

**PACS:**



## **Naslov v angleškem jeziku**

### **ABSTRACT**

Kratek izvleček v angleškem jeziku, do 300 besed.

**Keywords:**

**PACS:**



# Contents

<b>1</b>	<b>Introduction</b>	<b>13</b>
1.1	Open clusters in Gaia era	13
1.2	Chemical tagging - background	13
1.3	Chemical tagging - challenges	13
<b>2</b>	<b>Spectroscopic, photometric, and astrometric surveys</b>	<b>15</b>
2.1	Gaia	15
2.1.1	Photometry and astrometry	17
2.1.2	Spectroscopy	17
2.2	Gaia DR2	17
2.3	GALAH	20
2.3.1	Acquired spectra and target selection	20
2.3.2	Spectral reduction and parameters determination	21
2.4	Asiago	22
<b>3</b>	<b>Chemo-dynamic tracing of open cluster stars</b>	<b>25</b>
<b>4</b>	<b>Triple stars</b>	<b>27</b>
4.1	Abstract	27
4.2	Introduction	27
4.3	Data	28
4.4	Solar-like spectra	31
4.4.1	Candidate multiple systems	33
4.5	Single star models	34
4.5.1	Spectroscopic model	35
4.5.2	Photometric model	35
4.5.3	Limitations in the parameter space	36
4.6	Characterization of multiple system candidates	37
4.6.1	Fitting procedure	37
4.6.2	Photometric fitting - first step	38
4.6.3	Spectroscopic fitting - second step	40
4.6.4	Final fit - third step	41
4.6.5	Number of stellar components - final classification	41
4.6.6	Quality flags	42
4.7	Characterization of single star candidates	44
4.8	Orbital period constraints	44
4.8.1	Outer pair and <i>Gaia</i> angular resolution	45
4.8.2	Inner binary pair and formation of double lines in a spectrum	47
4.8.3	Multi-epoch radial velocities	49

---

4.9	Simulations and tests . . . . .	52
4.9.1	Radial velocity separation between components . . . . .	52
4.9.2	Analysis of synthetic multiple systems . . . . .	53
4.9.3	Triple stars across the H-R diagram . . . . .	54
4.9.4	Observational bias - Galaxia model . . . . .	57
4.10	Conclusions . . . . .	58
4.11	Table description and summary . . . . .	58
4.12	Additional figures . . . . .	61
<b>5</b>	<b>Peculiar stars . . . . .</b>	<b>67</b>
5.1	Abstract . . . . .	67
5.2	Introduction . . . . .	67
5.3	Data . . . . .	68
5.4	Detection procedure . . . . .	69
5.4.1	Supervised classification . . . . .	70
5.4.2	Unsupervised classification . . . . .	74
5.5	Candidate characteristics . . . . .	76
5.5.1	Radial velocity variations . . . . .	77
5.5.2	Stellar parameters . . . . .	78
5.5.3	S-process elements . . . . .	78
5.5.4	Lithium abundance . . . . .	80
5.5.5	Sub-classes . . . . .	80
5.5.6	Match with other catalogues . . . . .	81
5.6	Metal-poor candidates . . . . .	82
5.7	Follow-up observation . . . . .	86
5.8	Conclusions . . . . .	86
5.9	Table description . . . . .	88
<b>6</b>	<b>Conclusions . . . . .</b>	<b>95</b>
<b>Bibliography . . . . .</b>	<b>97</b>	
<b>Appendix A Naslov prvega dodatka . . . . .</b>	<b>117</b>	
<b>Razširjeni povzetek v slovenskem jeziku . . . . .</b>	<b>119</b>	

# Chapter 1

## Introduction

- 1.1 Open clusters in Gaia era
- 1.2 Chemical tagging - background
- 1.3 Chemical tagging - challenges



# Chapter 2

## Spectroscopic, photometric, and astrometric surveys

In the last few decades we are witnessing a fast and numerous shift from dedicated single object observations to massive all-sky surveys producing hundreds or even thousands of unbiased observations in a single telescope pointing. Along with the complexity of data acquisition and storage, new challenges and problems involving data reduction arose, requiring dedicated computer power to reduce acquired data. The reduction challenges span from timely, almost real-time reduction requirements, to complex, computationally demanding processes that try to take into account as many telescopically and observationally induced biases as possible. Some of those processes will be discussed in the following sections discussing a specific survey.

This thesis shows few cases of synergies of such vastly different data sets and at the same time points to a necessity of having knowledge about the automatic processing pipelines that produced final products, quite often blindly used by users.

The main source of data for our studies are the following three stellar surveys producing informations about the stars' brightness, composition, distance, kinematics and many additional parameters that can be inferred from the observed quantities.

### 2.1 Gaia

Gaia is the one-billion-star surveyor of the European Space Agency (ESA). It has been continuously scanning the sky since July 2014 from its designated location close to the second Lagrange point of the Sun-Earth/Moon system. Gaia's aim is to map the entire sky, down to magnitude  $\sim 20.7$ , and to collect micro-arcsecond-level astrometry and milli-magnitude-level photometry for the brightest 1,000+ million stars as well as medium-resolution spectroscopy for mainly radial-velocity determination of the brightest subset of  $\sim 150$  million objects.

The Gaia scanning of the sky is composed of two independent, superimposed motions: a rotation around the spacecraft spin axis with a period of 6 hours plus a slow, 63 day period precession of the spin axis around the Solar direction at a fixed Solar-aspect angle of  $45^\circ$ . Over the nominal five- year mission, Gaia has completed 29 of these precession periods, leading to an optimally uniform sky coverage with, on average,  $\sim 70$  astrometric and photometric transits across the focal plane (and  $\sim 40$  for the spectroscopic instrument). In the extended mission phase that started in July 2019, a similar scanning law is being employed but with a reversed precession

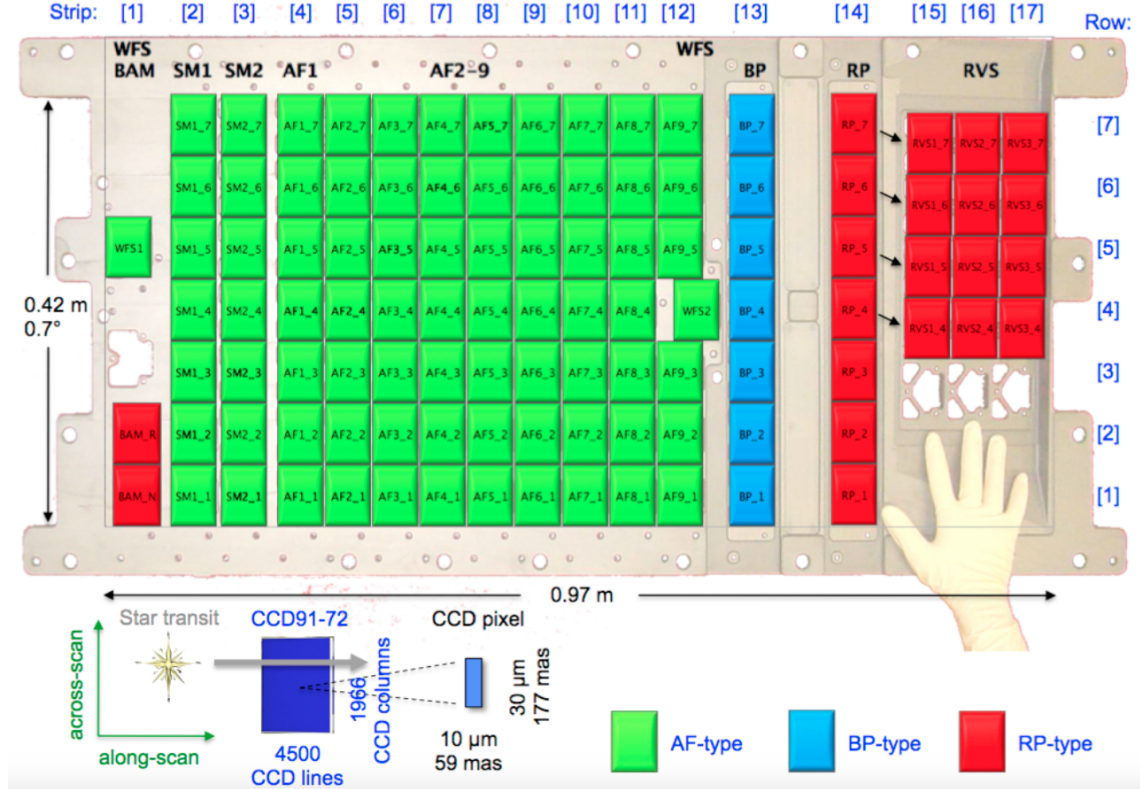


Figure 2.1: Size comparison and spatial arrangement of the CCD detectors in the Gaia focal plane. Image credit: Gaia Collaboration *et al.* [1].

Table 2.1: Past and future predicted release dates of Gaia data and products.

Release designation	Date
Gaia DR1	14 September 2016
Gaia DR2	25 April 2018
Gaia EDR3	3 <sup>rd</sup> quarter of 2020
Gaia DR3	2 <sup>nd</sup> half of 2021
Final release	not yet determined

direction during the first year. A passage of a star through the focal plane is called a field-of-view transit. During each transit, Gaia collects instantaneous, so-called epoch data of each object. Publication of all epoch data is scheduled (see Table 2.1 for the final data release).

As the spacecraft slowly rotates, observed stars traverse the Gaia focal plane equipped with 106 CCD detectors (show in Figure 2.1). Every star that gets observed therefore passes trough a sequence of those detectors who analyse a star in the given order:

### 2.1.1 Photometry and astrometry

The first array of CCDs that collects light from stars is a Sky Mapper (SM) that autonomously detect objects. Stars brighter than magnitude  $\sim 3$  are too bright to be detected automatically. The faint detection threshold is set at 20.7 magnitude in the Gaia G band but is not infinitely sharp due to on-the-fly magnitude estimation errors of the on-board software.

After the source detection, stars pass into the largest array of CCDs that is attributed to the Astrometric Field (AF). It collects the instantaneous positions and fluxes of all objects detected by the Sky Mapper as they traverse along the field. Astrometric measurements are made in a white-light bandpass, covering the range from 3300 to 10500 Å, which is referred to as the Gaia G band.

The last spectro-photometric measurements are thereafter performed by two low dispersion detectors that are measuring precise fluxes in a number of narrow-pass sub-bands of previously mentioned wide-pass G band. The Blue Photometer (BP) collects low resolution spectra of all objects over the wavelength range from 3300 to 6800 Å. The integrated magnitude is referred to as the  $G_{BP}$  or BP magnitude. The Red Photometer (RP) collects low-resolution spectra of all objects over the wavelength range from 6300 to 10500 Å. The integrated magnitude is referred to as the  $G_{RP}$  or RP magnitude.

### 2.1.2 Spectroscopy

A final measurement performed by the spacecraft is spectroscopy over the whole observed field of the sky. The integral-field Radial Velocity Spectrometer (RVS) [2] collects medium-resolution spectra (spectral resolving power ( $R$ )  $\sim 11,700$ ) over the wavelength range from 8450 to 8720 Å, for all objects brighter than magnitude  $\sim 16$  in this bandpass. The location of the pass-band is selected to cover the ionised calcium (CaII) triplet with a prominent absorption features over a large temperature range of stars and can therefore be used to determine radial velocity of spectrally diverse stars. The integrated magnitude in the RVS bandpass is referred to as the  $G_{RVS}$  magnitude. The RVS has a reduced field of view orthogonal to the scan direction such that fewer observations up to the RVS limiting magnitude are collected compared to photometric fields in a ratio of 4:7.

## 2.2 Gaia DR2

The second data release of Gaia data (Gaia DR2) was heavily used during the production of this thesis, therefore it requires detailed description of provided tables, its use and potential problems. The release set is far from complete and similar to the final release, but on the other hand provides an unprecedented set of homogeneously acquired and reduced stellar informations newer seen before. Visual and numerical representation of the specific stellar product is given in Figure 2.2. Gaia DR2 is based on data collected by the spacecraft between 25 July 2014 and 23 May 2016, spanning a period of 22 months.

Along the calibrated raw measurements, Gaia Data Processing and Analysis Consortium (DPAC) provides numerous parameters and properties of stars, pre-selected Solar system bodies and quasars that can be used and explored by users.



Figure 2.2: Visual and numerical representation of Gaia DR2 stellar content. Image credit: ESA, CC BY-SA 3.0 IGO.

Among them we can find:

- **Astrometric set** consisting of partial 2-parameter (limited to celestial positions  $\alpha$  and  $\delta$ ) and full 5-parameter astrometric solution with addition of including parallax, and proper motion. The 2-parameter sources are typically faint (with about half of them at magnitude  $G > 20.6$ ), have very few observations (less than five as required for full solution), or very poorly fit the five-parameter astrometric model. All sources fainter than magnitude  $G = 21$  have only positional information. In the current data release all stars are still treated as single during astrometric fit, which could significantly influence solutions in the case of multiple fast moving sources contributing to the position of an observed photocentre. The Gaia coordinate reference frame is aligned with the International Celestial Reference Frame (ICRF) using positions of extragalactic sources such as quasars [3]. After the initial release, it was determined that the quality of an astrometric fit is best described by the renormalised astrometric chi-square (RUWE) [4]. Further details about astrometric processing and validation are given in Lindegren *et al.* [5], Luri *et al.* [6].
- **Photometric data set** contains the broad band photometry in the G,  $G_{BP}$ , and  $G_{RP}$  bands, giving us colour information for Gaia DR2 sources that were observed at least twice. The mean value of the G-band fluxes is reported for all sources while colour information (BP and RP) is available for about 80% of them. The integrated colour information suffers from strong systematic effects at the faint end of the survey ( $G > 19$ ), in crowded regions, and near bright stars. In the case when measured fluxes are inconsistent between the

$G$  and the  $G_{BP}$  and  $G_{RP}$  bands (sum of the later two is significantly larger than  $G$  measurement) a warning is raised. A quantitative index of this effect is provided in the numerical form as *flux excess factor*. Further details about processing and photometry validation are given in Evans *et al.* [7], Riello *et al.* [8].

- **Radial velocity measurements** indicate stellar median radial velocity, averaged over the first 22 months of the observations. Therefore stellar multiplicity and their orbital motion can not be determined from current data. Velocities are provided for sources which are brighter than magnitude 12 in the  $G_{RVS}$  photometric band. Because of used set of spectral templates during radial velocity determination, velocities are reported only for stars with effective temperatures in the range between 3550 and 6900 K (referring to the effective temperature of a used template and not an actual effective temperature of a star). By the RVS pipeline design, determined absolute radial velocity are limited to  $1000 \text{ km s}^{-1}$ . The uncertainties of the radial velocities at the faint end depend on stellar effective temperature and range from  $1.4 \text{ km s}^{-1}$  for cooler to  $3.6 \text{ km s}^{-1}$  for hotter stars. The zero-point of the RVS velocities was determined using a comprehensive set of standard stars with numerous dedicated, precise and temporally spread radial velocity measurements [9]. Further processing details of RVS data are given in Sartoretti *et al.* [10].
- **Stellar variability data set** consists of sources that were firmly identified as variable (based on at least two observations of the two Gaia telescopes). The final number still represents only a small subset of the total amount of variables expected in the Gaia survey. The sources were classified into the following nine categories based on their light curves: RR Lyrae (anomalous RRd, RRd, RRab, RRc), long period variables (Mira type and Semi-Regulars), Cepheids (anomalous Cepheids, classical Cepheids, type-II Cepheids),  $\delta$  Scuti and SX Phoenicis stars. If a star had 12 or more observations its light curve was analysed in detail. They are designated as specific object studies (SOS) and consist of variables of the type Cepheid and RR Lyrae, long period variables, short time scale variables, and rotational modulation variables. Full details on the variable star processing, results and their validation are given in Holl *et al.* [11], Mowlavi *et al.* [12], Molnár *et al.* [13], Clementini *et al.* [14].
- **Astrophysical parameters** derived by the astrophysical parameter inference system in the Gaia data processing (Apsis) include estimates of  $T_{\text{eff}}$  extinction  $A_G$  and reddening  $E(G_{BP} - G_{RP})$ , radius, and luminosity for stars brighter than magnitude  $G = 17$ . Values of  $T_{\text{eff}}$  are reported only over the temperature range between 3000 and 10,000 K that is induced by the training set for the algorithm responsible for the  $T_{\text{eff}}$  estimation. Estimates of the other astrophysical parameters are published for about half of the sources with determined  $T_{\text{eff}}$ . As the processing pipeline was performed individually for every object and with a limited set of input data (three Gaia photometric bands and parallax) some errors are expected because of high degeneracy between determined parameters. If a star is located far from expected isochrones used in the processing, extinction becomes overestimated. Full details of the astrophysical parameter processing and result validation are described in Andrae

*et al.* [15].

- **Solar system objects** (SSO) data set provides epoch astrometry and unfiltered G photometry for a pre-selected list of 14,099 known minor bodies in the solar system that are numbered in the Minor Planet Center repository. Each time a given SSO enters field of view of Gaia telescopes celestial positions are recorded as seen from the spacecraft. The data set and its production are thoroughly described in Gaia Collaboration *et al.* [16].

The above sections are partially adapted and summarized from Gaia Collaboration *et al.* [1, 17], Gaia Helpdesk [18].

## 2.3 GALAH

The GALactic Archaeology with HERMES (GALAH) [19] is an ongoing spectroscopic survey that aims to unveil the Milky Way’s formation history by studying the detailed chemical composition of observed stars. Fossil remnants, which have been disrupted during the formation and are now dispersed around the Galaxy, are tough to have conserved the initial chemical signature of individual galactic components. It is essential to disentangle their formation location and migration history in order to explain current stellar populations. This can be achieved through the technique of chemical tagging [20] that promises identification of old dispersed fossil remnants based on their unique abundance patterns over numerous chemical elements. The GALAH aims to achieve this by measuring up to 31 elemental abundances (from 7 independent element groups with different physical origin) individually in every acquired spectrum.

The GALAH survey was the main driver for the construction of the High Efficiency and Resolution Multi-Element Spectrograph (HERMES) [21, 22], a multi-fibre spectrograph mounted on the 3.9-metre Anglo-Australian Telescope (AAT) situated at the Siding Spring Observatory, Australia. The spectrograph has a resolving power of  $R \sim 28,000$  (or  $R \sim 45,000$  when slit mask is used) and covers four separately acquired wavelength ranges ( $4713 - 4903 \text{ \AA}$ ,  $5648 - 5873 \text{ \AA}$ ,  $6478 - 6737 \text{ \AA}$ , and  $7585 - 7887 \text{ \AA}$ ), together covering approximately  $1000 \text{ \AA}$ , including the  $\text{H}\alpha$  and  $\text{H}\beta$  lines. The ranges are frequently referred to as blue, green, red and near-infrared spectral arms. This configuration can simultaneously record spectra from up to 392 fibres distributed over a  $2^\circ$  diameter field of the night sky, with an additional 8 fibres used for the telescope guiding. The spectrograph can typically achieve a signal to noise ratio (SNR)  $\sim 100$  per resolution element at magnitude  $V=14$  in the red arm during a 1-hour long exposure.

### 2.3.1 Acquired spectra and target selection

The spectroscopic data used during the production of this thesis were taken from the pilot survey, the main GALAH survey [19], the K2-HERMES survey [23], the TESS-HERMES survey [24], and special dedicated the HEMRES open clusters (De Silva et al. in preparation) and the HERMES Orion star forming region (Kos et al. in preparation) surveys. Together they form a dataset of 669,845 successfully reduced stellar spectra, of which a small fraction belongs to a repeated observations.

All acquired spectra are homogeneously reduced to one dimensional spectrum, normalised and shifted to stellar reference frame (detailed description in Kos *et al.* [25]). Combination of those surveys produces increased number of spectra compared to the main GALAH survey, but at the same time breaks rule of a simple unbiased selection function (Sharma *et al.* in preparation) that is desired for population studies and easier comparison with synthetic galactic models.

The original selection function of the main GALAH survey is separated into two magnitude limited filed selections - bright ( $10 < V < 12$ ) and normal ( $12 < V < 14$ ) fields whose target selection is colour independent. Used V magnitude is inferred from magnitudes measured by the Two Micron All-Sky Survey (2MASS) [26] whose photometric bands are shifted into infra-red spectral region. Because of that, some, especially peculiar and variable stars, might have erroneous estimation of V magnitude leading to an underexposure or excessive spectral crosstalk. Because of expected crowding problems (projected diameter of used optical fiber on the sky is equal to  $2''$ ) observed stars are located at higher Galactic latitudes ( $|b| > 10^\circ$ ) where density of stars is lower. Additional surveys sometimes break those rules by selecting fainter/dimmer stars, going closer to the Galactic plane, employ colour cuts, or favor interesting preselected stars such as K2 [27] targets, TESS [28] targets and cluster members. Therefore some care is needed when trying to infer global stellar or galactic properties based on such inhomogeneous selection criteria.

### 2.3.2 Spectral reduction and parameters determination

The first step after recording spectra in the form of a 2D image is their extraction to 1D spectrum. The procedure, extensively documented by Kos *et al.* [25], consist of the following steps: raw image cosmetic corrections, spectral tracing, optical aberrations correction, scattered light and apertures coss-talk removal, wavelength calibration, sky subtraction, and telluric absorption removal. After reduction, spectra are normalised and shifted into their rest frame by cross-correlating them with a set of 15 AMBRE model spectra [29]. Stellar atmospheric parameters and individual elemental abundances derived from normalised spectra, acquired by different surveys, are analysed with the same procedure that slowly evolved and improved during the course of the GALAH survey. The three most important milestones in an ongoing process are:

- The initial stellar parameters ( $T_{\text{eff}}$ ,  $\log g$ , and  $[\text{Fe}/\text{H}]$ ), accompanying the first GALAH data release (**GALAH DR1**), were derived as a global fit (all arms at the same time) of the observed spectra to a grid of 16,783 AMBRE spectra [29], which were convolved down to the average resolution of individual CCD. The aim of this procedure was to provide indicative stellar parameters, which could be used as a first initial guess to help speed up a more complex stellar parameters and abundance pipeline.
- The parameters (with extension to  $v \sin i$ ,  $v_{\text{mic}}$ , and  $A_{K_S}$ ) and up to 23 elemental abundances, released as part of the **GALAH DR2** [72], were produced using a multi-step data driven approach. The complete analysis depended on a set of 10,605 spectra that were selected in a such way to span a large portion of the parameter and did not contain any peculiar star, especially binary and emission line spectra. Selected spectra were analysed using a physics-driven

spectrum synthesis code Spectra Made Easy (*SME*) [30, 31] that performs spectrum synthesis for 1D stellar atmospheres models. In the case of DR2, it consist of MARCS theoretical 1D hydrostatic models [? ] under the assumption of local thermodynamic equilibrium (LTE) for majority of elements. Only several key elements (Li, O, Na, Mg, Al, Si, and Fe) were analysed using non-LTE line formation.

To propagate the parameter and abundance results of the training set to the whole survey, *The Cannon* [71] generative data-driven approach was used. It adopts a simple quadratic model which uses stellar parameters to describes observed flux of a given spectrum. Independent model is build for every spectrum wavelength pixels. To train *The Cannon* model all spectra in the training set were interpolated to a common wavelength grid. After the training is performed, model was inverted to produce parameters and abundances for every observed spectrum by fitting it to internal generative spectrum produced by *The Cannon*. Further details of the described process are given in Buder *et al.* [72].

- Not relying only on the GALAH spectral information, but including *Gaia* parallax, colour, and absolute magnitude, additional constrains and priors can be used to infer stellar parameters. Adaption of *SME* software thoroughly described in (???????) used those additional information to produce **GALAH DR3** data set. Unlike in DR2, no data-driven methodology was used to produce stellar parameters and abundances as *SME* was run for every individual spectrum.

The dataset includes .....

## 2.4 Asiago

Vastly different from the previous two massive all-sky surveys, telescopes at the Asiago site are mainly used for dedicated observations or monitoring of previously selected targets, whose observational and astrophysical potential was identified from all-sky surveys. During our stay at the Asiago observatory, that usually lasted for four consecutive bright nights every month, we used 1.82 m Copernico telescope located on top of the nearby hill Mount Ekar (Asiago, Italy - altitude of 1,366 m).

All our observations were performed by the Echelle spectrograph that is mounted on the telescope on days around the full Moon when quality and deepness of photometric observations is heavily reduced. Design of the Echelle instrument and its slit length enables observer to observe only one star a time. Obtained spectra have a resolving power of  $R \sim 20,000$  and a wide span of wavelengths between 3600 and 7400 Å. They are divided into 30 orders who partially overlap with succeeding and preceding order, providing an undisturbed coverage of observed wavelengths. Acquired spectra are recorded by Andor CCD with the size of  $2048 \times 2048$  pixels. This setup enables us to capture spectra of stars with magnitudes  $V < 10$  at high SNR with reasonable exposure time (less than 1 hour per spectrum). Because of the mechanical limitation, observed stars must be positioned at least  $15^\circ$  above the local horizon. At those low altitudes, only the brightest stars are reasonable to be observed because of strong atmospheric attenuation.

Combining location of the observatory and above observational limitations with the fact that our interesting stars were selected from the GALAH survey, highly reduces the number of potentially observable objects. To reduce the atmospheric effect effects, we only observed stars which rose at least  $30^\circ$  above the local horizon that is equal to having right ascension above  $000000^\circ$ . As described in more detail below, we used additional Asiago observations to inspect spectroscopic features not accessible by the GALAH spectra and to prolong radial velocity time series of possible multiple stars who could show signs of radial velocity changes not detectable by a single epoch GALAH spectrum.

Additionally to our program observations, we also contributed spectroscopic observations that resulted in published astronomer's telegrams [32] and scientific papers [33].



# Chapter 3

## Chemo-dynamic tracing of open cluster stars



# Chapter 4

## Triple stars

### 4.1 Abstract

The latest *Gaia* data release enables us to accurately identify stars that are more luminous than would be expected on the basis of their spectral type and distance. During an investigation of the 329 best Solar twin candidates uncovered among the spectra acquired by the GALAH survey, we identified 64 such over-luminous stars. In order to investigate their exact composition, we developed a data-driven methodology that can generate a synthetic photometric signature and spectrum of a single star. By combining multiple such synthetic stars into an unresolved binary or triple system and comparing the results to the actual photometric and spectroscopic observations, we uncovered 6 definitive triple stellar system candidates and an additional 14 potential candidates whose combined spectrum mimics the Solar spectrum. Considering the volume correction factor for a magnitude limited survey, the fraction of probable unresolved triple stars with long orbital periods is  $\sim 2\%$ . Possible orbital configurations of the candidates were investigated using the selection and observational limits. To validate the discovered multiplicity fraction, the same procedure was used to evaluate the multiplicity fraction of other stellar types.

### 4.2 Introduction

The investigation of Solar-type stars in the Solar neighbourhood has revealed that around half of them are found in binary or more complex stellar systems [34, 35, 36]. Of all multiple systems, about 13 % are part of higher-order hierarchical systems [34, 37]. Beyond the Solar neighbourhood, the angular separation between members of such multiple star systems becomes too small for their components to be spatially resolvable in the sky. As a result, all stellar components contribute to the light observed by spectroscopic, photometric, and astrometric surveys. It has been suggested that the population of binaries in the field could be even higher than in the Solar neighbourhood [38], therefore a combination of multiple complementary approaches must be used to detect and analyse multiple stellar systems with different properties [36].

If the orbital period of such a system is relatively short, with high orbital velocities, it can be spectroscopically identified as a multiple system in two ways. When the components are of comparable luminosities, the effect of multiple absorption

lines can be observed in the system's spectrum. Such an object is also known as a double-lined binary (SB2) system [39, 40, 41, 42]. By contrast, a single-lined binary (SB1) system does not show the same effect, as the secondary component is too faint to significantly contribute to the observables. Short period SB1 systems can be identified from the periodic radial velocity variations if multi-epoch spectroscopy is available [43, 44, 45, 46, 47]. Other extrema are very wide binaries [48, 49, 50, 51, 52, 53, 54], and co-moving pairs [55, 56] that can only be identified by their spatial proximity and common velocity vector.

Duchêne and Kraus [35] summarized that the majority of Solar-type stars are part of binary systems with periods of hundreds to thousands of years, whose period distribution reaches a maximum at  $\log(P) \approx 5$ , for  $P$  measured in days. Because of the wide separation and long orbital periods of the components in such a scenario, the radial velocity variations will have both low amplitude and long period. This makes them challenging to detect in large-scale spectroscopic surveys, which typically last for less than a decade, and have a low number of revisits. A spectrum of such a binary or triple still contains a spectroscopic signature of all members, and those contributions can be disentangled into individual components [57, 58]. Such a decomposition is easier when a binary consists of spectrally different stars [59, 60, 61, 62, 63], but becomes much harder or near-impossible when the composite spectrum consists of contribution from near-identical stars whose individual radial velocities are almost identical [64]. In that case, additional photometric and distance measurement have to be used to constrain possible combinations [65]. If spectroscopic data are not available, determination of multiples can be attempted purely on the basis of photometric information [65, 66, 67, 68], but such approaches are limited to certain stellar types, and yield results that might be polluted with young pre-main-sequence stars [69].

In the scope of the GALactic Archaeology with HERMES (GALAH) survey, most stars are observed at only one epoch, limiting the number of available data points that can be used to identify and characterize unresolved spectroscopic binaries. For this study, GALAH observations were complemented by multiple photometric surveys presented in Section 5.3. Both spectroscopic (Section 4.5.1) and photometric (Section 4.5.2) observations were used to create data-driven models of a single star. Those models were used to analyse Solar twin candidates detected amongst the GALAH spectra (Section 4.4). Sections 4.6 and 4.7 describe the employed fitting procedure that was used to determine multiplicity and physical parameters of the twin systems. In Section 4.8 we determine constraints on orbital periods of the detected triple candidates. Constraints are imposed using the observational limits and simulations described in Section 4.9, where a population bias introduced by the magnitude-limited survey is assessed in Section 4.9.4. Concluding Section 4.10 summarises the results and introduces additional approaches that could be used to verify the results.

## 4.3 Data

In this work, we analyse a set of high-resolution stellar spectra that were acquired by the High Efficiency and Resolution Multi-Element Spectrograph [HERMES, 21, 22], a multi-fibre spectrograph mounted on the 3.9-metre Anglo-Australian Telescope (AAT). The spectrograph has a resolving power of  $R \sim 28,000$  and covers four

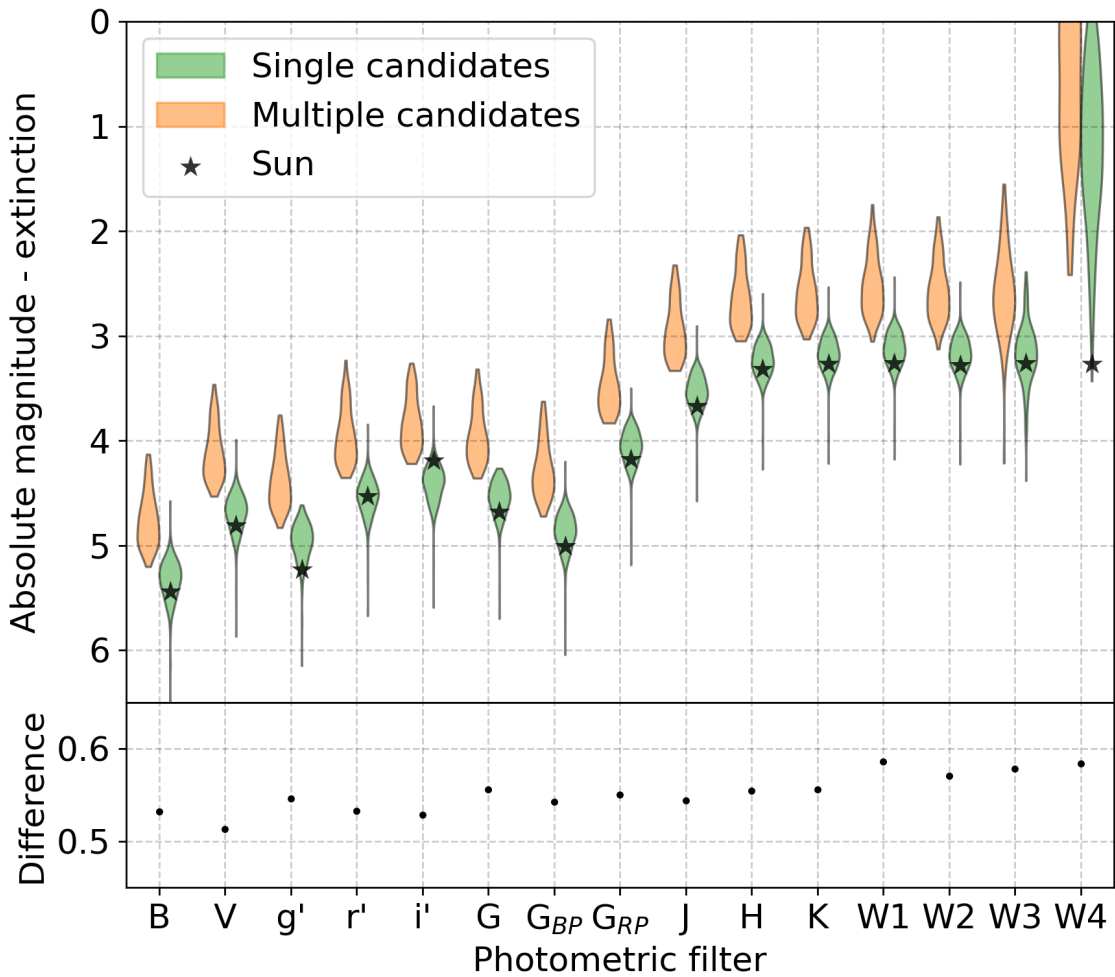


Figure 4.1: Violin density plots showing the distribution of extinction-corrected absolute magnitudes in multiple photometric systems. Separate distributions are given for stars that we considered as single and multiple in our analysis. Star symbols indicate absolute magnitude of the Sun [70]. The bottom panel shows a difference between the median magnitudes of both distributions.

wavelength ranges ( $4713 - 4903 \text{ \AA}$ ,  $5648 - 5873 \text{ \AA}$ ,  $6478 - 6737 \text{ \AA}$ , and  $7585 - 7887 \text{ \AA}$ ), frequently also referred to as spectral arms. Observations used in this study have been taken from multiple observing programmes that make use of HERMES spectrograph: the main GALAH survey [19], the K2-HERMES survey [23], and the TESS-HERMES survey [24]. Those observing programmes mostly observe stars at higher Galactic latitudes ( $|b| > 10^\circ$ ), employ different selection functions, but share the same observing procedures, reduction, and analysis pipeline [internal version 5.3, 25]. All three programmes are magnitude-limited, with no colour cuts (except the K2-HERMES survey), and observations predominantly fall in the V magnitude range between 12 and 14. This leads to an unbiased sample of mostly southern stars that can be used for different population studies, such as multiple stellar systems in our case. Additionally, stellar atmospheric parameters and individual abundances derived from spectra acquired during different observing programmes are analysed with the same *The Cannon* procedure [internal version 182112 that uses parallax information to infer  $\log g$  of a star, 71, 72], so they are inter-comparable. *The Cannon* is a data-driven interpolation approach trained on a set of stellar spectra that span the majority of the stellar parameter space [for details, see 72]. Whenever we refer to valid or unflagged stellar parameters in the text, only stars with the quality flag `flag_cannon` equal to 0 were selected.

With the latest *Gaia* DR2 release [1, 17], the determination of distance for stars within a few kpc away from the Sun becomes straightforward, and the derived distances are accurate to a few percent. Along with the measurements of parallax and proper motion, stellar magnitudes in up to three photometric bands ( $G$ ,  $G_{BP}$  and  $G_{RP}$ ) are provided. Coupling those two measurements together, we can determine the absolute magnitude and luminosity of a star. This can be done for the majority of stars observed in the scope of the GALAH survey as more than 99 % of them can be matched with sources in *Gaia* DR2. Although the uncertainty in *Gaia* mean radial velocities is much larger than those from GALAH [73], especially at its faint limit, they can still be used in the multi-epoch analysis (Section 4.8.3) to determine the lower boundary of its variability.

Because observations of both surveys were acquired at approximately the same epoch ranges, wide binaries with long orbital periods would show little variability in their projected velocities. Observational time-series were therefore extended into the past with the latest data release from The Radial Velocity Experiment [RAVE DR5, 74] that also surveyed the southern part of the sky. More recent spectra of accessible (stars' declination  $> -25^\circ$  and  $G$  magnitude  $< 13.5$ ) multiple candidates were acquired by the high-resolution Echelle spectrograph (with the resolving power  $R \sim 20,000$ ) mounted on the 1.82-m Copernico telescope located at Cima Ekar in Asiago, Italy. As this telescope is located in a northern observatory, we were able to observe only a limited number of stars. Every observation consisted of two half-hour long exposures that were fully reduced, shifted to the heliocentric frame, combined together, and normalized. The system's radial velocity was determined by cross-correlating the observed spectrum with that of the Sun. Data from those two additional spectroscopic surveys enabled us to further constrain the variability of the analysed systems.

For a broader wavelength coverage, additional photometric data were taken from three large all-sky surveys. In the visual part of the spectrum we rely on the AAVSO Photometric All-Sky Survey [APASS, 75] B, V,  $g'$ ,  $r'$ ,  $i'$  bands that are supplemented

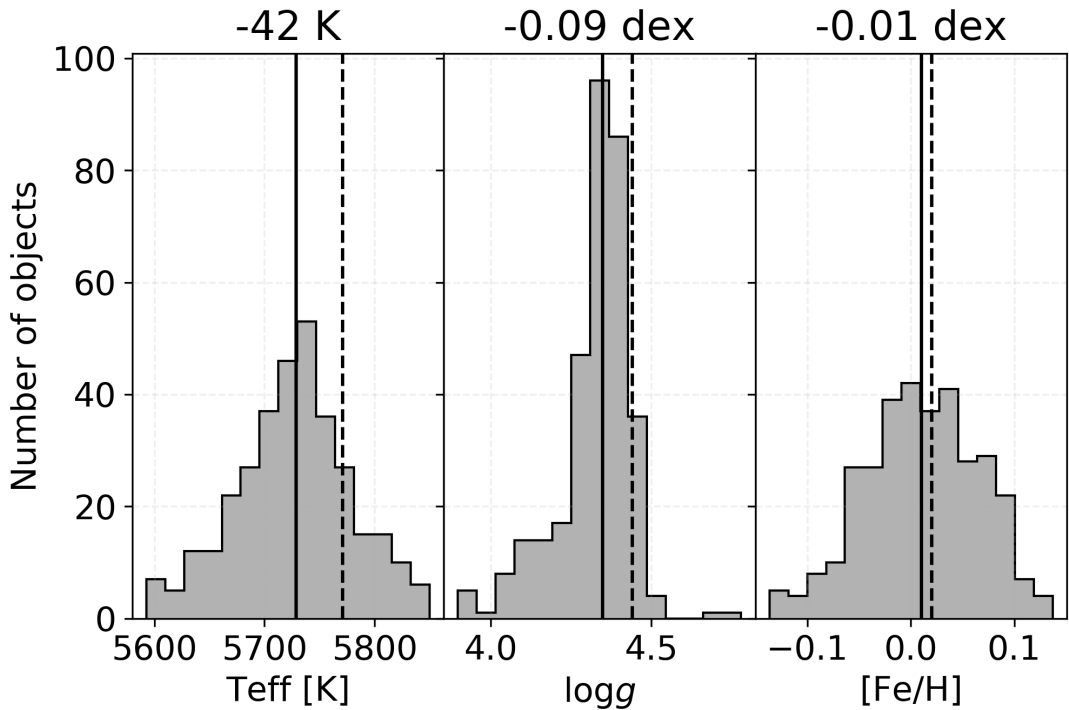


Figure 4.2: Distribution of physical parameters for discovered Solar twin candidates. Values above the plots represent difference between median of the distribution (solid vertical line) and actual Solar values (dashed vertical line).

by the Two Micron All-Sky Survey [2MASS, 26] J, H,  $K_S$  bands, and the Wide-field Infrared Survey Explorer [WISE, 76] W1, W2 bands. All of those surveys were matched with the GALAH targets, which resulted in up to 13 photometric observations per star. Photometric values and their uncertainties were taken as published in these catalogues, ignoring any specific quality flags. During the initial investigation of their usefulness, WISE W3, and W4 bands proved to be unreliable for our application and were therefore removed from further use. The main reason for their removal is a large scatter in magnitude measurements of similar stars and a strong overlap between single and multiple stars evident in Figure 4.1.

## 4.4 Solar-like spectra

The selection of the most probable Solar twin candidates observed in the scope of the GALAH survey was performed purely on the basis of spectral comparison using the Canberra distance metric [77]. It is defined as

$$distance_{Canberra}(f_\odot, f_{obs}) = \sum_{\lambda} \frac{|f_{\odot,\lambda} - f_{obs,\lambda}|}{|f_{\odot,\lambda}| + |f_{obs,\lambda}|}, \quad (4.1)$$

where  $f_\odot$  is the reference Solar spectrum and  $f_{obs}$  observed spectrum. This avoided the need for prior knowledge about the physical parameters of the considered stars. Observed spectra were compared with reference twilight Solar spectrum that was acquired by the same spectrograph. The comparison was done in two steps. First, the

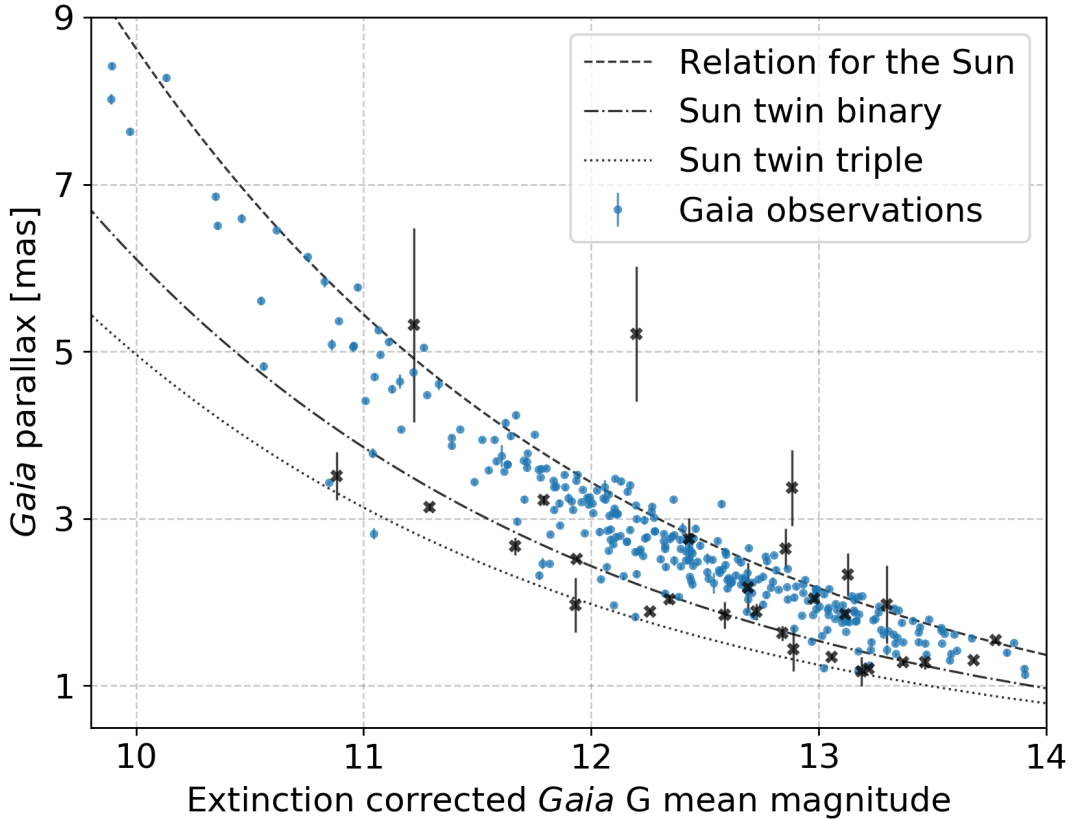


Figure 4.3: Parallax versus measured apparent *Gaia* G magnitude for our Solar twin candidates. Stars marked with black crosses have large normalised astrometric uncertainties ( $\text{RUWE} > 1.4$ ) which may lead to wrongly determined distance and consequently multiplicity results. The dashed line represents a theoretical absolute magnitude of the Sun as it would be observed at different parallaxes. Similarly, the relation for a binary and a triple system composed of multiple Solar twins are plotted with the dash-dotted and dotted line.

observed spectra were compared arm by arm, where only 7 % of the best matching candidates were selected for every HERMES arm. The selection does not consist of only one hard threshold on spectral similarity, but it varies as a power law of spectral SNR. Larger discrepancies between spectra are therefore allowed for spectra with low SNR. The final selection consisted of a set of stars whose spectra were adequately similar to the Solar spectrum in every arm. Further processing consisted of modelling the spectral noise and the comparison of individual chemical abundances. For details about spectral comparison and Solar twin determination see Čotar et al. (in preparation). The parameter distribution for the selected set of objects is presented in Figure 4.2. As the computation of  $\log g$  uses prior knowledge about the absolute magnitude of a star, lower  $\log g$  values are attributed to objects that exhibit excess luminosity.

### 4.4.1 Candidate multiple systems

Among the determined Solar twin candidates, we noticed a photometric trend that is inconsistent with the distance of an object that resembles the Sun. Solar twins, mimicking the observed Solar spectrum, should also be similar to it in all other observables such as luminosity, effective temperature, surface gravity, chemical composition and absolute magnitude. Plotting their apparent magnitude against *Gaia* parallax measurement (Figure 4.3), all of the detected stars should lie near or on the theoretical line, describing the same relation for the Sun observed at different parallaxes. As the magnitude of the Sun is not directly measured by the *Gaia* or determined by the *Gaia* team, we computed its absolute magnitude using the relations published by Evans *et al.* [78] that connect the *Gaia* photometric system with other photometric systems. The reference Solar magnitudes (in multiple filters) that were used in the computation were taken from Willmer [70]. The resulting absolute G magnitude of the Sun is  $4.68 \pm 0.02$ , where the uncertainty comes from the use of multiple relations. This value also coincides with the synthetic *Gaia* photometry produced by Casagrande and Vandenberg [79], who determined magnitude of the Sun to be  $M_{G,\odot} = 4.67$ .

Within our sample of the probable Solar twins, we identified 64 stars that show signs of being too bright at a given parallax. In Figure 4.3 they are noticeable as a sequence of data points that lie below the theoretical line and are parallel to it. Another even more obvious indication of their excess luminosity is given by the colour-magnitude diagram in Figure 4.4. There, the same group of stars is brighter by  $\sim 0.7$  magnitude when comparing stars with the same colour index. As both groups of stars are visually separable, the multiple stellar candidates can easily be isolated by selecting objects with extinction corrected absolute G magnitude above the binary limit line shown in Figure 4.4. To compute the absolute magnitudes, we used the distance to stars inferred by the Bayesian approach that takes into account the distribution of stars in the Galaxy [80]. As the reddening published along the *Gaia* DR2 [15] could be wrong for stars located away from the used set of isochrones, we took the information about the reddening at specific sky locations and distances from the all-sky three-dimensional dust map produced by Capitanio *et al.* [81]. To infer a band dependent extinction from the acquired reddening, a reddening coefficient ( $R$ ) was used. The values of  $R$ , considering the extinction law  $R_V = 3.1$ , were taken from the tabulated results published in Schlafly and Finkbeiner [82].

To determine the limiting threshold between single and multiple candidates, we first fit a linear representation of the main sequence to the median of the absolute magnitudes distribution in the 0.02 mag wide colour bins. The lower limit for the binaries was placed 0.25 mag above the fitted line.

Confirmation that this extra flux could be contributed by the unseen companion also comes from other photometric systems, where the distribution of absolute magnitudes for both groups is shown in Figure 4.1. On average, multiple candidates are brighter by  $\sim 0.55$  magnitude in every considered band. For an identical binary system, a measured magnitude excess would be 0.75, and 1.2 for a triple system. As the observed difference is not constant in every band, as would be expected for a system composed of identical stars, we expect some differences in parameters between the components of the system. This can be said under the assumption that all considered photometric measurements were performed at the same time. Of course, that is not exactly true in our case as the acquisition time between different ph-

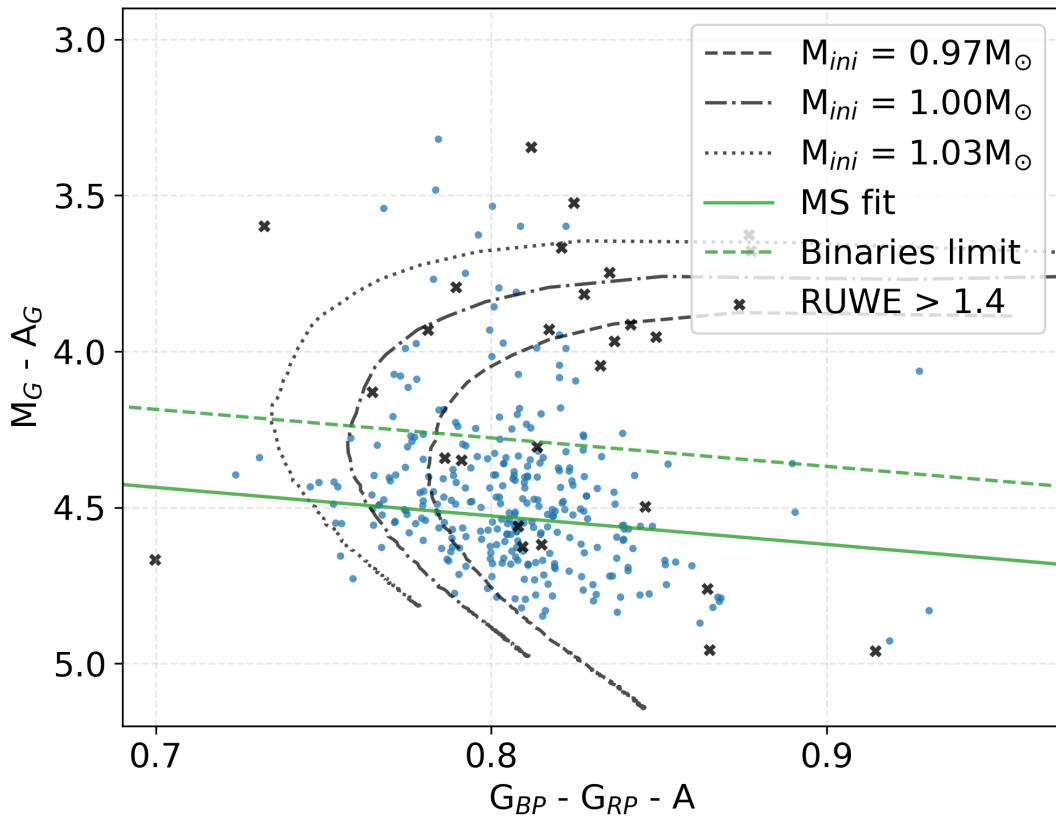


Figure 4.4: *Gaia* extinction corrected absolute G magnitude and colour index computed from  $G_{BP}$ , and  $G_{RP}$  bands. Stars marked with black crosses have large normalised astrometric uncertainty ( $\text{RUWE} > 1.4$ ). The green dashed line represents a threshold that was used as a delimiter between objects treated as multiple and single stars. Overlaid evolutionary tracks, constructed from the PARSEC isochrones [83], represent an evolution of stars with Solar-like initial mass  $M_{ini}$  and metallicity  $[\text{M}/\text{H}] = 0$  for stellar ages between 0.1 and 12 Gyr.

tometric surveys can vary by a few to 10 years. As the Sun-like stars are normal, low activity stars, this effect is most probably negligible, but events like occultations between the stars in the system can still occur.

## 4.5 Single star models

Once the selection of interesting stars was performed, we began with the analysis of their possible multiplicity. Our procedure for the analysis of suspected multiple stellar systems is based on spectroscopic and photometric data-driven single star models that were constructed from observations taken from multiple large sky surveys. With this approach, we exclude assumptions about stellar properties and populations that are usually used to generate synthetic data. In this section, we describe approaches that were used to create those models.

### 4.5.1 Spectroscopic model

Every stellar spectrum can be largely described using four basic physical stellar parameters:  $T_{\text{eff}}$ ,  $\log g$ , chemical composition, and  $v \sin i$ . To construct a model that would be able to recreate a spectrum corresponding to any conceivable combination of those parameters, we used a data-driven approach named *The Cannon*. The model was trained on a set of normalised GALAH spectra that meet the following criteria: the spectrum must not be flagged as peculiar [84], have a signal to noise ratio (SNR) per resolution element in the green arm  $> 20$ , does not contain any monitored reduction problems and have valid *The Cannon* stellar parameters. Additionally, we limited our set to main sequence dwarf stars (below the arbitrarily defined line shown in Figure 4.5) as giants are not considered for our analysis. Additionally, the decision not to consider giants was taken as a result of the fact that accurate modelling of their spectra requires information about their luminosity. It should be noted that the application of these limits does not ensure that our training set is completely free from spectra of unresolved (or even clearly resolved SB2 binaries), as would be desired in the case of an ideal training set.

In order to train the model, all spectra were first shifted to the rest frame by the reduction pipeline [25], and then linearly interpolated onto a common wavelength grid. The training procedure consists of minimising a loss function between an internal model of *The Cannon* and observations for every pixel of a spectrum [71].

The result of this training procedure are quadratic relations that take desired stellar parameters  $T_{\text{eff}}$ ,  $\log g$ ,  $[\text{Fe}/\text{H}]$ , and  $v \sin i$  to reconstruct a target spectrum. Spectra generated in this manner are trustworthy only within the parameter space defined by the training set, where the main limitation is the effective temperature which ranges from  $\sim 4600$  to  $\sim 6700$  K on the main sequence. Spectra of hotter stars are easy to reproduce, but they lack elemental absorption lines that we would like to analyse. On the other hand, spectra of colder stars are packed with molecular absorption lines and therefore harder to reproduce and analyse. The model itself can be used to extrapolate spectra outside the initial training set, but as they can not be verified, they were not considered to be useful for the analysis.

### 4.5.2 Photometric model

With the use of a model that produces normalised spectra for every given set of stellar parameters, we lose all information about the stars' colour, luminosity, and spectral energy distribution. This can be overcome using another model that generates the photometric signature of a desired star. To create this kind of a model, we first collected up to 13 apparent magnitudes from the selected photometric surveys (*Gaia*, APASS, 2MASS, and WISE) for every star in the GALAH survey. Whenever possible, these values were converted to absolute magnitudes using the distance to stars inferred by the Bayesian approach [80]. Before using the pre-computed published distances, we removed all sources whose computed astrometric re-normalised unit-weight error [RUWE, 4] was greater than 1.4. The magnitudes of every individual star were also corrected for the reddening effect, except for the WISE photometric bands W1 and W2 that were considered to be extinction free.

Using the valid *The Cannon* stellar parameters, the inferred and corrected absolute magnitudes in multiple photometric bands were grouped into bins that contain stars within  $\Delta T_{\text{eff}} = \pm 80$  K,  $\Delta \log g = \pm 0.05$  dex, and  $\Delta [\text{Fe}/\text{H}] = \pm 0.1$  dex around

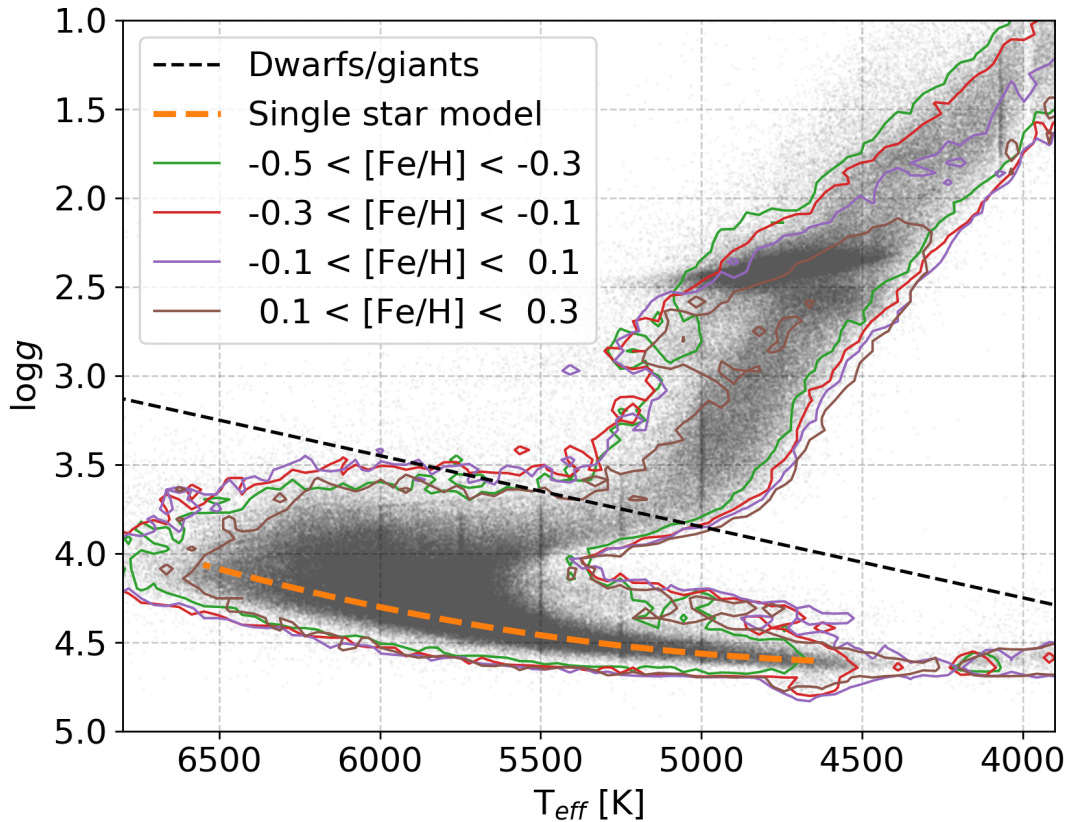


Figure 4.5: Complete observational set of valid stellar parameters shown as a varied density of grey dots. Contours around the diagram illustrate a coverage of parameter space in different  $[Fe/H]$  bins. Overlaid orange dashed curve represents a relation on the main sequence from where single stars considered in the fit are drawn. Additionally, black dashed linear line represents arbitrarily defined limit between giant and dwarf stars that were used in the process of training a spectroscopic single star model.

the bin centre. As spectroscopically unresolved multiple stellar systems could still be present in this bin, median photometric values are computed per bin to minimise their effect. Extrapolation outside this grid, that covers the complete observational stellar parameter space, is not desired nor implemented as it may produce erroneous values. When a photometric signature of a star with parameters between the grid points is requested, it is recovered by linear interpolation between the neighbouring grid points. The median photometric signature for the requested stellar parameters could also be computed on-the-fly using the same binning, but we found out that this produced insignificant difference and increased the processing time by more than a factor of 2.

### 4.5.3 Limitations in the parameter space

As already emphasized, spectroscopic and photometric models were built on real observations and are therefore limited by the training set coverage. The limitations are visually illustrated by Figure 4.5, where the dashed curve, from which single

stars are drawn, is plotted over the observations. This arbitrary quadratic function is defined as:

$$\log g = 2.576 + 9.48 \cdot 10^{-4} T_{\text{eff}} - 1.10 \cdot 10^{-7} T_{\text{eff}}^2, \quad (4.2)$$

where values of  $T_{\text{eff}}$  and  $\log g$  are given in units of K and  $\text{cm s}^{-2}$  respectively. The polynomial coefficients were determined by fitting a quadratic function to manually defined points that represent regions with the highest density of stars on the shown Kiel diagram. From Equation 4.2, it follows that the  $\log g$  of a selected single star is not varied freely, but computed from the selected  $T_{\text{eff}}$  whose range is limited within the values  $6550 > T_{\text{eff}} > 4650$  K.

Focusing on Solar-like stars gives us an advantage in their modelling as the whole observational diagram in Figure 4.5 is sufficiently populated with stars of Solar-like iron abundance. When going towards more extreme  $[\text{Fe}/\text{H}]$  values (high or low), coverage of the main sequence starts to decrease. For cooler stars, this happens at low iron abundance ( $[\text{Fe}/\text{H}] < -0.3$ ) and for hot stars at high abundance ( $[\text{Fe}/\text{H}] > 0.3$ ). Those limits pose no problems for our analysis, unless the wrong stellar configuration is used to describe the observations. At that point, the spectroscopic fitting procedure would try to compensate for too deep or too shallow spectral lines (effect of wrongly selected  $T_{\text{eff}}$ ) by decreasing or increasing  $[\text{Fe}/\text{H}]$  beyond values reasonable for Solar-like objects.

## 4.6 Characterization of multiple system candidates

For the detailed characterization of Solar twin candidates that show excess luminosity, we used their complete available photometric and spectroscopic information. The excess luminosity can only be explained by the presence of an additional stellar component or a star that is hotter or larger than the Sun. Both of those cases can be investigated and confirmed by the data and models described in Sections 5.3 and 4.5. In the scope of our comparative methodology, we constructed a broad collection of synthetic single, double, and triple stellar systems that were compared and fitted to the observations.

As the measured *Gaia* DR2 parallaxes, and therefore inferred distances, of some objects are badly fitted or highly uncertain, the distance results provided by [80] actually yield three distinct distance estimates - the mode of an inferred distance distribution (`r_est`) and a near and distant distance (`r_lo`, and `r_hi`) estimation, between which 68 % of the distance estimations are distributed. As the actual shape of the distribution is not known and could be highly skewed, we did not draw multiple possible distances from the distribution, but only used its mode value.

### 4.6.1 Fitting procedure

A complete characterization and exploration fitting procedure for every stellar configuration (single, binary, and triple) consists of four consecutive steps that are detailed in the following sections. As we are investigating Solar twin spectra, the initial assumption for the iron abundance of the system is set to  $[\text{Fe}/\text{H}] = 0$ . This also includes the assumption that stars in a system are of the same age, at similar evolutionary stages, and were formed from a similarly enriched material. If that is true, we can set iron abundance to be equal for all stars in the system. This notion

is supported by the simulations [85] and studies [86] of field stars showing that close stars are very likely to be co-natal if their velocity separation is small.

The observed systems must be composed of multiple main sequence stars, otherwise the giant companion would dominate the observables, and the system would not be a spectroscopic match to the Sun. Therefore their parameters  $T_{\text{eff}}$  and  $\log g$  are drawn from the middle of the main sequence determined by *The Cannon* parameters in the scope of the GALAH survey. The Kiel diagram of the stars with valid parameters and model of the main sequence isochrone used in the fitting procedure are shown in Figure 4.5.

#### 4.6.2 Photometric fitting - first step

With those initial assumptions in mind, we begin with the construction of the photometric signature of the selected stellar configuration. To find the best model that describes the observations, we employ a Bayesian MCMC fitting approach [87], where the varied parameter is the effective temperature of the components. The selected  $T_{\text{eff}}$  values, and inferred  $\log g$  (Equation 4.2), are fed to the photometric model (Section 4.5.2) to predict a photometric signature of an individual component. Multiple stellar signatures are combined together into a single unresolved stellar source using the following equation:

$$M_{\text{model}} = -2.5 \log_{10} \left( \sum_{i=1}^{n_s} 10^{-0.4M_i} \right); \quad n_s = [1, 2, 3], \quad (4.3)$$

where  $M_i$  denotes absolute magnitude of a star in one of the used photometric bands, and  $n_s$  number of components in a system. The newly constructed photometric signature at selected  $T_{\text{eff}}$  values is compared to the observations using the photometric log-likelihood function  $\ln p_P$  defined as:

$$\ln p_P(T_{\text{eff}} | M, \sigma) = -\frac{1}{2} \sum_{i=1}^{n_p} \left[ \frac{(M_i - M_{\text{model},i})^2}{\sigma_i^2} + \ln(2\pi\sigma_i^2) \right], \quad (4.4)$$

where  $M$  and  $\sigma$  represent extinction corrected absolute magnitudes, and their measured uncertainties that were taken for multiple published catalogues presented in Section 5.3. The constructed photometric model of a multiple system is represented by the variable  $M_{\text{model}}$  and the number of photometric bands by  $n_p$ . The maximum, and most common value for  $n_p$  is 13, but in some cases, it can drop to as low as 8. The MCMC procedure is employed to maximise this log-likelihood and find the best fitting stellar components.

To determine the best possible combination of  $T_{\text{eff}}$  values, we initiate the fit with 1200 uniformly distributed random combinations of initial temperature values that span the parameter space shown in Figure 4.5. The number of initial combinations is intentionally high in order to sufficiently explore the temperature space. Excessive or repeated variations of initial parameters are rearranged by a prior limitation that the temperatures of components must be decreasing, therefore  $T_{\text{eff}1} >= T_{\text{eff}2} >= T_{\text{eff}3}$  in the case of a triple system (example of used initial walker parameters is shown in Figure 4.17). The initial conditions are run for 200 steps. The number of steps was selected in such a way to ensure a convergence of all considered cases (example of the walkers convergence is shown in Figure 4.18). The distribution of priors for

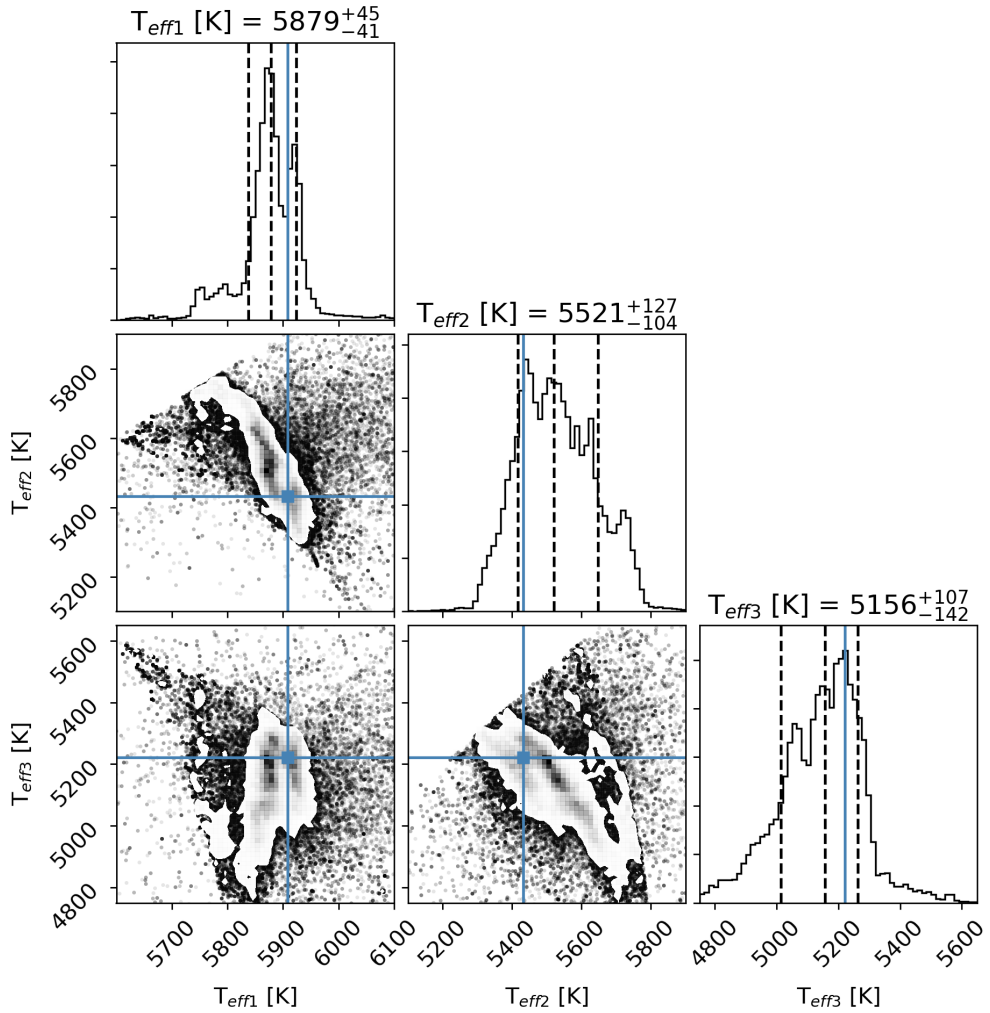


Figure 4.6: Distribution of considered posteriors during the initial MCMC photometric fit for one of the objects that was at the end classified as a triple candidate. As the plots show the first step in the fitting procedure that explores the complete parameter space, the distributions are not expected to be smooth because of possible multiple local minima. Values indicated on the scatter plots represent medians for the 10 % of the best fitting solutions.

such a run is shown as a corner plot in Figure 4.6. After that, only the best 150 walkers are kept, their values perturbed by 2 %, and run for another 200 steps to determine the posterior distribution of the parameters varied during the MCMC fit. This two-step run is needed to speed up the process and discard solutions with lower  $\ln p_P$ . During the initial tests, we found that the investigated parameter space can have multiple local minima which attract walkers, especially in the case of a triple system.

After the completion of all MCMC steps, the considered parameter combinations are ordered by their log-likelihood in descending order. Of those, only 10 % of the best fitting combinations are used to compute final  $T_{\text{eff[1-3]}}$  values. They are computed as the median of the selected best combinations.

### 4.6.3 Spectroscopic fitting - second step

After an effective temperature of the components has been determined, we proceed with the evaluation of how well they reproduce the observed spectrum. As a majority of the fitted systems do not consist of multiple components with a  $T_{\text{eff}}$  equal to Solar, the [Fe/H] of the system must be slightly changed to equalize absorption strength of the simulated and observed spectral lines.

To determine the [Fe/H] of the system, we first compute a simulated spectrum for every component using a spectroscopic model described in Section 4.5.1. Individual spectra are afterwards combined using Equation 4.5 in the case of a binary system or Equation 4.6 in the case of a triple system.

$$\begin{aligned} r_{12} &= \frac{L_{2,\lambda}}{L_{1,\lambda}}; \quad \lambda = [1, 2, 3, 4] \\ f_{model,\lambda} &= \frac{f_{1,\lambda}}{1 + r_{12}} + \frac{f_{2,\lambda}}{1 + 1/r_{12}} \end{aligned} \quad (4.5)$$

$$\begin{aligned} r_{12} &= \frac{L_{2,\lambda}}{L_{1,\lambda}}, \quad r_{13} = \frac{L_{3,\lambda}}{L_{1,\lambda}} \\ f_{model,\lambda} &= \frac{f_{1,\lambda}}{1 + r_{12} + r_{13}} + \frac{r_{12}f_{2,\lambda}}{1 + r_{12} + r_{13}} + \frac{r_{13}f_{3,\lambda}}{1 + r_{12} + r_{13}} \end{aligned} \quad (4.6)$$

Individual normalised spectra, denoted by  $f_{n,\lambda}$  in Equations 4.5 and 4.6, are weighted by the luminosity ratios between the components ( $r_{xy}$ ) and then summed together.

As the HERMES spectrum covers four spectral ranges, whose distribution of spectral energy depends on stellar  $T_{\text{eff}}$ , different luminosity ratios also have to be used for every spectral arm. Of all of the used photometric systems, APASS filters B, g', r', and i' have the best spectral match with blue, green, red, and infrared HERMES arm. The modelled APASS magnitudes of the same stars are used to compute luminosity ratios between them.

The described summation of the spectra introduces an additional assumption about the analysed object. With this step, we assume that components have a negligible internal spread of projected radial velocities that could otherwise introduce asymmetries in the shape of observed spectral lines. The assumption allows us to combine individual components without any wavelength corrections.

Similarly, as in the previous case, a Bayesian MCMC fitting procedure was used to maximise the spectroscopic log-likelihood  $\ln p_S$  defined as:

$$\ln p_S([\text{Fe}/\text{H}]|f, \sigma) = -\frac{1}{2} \sum_{\lambda} \left[ \frac{(f_{\lambda} - f_{model,\lambda})^2}{\sigma_{\lambda}^2} + \ln(2\pi\sigma_{\lambda}^2) \right], \quad (4.7)$$

where  $f$  and  $\sigma$  represent the observed spectrum and its per-pixel uncertainty, respectively. A modelled spectrum of the system, at selected [Fe/H], is represented by the variable  $f_{model}$  and the number of wavelength pixels in that model by  $\lambda$ . Combined, all four spectral bands consist of almost 16,000 pixels.  $T_{\text{eff}}$  values of the components are fixed for all considered cases.

The MCMC fit is initiated with 150 randomly selected [Fe/H] values, whose uniform distribution is centred at the initial [Fe/H] value of the system and has a span of 0.4 dex. All of the initiated walkers are run for 100 steps. At every

[Fe/H] level, a new simulated spectrum composite is generated and compared to the observed spectrum by computing log-likelihood  $\ln p_S$  of a selected [Fe/H] value. The range of possible [Fe/H] values considered in the fit is limited by a flat prior between  $-0.5$  and  $0.4$ .

By the definition of [Fe/H] in the scope of GALAH *The Cannon* analysis, the parameter describes stellar iron abundance and not its metallicity as commonly used in the literature. Therefore only spectral absorption regions of un-blended Fe atomic lines are used to compute the spectral log-likelihood. Having to fit only one variable at a time, the solution is easily found and computed as a median value of all posteriors considered in the fit.

### 4.6.4 Final fit - third step

A changed value of [Fe/H] for the system will introduce subtle changes to its photometric signature, therefore we re-initiate the photometric fitting procedure. It is equivalent to the procedure described in Section 4.6.3, but with much narrower initial conditions. These new initial conditions are uniformly drawn from the distribution centred at  $T_{\text{eff}}$  values determined in the first step of the fitting procedure. The width of the uniform distribution is equal to 100 K. Drawn initial conditions are afterwards run through the same procedure as described before.

At this point, the second and third step in the fitting procedure can be repeatedly run several times to further pinpoint the best solution. We found out that further refinement was not needed in our case as it did not influence the determined number of stars in the system.

### 4.6.5 Number of stellar components - final classification

The fitting procedure described above was used to evaluate observations of every multiple stellar candidate to determine whether they belong to a single, binary or triple stellar system. This resulted in the following set of results for every configuration: predicted  $T_{\text{eff}}$  of the components, [Fe/H] of the system, simulated spectrum, and simulated photometric signature of the system.

As the photometric and spectroscopic fits do not always agree on the best configuration, the following set of steps and rules was applied to classify results in one of six classes presented in Table 4.1.

- Compute  $\chi^2$  between the simulated photometric signature of the modelled system and extinction corrected absolute photometric observations for every considered stellar configuration.
- Compute  $\chi^2$  between the simulated spectrum of the modelled system and the complete GALAH observed spectrum for every considered stellar configuration.
- Independently select the best fitting configuration with the lowest  $\chi^2$  for photometric and spectroscopic fit.
- If the best photometric and spectroscopic fit point to the same configuration, then the system is classified as having a number of stars defined by both fitting procedures.

Table 4.1: Number of different systems discovered by the fitting procedure performed on possible multiple stars that exhibit excess luminosity.

Configuration classification	Number of systems
1 star	2
$\geq 1$ star	14
2 stars	27
$\geq 2$ stars	14
3 stars	6
Inconclusive	1
Total objects	64

- If the best photometric and spectroscopic fit do not point to the same configuration, then the system is classified as having at least as many stars as determined by the prediction with a lower number of stars (e.g.  $\geq 2$  stars).
- If the difference between those two predictions is greater than 1 (e.g. photometric fit points to a single star and spectroscopic to a triple star), then the system is classified as inconclusive.

The classification produced using these rules is shown as colour coded *Gaia* colour-magnitude diagram in Figure 4.7.

#### 4.6.6 Quality flags

In addition to our final classification, we also provide an additional quality checks that might help to identify cases for which our method might return questionable determination of a stellar configuration. Every of those checks, listed in Table 4.2, is represented by one bit of a parameter `flag` in the final published table (Table 5.1). The first bit gives us an indication of whether the object could have an uncertain astrometric solution, whereas the second and the third bits indicate if the final fitted solution has a worse match with the observations than the parameters produced by the *The Cannon* pipeline. To evaluate this, we used the original stellar parameters reported for the object to construct their photometric and spectroscopic synthetic model that was compared to the observations by computing their  $\chi^2$  similarity (`m_sim_p` and `m_sim_f` in Table 5.1). The resulting fitted spectrum or photometric signature is marked as deviating if its similarity towards observations is worse than for the reported one star parameters. This might not be the best indication of possible mismatch as it is common that *The Cannon* parameters of the analysed multiple candidates deviate from the main sequence in Kiel diagram (Figure 4.5) and therefore fall into less populated parameter space, where they can skew the single star models (Sections 4.5.1 and 4.5.2).

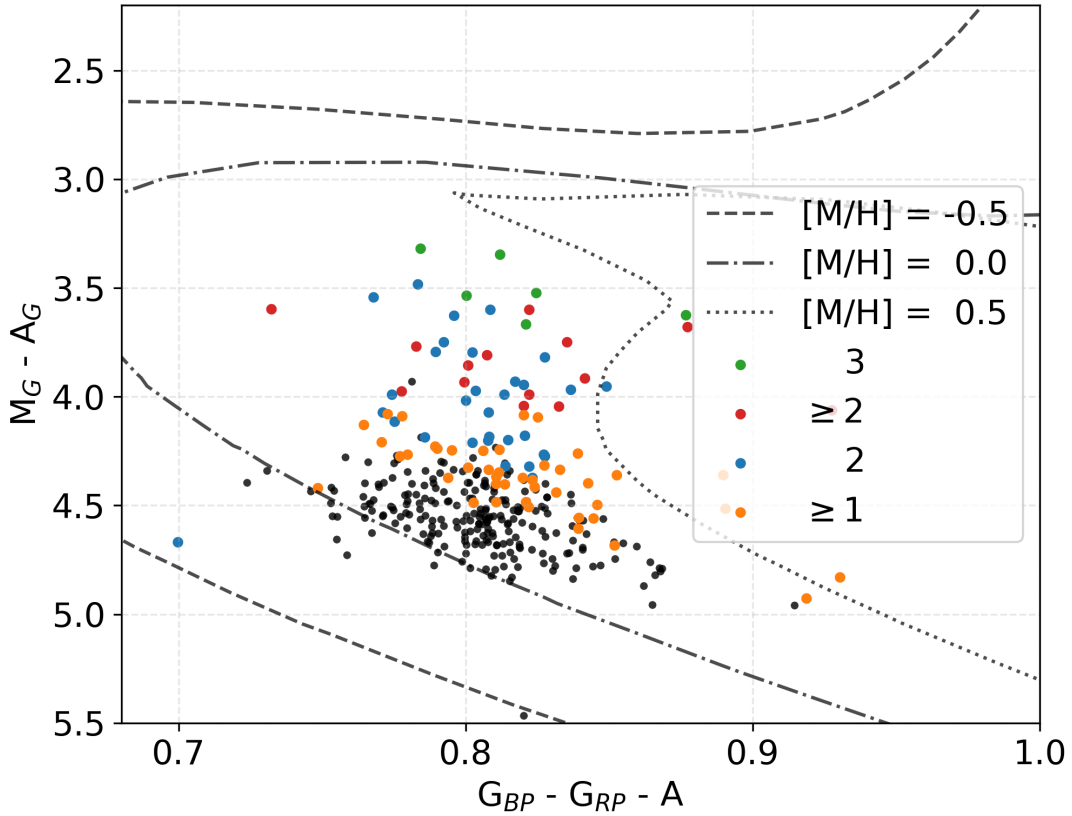


Figure 4.7: Showing the same data points as Figure 4.4 with indicated definite triple (green dots), possible triple (red dots), binary (blue dots), and possible binary stellar systems (orange dots). All other classes are shown with black dots. Overplotted are PARSEC isochrones [83] for stars with the age of 4.5 Gyr and different metallicities.

Table 4.2: Explanation of the used binary quality flags in the final classification of the stellar configuration. A raised bit could indicate possible problems or mismatches in the determined configuration. Symbol X in the last two descriptions represents the best fitting configuration, therefore  $X = [1, 2, 3]$ .

Raised bit	Description
0	None of the flags was raised
1 <sup>st</sup> bit	High astrometric uncertainty ( $\text{RUWE} > 1.4$ )
2 <sup>nd</sup> bit	Deviating photometric fit ( $sX_{\text{sim\_p}} > m_{\text{sim\_p}}$ )
3 <sup>rd</sup> bit	Deviating spectroscopic fit ( $sX_{\text{sim\_s}} > m_{\text{sim\_s}}$ )

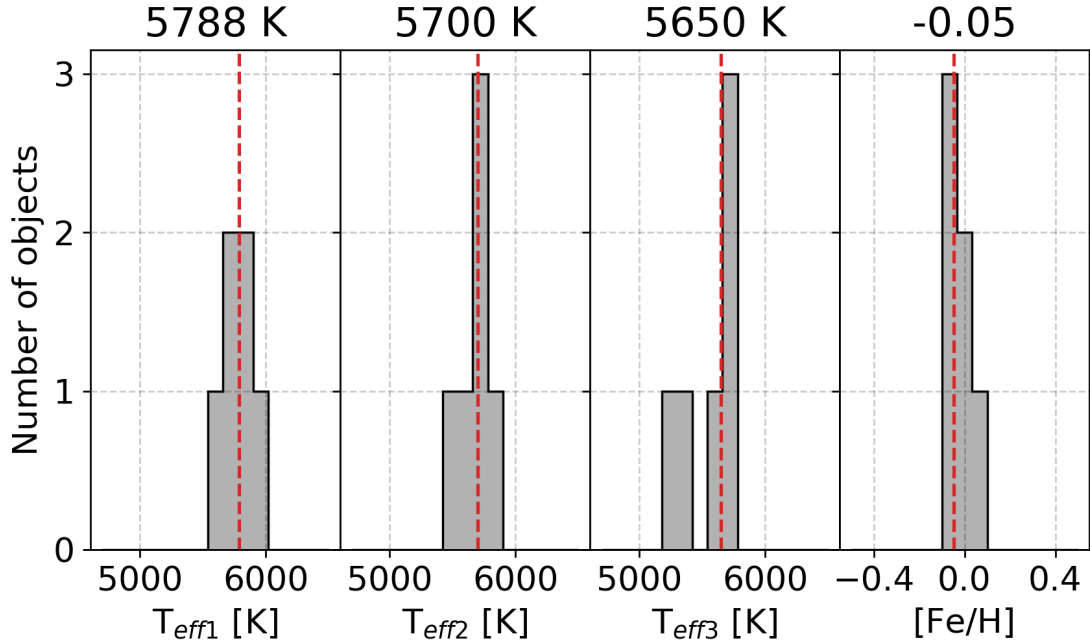


Figure 4.8: Parameters of triple stellar systems discovered and characterized by our analysis. Histograms represent distribution of all fitted results for 6 objects that were classified as triple stellar systems and observationally mimic Solar spectrum. Median values of the distributions are given above individual histogram and indicated with dashed vertical line.

## 4.7 Characterization of single star candidates

Once we concluded our analysis of the set of 64 objects that showed obvious signs of excess luminosity, we then proceeded to study the remaining 265 objects that are most probably not part of a complex stellar system. To explore their composition, they were analysed with the same procedure as multiple candidates (Section 4.6). Before running the procedure, we omitted the option to fit for a triple system as they clearly do not possess enough excess luminosity for that kind of a system.

The obtained results were analysed and classified using the same set of rules introduced in Section 4.6.5. Retrieved classes are summarized in Table 4.3 and in Figure 4.7. In the latter we see that the potential binaries are located on the top of the colour-magnitude diagram, which is consistent with the potential presence of an additional stellar source.

## 4.8 Orbital period constraints

The observational data we have gathered on possible multiple systems point to configurations that change slowly as a function of time. Using the observational constraints and models that describe the formation of the observed spectra, we try to set limiting values on the orbital parameters of the detected triple stellar system candidates. In order to have a greater sample size, we use both definite (class 3) and probable (class  $\geq 2$ ) triple stars.

With the limited set of observations, we have to set assumptions about the constitution of those systems. For a hierarchical 2 + 1 system to be dynamically

Table 4.3: Number of different systems discovered by the fitting procedure performed on stars that do not exhibit excess luminosity. Classes and their description is the same as used in Table 4.1. In addition, number of stars without parallactic measurements is added for completeness.

Configuration classification	Number of systems
1 star	230
$\geq 1$ star	31
2 stars	4
$\geq 2$ stars	0
3 stars	0
Inconclusive	0
Unknown parallax	0
Total objects	265

stable on long timescales, its ratio between the orbital period of an inner pair  $P_S$  and outer pair  $P_L$  must be above a certain limit. Eggleton [88] showed that  $P_L/P_S$  must be higher than 5. The same lower limit is noticeable when the correlation between periods of the known triple stars is plotted [89, 90].

In order to estimate the periods, we have to know the masses and distances between the stars in a system. Without complete information about the projected velocity variation in a system, masses can also be inferred from the spectral type. As we are looking at the Solar twin triples, whose effective temperatures are all very similar and close to Solar values (see Figure 4.8), our rough estimate is that all stars also have a Solar-like mass  $\sim M_\odot$ . From this, we can set the inner mass ratio  $q_S$  to be close to 1 and the outer mass ratio  $q_L \sim 0.5$ . When we are dealing with the outermost star, the inner pair is combined into one object with twice the mass of the Sun. The likelihood of such a configuration is also supported by the observations [89] where a higher concentration of triple systems is present around those mass ratios. Contrary to our systems, twin binaries with equal masses usually have shorter orbital periods [91].

With the initial assumption about the configuration of the triple systems and masses of the stars, the periods of the inner and outer pair can be constrained to some degree as other orbital elements (inclination, ellipticity, phase ...) are not known.

### 4.8.1 Outer pair and *Gaia* angular resolution

Limited by its design, *Gaia* spacecraft and its on-ground data processing are in theory unable to resolve stars with the angular separation below  $\sim 0.1$  arcsec. Above that limit, their separability is governed by the flux ratio of the pair. The validation report of the latest data release [92] shows that the currently achieved angular resolution is approximately 0.4 arcsec as none of the source pairs is found closer than this separation. We used this reported angular limit to assess possible or-

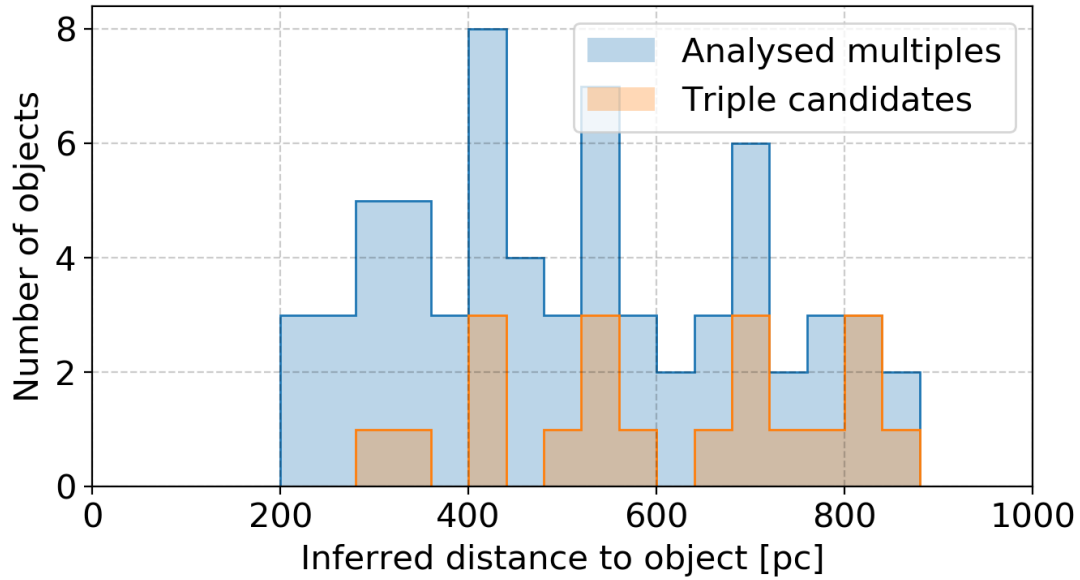


Figure 4.9: Histogram showing distribution of radial distances for the analysed set of stars. Distances were inferred by the Bayesian approach that takes into account the distribution of stars in the Galaxy [80].

bital configurations that are consistent with both the spectroscopic and astrometric observations.

Along with the final astrometric parameters, the *Gaia* data set also contains information about the goodness of the astrometric fit. Evans [93] used those parameters to confirm old and find new candidates for unresolved exoplanet hosting binaries in the data set. As we are looking at a system of multiple stars that orbit around their common centre of mass, we expect their photo-centre to slightly shift during such orbital motion. The observed wobble of the photo-centre also depends on the mass of stars in the observed system. In the case of a binary system containing two identical stars, the wobble would not be observed, but its prominence increase as the difference between their luminosities becomes more pronounced. This subtle change in the position of a photo-centre adds additional stellar movement to the astrometric fit, consequently degrading its quality. Improvements for such a motion will be added in latter *Gaia* data releases. If a system has an orbital period much longer than the time-span of *Gaia* DR2 measurements (22 months), its movement has not yet affected the astrometric solution. This puts an upper limit on an orbital period as it should not be longer than few years in order to already affect the astrometric fit results.

Setting limits to the parameters of astrometric fit quality [`astrometric_excess_noise > 5`, and `astrometric_gof_a1 > 20` as proposed by 93], none of our 329 stars meets those requirements. This suggests that all of them are most likely well below the *Gaia* separability limit and/or have long orbital periods. Another indicator for a lower-quality astrometric fit that we can use is RUWE. Figure 4.4 shows distribution of potentially problematic large RUWE among single and multiple candidates. The latter, on average, have a much poorer fit quality that might indicate a presence of an additional parameter that needs to be considered in the astrometric fit.

Distances to triple stars, shown by the histogram in Figure 4.9 range from around 0.3 to 0.9 kpc. From this we can assume the maximal allowable distance between components of an outer pair to be in the order of 100–350 AU, pointing to outer orbital periods larger than 500 years. To test if such systems would meet our detection constraints, we created 100,000 synthetic binary systems whose orbital parameters were uniformly distributed within the parameter ranges given in Table 4.4. Observable radial velocities of both components were computed using the following equations:

$$v_1 = \frac{2\pi \sin i}{P\sqrt{1-e^2}} \frac{aq}{1+q} (\cos(\theta + \omega) + e \cos \omega) \quad (4.8)$$

$$v_2 = \frac{2\pi a \sin i}{P\sqrt{1-e^2}} \frac{a}{1+q} (\cos(\theta + \omega + \pi) + e \cos(\omega + \pi)) \quad (4.9)$$

$$P = \sqrt{a^3 \frac{4\pi^2}{GM_1(1+q)}} \quad (4.10)$$

The distribution of velocity separations ( $\Delta v = v_2 - v_1$ ) for synthetic systems is given by Figure 4.10, where we can see that more than 99.7 % of generated configurations would produce a spectrum that would still be considered as a Solar twin ( $\Delta v < 6 \text{ km s}^{-1}$ , see Section 4.9.1 and Figure 4.19 for further clarification). If we set the semi-major axis  $a$  (in Table 4.4) to single value in the same simulation, we can find the closest separation that would still meet the same observational criteria in at least 68 % of the cases. In our simulation this happens at the mutual separation of 10 AU (and at 50 AU for 95 % of the cases). The orbital period of a such outer pair is about 18 years (and 200 years for 50 AU) and is most probably way too long to had significant effect on the quality of the astrometric fit. Considering observationally favorable orbital configurations with face-on orbits, the actual system could be much more compact than estimated.

#### 4.8.2 Inner binary pair and formation of double lines in a spectrum

An upper estimate of orbital sizes for an outer pair gives us a confirmation that almost every considered random orbital configurations would satisfy the observational and selection constraints. To ensure the long-term stability of such a system, the inner pair must have a period that is at least five times shorter [88]. At such short orbital periods, the inner stars could potentially move sufficiently rapidly in their orbits as to produce noticeable absorption line splitting for edge-on orbits. To be confident that none of the analysed objects produces such an SB2 spectrum, we visually checked all considered spectra and found no noticeable line splitting in any of the acquired GALAH or Asiago spectra. A subtle hint about a possible broadening of the spectral lines comes from the determined  $v \sin i$ . The median of its distribution in Figure 4.11 is higher for multiple candidates with excess projected velocity of  $\sim 0.5 \text{ km s}^{-1}$ .

Accounting for the GALAH resolving power and spectral sampling, we can estimate a minimal radial velocity separation between components of a spectrum to show clear visual signs of duplicated spectral lines. To determine a lower limit, we

Table 4.4: Ranges of the orbital parameters used for the prediction of observable radial velocity separation between stars in an outer binary pair. The range of the semi-major axis length  $a$  is set between the *Gaia* separability limit for the closest and farthest triple candidate. The uniform distribution of  $a$  is a good approximation of the real periodicity distribution published by Raghavan *et al.* [34] as we are sampling a narrow range of it. Use of the real observed distribution would in our case introduce insignificant changes in radial velocity separation as we are simulating wide, slowly rotating systems.

Parameter	Considered range
$M_1$	$2 \text{ M}_\odot$
$a$	$100 \dots 350 \text{ AU}$
$q$	$0.45 \dots 0.55$
$\sin i$	$0 \dots 1$ ( $i = 0 \dots 90 \text{ deg}$ )
$e$	$0.1 \dots 0.8$
phase	$0 \dots 1$ , used for calculation of $\theta$
$\omega$	$0 \dots 360 \text{ deg}$

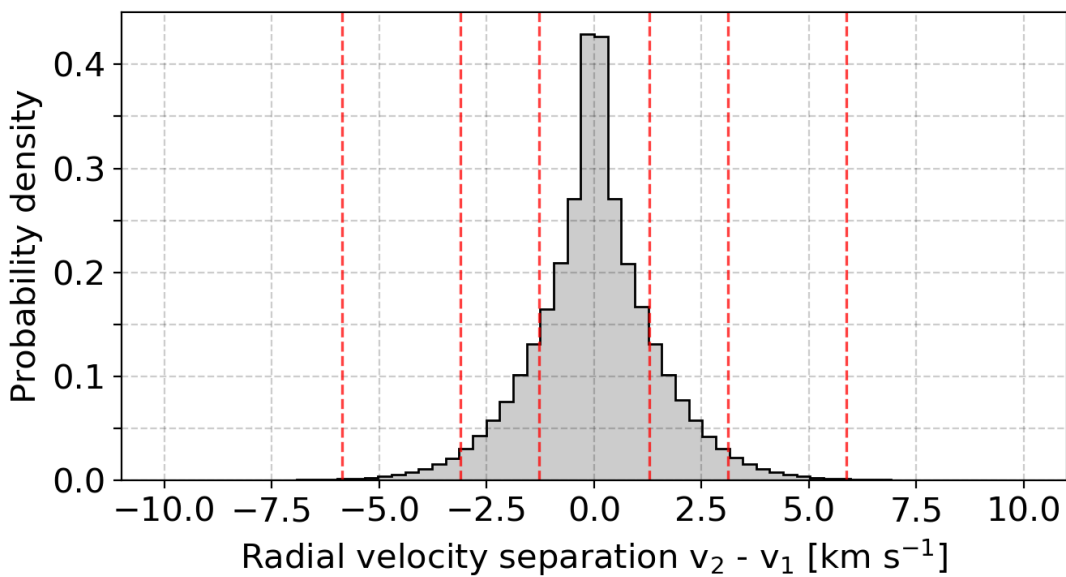


Figure 4.10: Distribution of computed radial velocity separations between a primary and secondary component of the simulated binary systems defined by the orbital parameters given in Table 4.4. Red vertical lines show 1, 2, and 3  $\sigma$  probabilities of the given distribution.

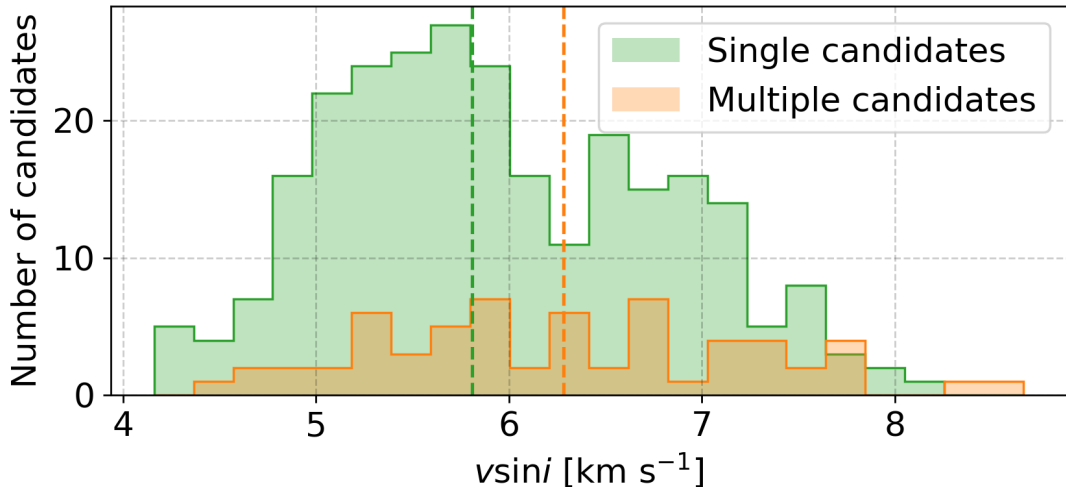


Figure 4.11: Distribution of determined  $v \sin i$  for analysed single and multiple candidates. Median values of the distributions are marked with dashed vertical lines.

combined two Solar spectra of different flux ratios and visually evaluated when the line splitting becomes easily noticeable. With equally bright sources, this happens at the separation of  $\sim 14 \text{ km s}^{-1}$ . When the secondary component contributes  $1/3$  of the total flux, minimal separation is increased to  $\sim 20 \text{ km s}^{-1}$ . A similar separation is needed when secondary contributes only  $10\%$  of the flux. As no line splitting is observed in our analysed spectra, we can be confident that the velocity separation between the binary components was lower than that during the acquisition.

Considering the minimal ratio between outer and inner binary period, we can deduce an expected radial velocity separation of an inner pair for the widest possible orbits. As explained in previous section, we used Equations 4.8-4.10 and possible ranges of inner orbital parameters (Table 4.5) to generate a set of synthetic binary systems. The distribution of their  $\Delta v$  is shown in Figure 4.12 and represent inner binaries with orbital periods from 100 to 700 years. At those orbital periods, more than 92 % of the considered configurations would satisfy the condition of  $\Delta v < 4 \text{ km s}^{-1}$ , ensuring that the observed composite of two equal Solar spectra would still be considered as a Solar twin (see Section 4.9.1 and Figure 4.14 for further clarification). If we limit our synthetic inner binaries to only one orbital period, we can estimate the most compact system that would still meet the observational criteria in at least 68 % of the cases. This would happen at the orbital period of 40 years with a semi-major axis of 14 AU.

### 4.8.3 Multi-epoch radial velocities

To support our claims about slowly changing low orbital speeds in detected triple candidates, we analysed changes in their measured radial velocities between the GALAH and other comparable all-sky surveys. Distributions of changes are presented by three histograms in Figure 4.13 where almost all velocity changes, except one, are within  $5 \text{ km s}^{-1}$ . Differences between the GALAH and *Gaia* radial velocities were expected to be small as the latter reports median velocities in the time-frame

Table 4.5: Same as Table 4.4, but for an inner binary of a hierarchical triple stellar system.

Parameter	Considered range
$M_1$	$M_\odot$
$P_S$	$P_L / 5$ , used for calculation of $a$
$q$	0.9 ... 1.0
$\sin i$	0 ... 1 ( $i = 0 \dots 90$ deg)
$e$	0.1 ... 0.8
phase	0 ... 1, used for calculation of $\theta$
$\omega$	0 ... 360 deg

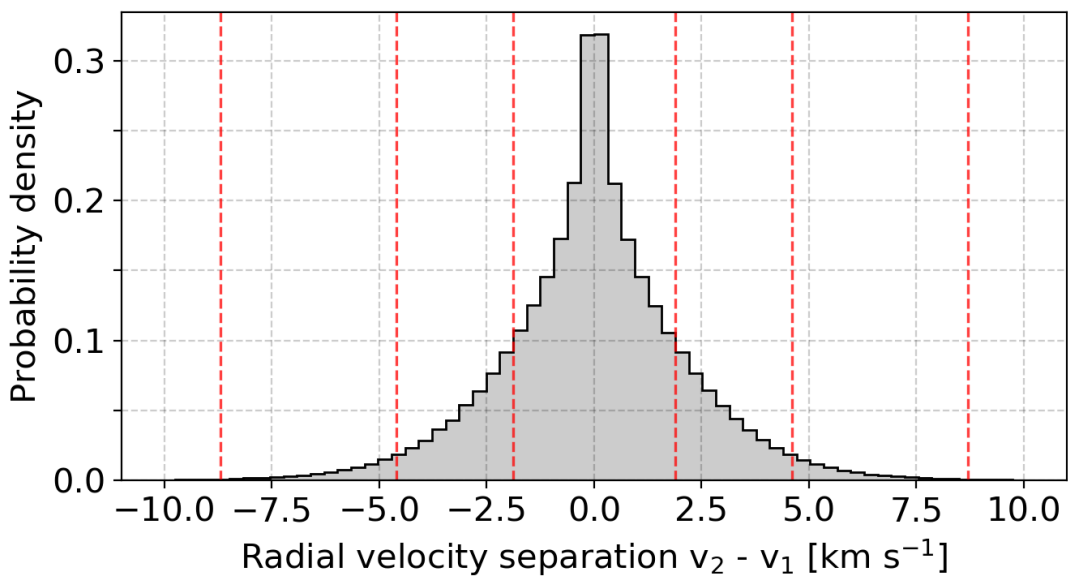


Figure 4.12: Same as Figure 4.10, but for an inner binary of a simulated triple stellar system.

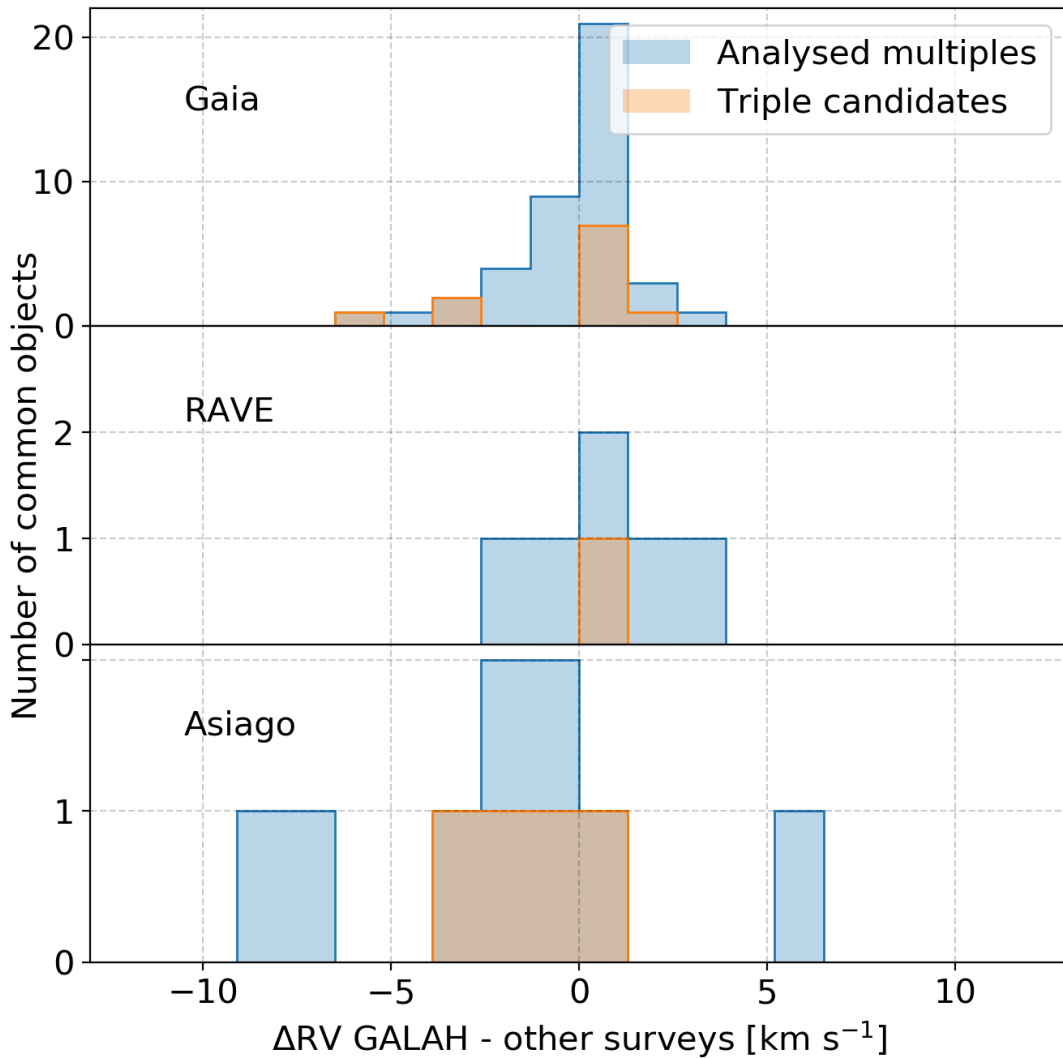


Figure 4.13: RV difference between GALAH and other large spectroscopic surveys. The name of an individual survey or observatory is given in the upper-left corner of every panel. Blue histograms represent velocity difference for all investigated multiple candidates and orange histograms for discovered triple systems only.

that is similar to the acquisition span of the GALAH spectra. Extending the GALAH observations in the past with RAVE and in the future with Asiago observations did not produce any extreme changes. For this comparison, we also have to consider the uncertainty of the measurements that are in the order of  $\sim 2 \text{ km s}^{-1}$  for RAVE and  $\sim 1 \text{ km s}^{-1}$  for Asiago spectra.

With the data synergies, we could produce only three observational time-series that have observations at more than two sufficiently separated times. With only three data points in each graph, not much can be said about actual orbits.

## 4.9 Simulations and tests

To determine the limitations of the employed algorithms, we used them to evaluate a set of synthetic photometric and spectroscopic sources. As the complete procedure depends on the criteria for the selection of Solar twin candidates, we first investigated if the selection criteria allows for any broadening of the spectral lines or their multiplicity as they are both signs of a multiple system with components at different projected radial velocities.

In the second part, we generated a set of ideal synthetic systems that were analysed by the same fitting procedure as the observed data set. The results of this analysis are used to determine what kind of systems could be recognized with the fitting procedure and how the results could be used to spot suspicious combinations of fitted parameters.

In the final part, we try to evaluate selection biases that might arise from the position of analysed stars on the *Gaia* colour-magnitude diagram and from the GALAH selection function that picks objects based on their apparent magnitude.

### 4.9.1 Radial velocity separation between components

To determine the minimal detectable radial velocity (RV) separation between components in a binary or a triple system, we constructed a synthetic spectrum resembling an observation of multiple Suns at a selected RV separation. The spectrum of a primary component was fixed at the rest wavelength with  $\text{RV} = 0 \text{ km s}^{-1}$  and a secondary spectrum shifted to a selected velocity. After the shift, these two spectra were added together based on their assumed flux ratio.

The generated synthetic spectrum was compared to the Solar spectrum with exactly the same metric as described in Section 4.4. Computed spectral similarities at different separations were compared to the similarities of analyzed Solar twin candidates. The first RV separation that produces a spectrum that is more degraded than the majority of Solar twin candidates was determined to be a minimal RV at which the observed spectrum would be degraded enough that it would no longer be recognized as a Solar twin. The high SNR of the generated spectrum was not taken into account for this analysis in contrast to the algorithm that was used to pinpoint Solar twin candidates. Therefore we also omitted candidates with a lower similarity that in our case directly corresponds to their low SNR.

The result of this comparison is presented in Figure 4.14, where we can see that the minimal detectable separation of two equally bright stars resembling the Sun is  $\sim 4 \text{ km s}^{-1}$ . In the case where a primary star contributes  $2/3$  of the total flux, the minimal RV increases to  $\sim 6 \text{ km s}^{-1}$  (see Figure 4.19). Further increase in the ratio between their fluxes would also increase a minimal detectable separation, but only to a certain threshold from where on a secondary star would not contribute enough flux for it to be detectable, and its received flux would be comparable to the typical HERMES spectral noise. In our case, this happens when the secondary contributes less than 10 % of the total flux. These boundaries are only indicative as they also heavily depend on the quality of the acquired spectra. When a low level of noise with the Gaussian distribution ( $\sigma = 0.01$ ) is added to a secondary component with a comparable luminosity, the minimal RV decreases because the similarity between spectra also decreases. In that case, the similarity for  $\Delta v = 0$  is located near the

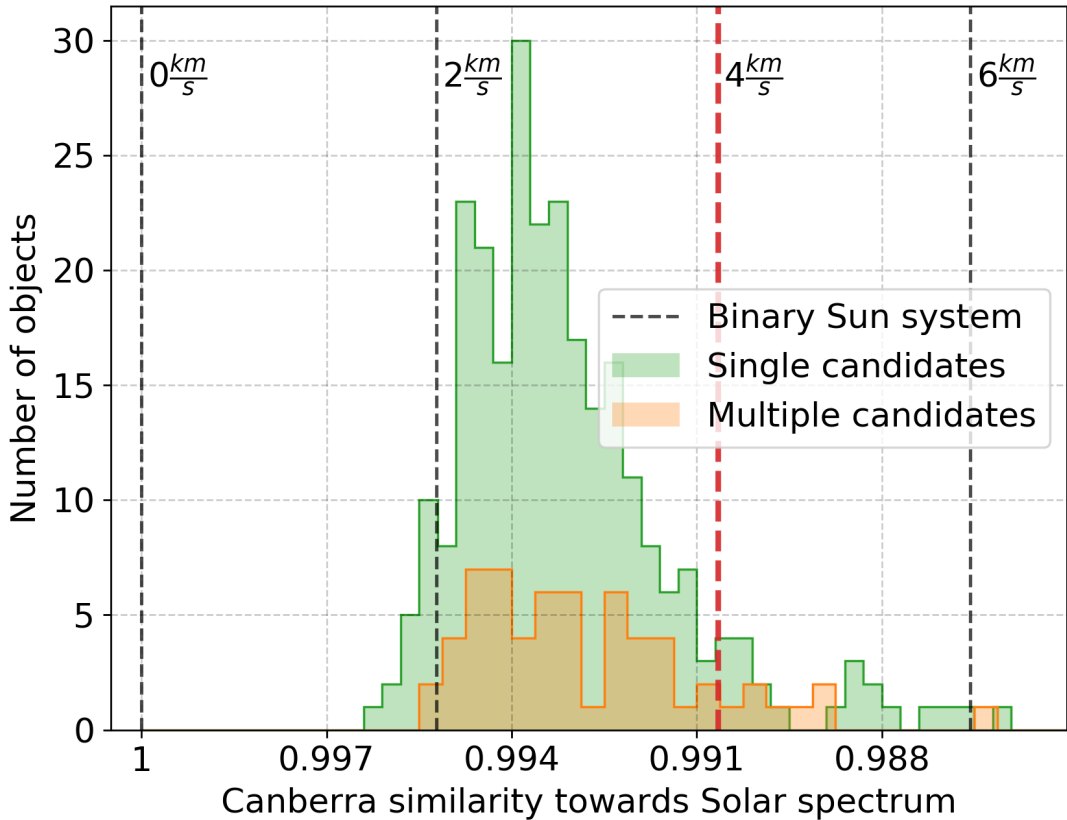


Figure 4.14: Histograms of Canberra similarities towards Solar spectrum for multiple stellar candidates (orange histogram) and single star candidates (green histogram) in the red HERMES arm. Vertical dashed lines represent the same similarity measure, but for a binary system comprising of two equally bright Suns, whose components are at different radial velocities. The separation between components is increasing in  $2 \text{ km s}^{-1}$  steps, where the leftmost vertical line represents the case where both stars are moving with the same projected velocity. The selected maximal velocity at which the composite spectrum would still be considered a Solar twin is marked with the thicker red vertical line. Distribution of histograms also shows that spectra of multiple system candidates are as (dis)similar as spectra of single stars.

mode value of similarity distribution in Figure 4.14.

#### 4.9.2 Analysis of synthetic multiple systems

The limitations and borderline cases of the fitting procedure were tested by evaluating its performance on a set of synthetic binary and triple systems that were generated using the same models and equations as described in the fitting procedure. An ideal, virtually noiseless set comprised 95 binary and 445 triple systems whose components differ in temperature steps of 100 K. The hottest component in the system was set to values in the range between 5300 and 6200 K. The  $T_{\text{eff}}$  of the coldest component could go as low as 4800 K. The [Fe/H] of all synthetic systems was set to 0.0 to mimic Solar-like conditions. Condensed results are presented in Figures 4.15 and 4.20.

As expected, the fitting procedure (Section 4.6) did not have any problem determining the correct configuration of the synthesized system. Temperatures of the components were also correctly recovered with a median error of  $0 \pm 13$  K for the hottest component and  $0 \pm 43$  K for the coldest component in a triple system. A more detailed analysis with the distribution of prediction errors, where the temperature difference between components is taken into account, is presented in Figure 4.15. From that analysis, we can deduce that  $T_{\text{eff}}$  of the secondary component is successfully retrieved if it does not deviate by more than 1000 K from the primary. Results at such large temperature difference are inconclusive as the number of simulated systems drops rapidly. The same can be said for the tertiary component, but with the limitation that it should not be colder by more than 700 K when compared to the secondary star. Beyond that point, the uncertainty of the fitted result increases and a star is determined to be hotter as it really is.

Another application of such an analysis is to identify signs that could point to a possibly faulty solution when it is comparably likely that a multiple system is comprised of two or three components. The results of such an analysis are presented in Figure 4.20, where we tried to describe a binary system with a triple system fit. From the distribution of errors, we can observe that the effective temperature of a primary star with the largest flux is recovered with the smallest fit errors whose median is  $20 \pm 93$  K. As we are using too many components in that fit,  $T_{\text{eff}}$  of a secondary is reduced in order to account for the redundant tertiary component in the fit. As imposed by the limit in the fitting procedure, the tertiary  $T_{\text{eff}3}$  is set to as low as possible. If the same thing happens for a real observed system, this could be interpreted as a model over-fitting.

### 4.9.3 Triple stars across the H-R diagram

In the current stage of Galactic evolution, binary stars with a Solar-like  $T_{\text{eff}}$  are located near a region that is also occupied by main sequence turnoff stars in the Kiel and colour-magnitude diagram (Figures 4.5 and 4.7). This, combined with the fact that older stars with a comparable initial mass and metallicity would also pass a region occupied with binaries (Figure 4.4) poses an additional challenge for detection of unresolved multiples if their spectrum does not change sufficiently during the evolution.

To analyse the possible influence of the turnoff stars and older, more evolved stars, we ran the same detection procedure as described in Section 4.4 and analysis (Section 4.6) to determine the fraction of binaries and triples at different  $T_{\text{eff}}$ , ranging from 5100 to 6000 K, with a step of 100 K. A comparison median spectrum was computed from all spectra in the range  $\Delta T_{\text{eff}} \pm 60$  K,  $\Delta \log g \pm 0.05$  dex and  $\Delta [\text{Fe}/\text{H}] \pm 0.05$  dex, where the main sequence  $\log g$  was taken from the main sequence curve shown in Figure 4.5, and  $[\text{Fe}/\text{H}]$  was set to 0.0. The limiting threshold for multiple candidates was automatically determined in the same way as for Solar twin candidates (Section 4.4.1).

Condensed results of the analysis are shown in Figure 4.16, where we can see that both the fraction of stars with excessive luminosity and triple candidates starts increasing above the  $T_{\text{eff}} \sim 5600$  K. This might indicate that the underlying distribution of more evolved and/or hotter stars might have some effect on our selection function. On the other hand, this increasing binarity fraction coincides with other

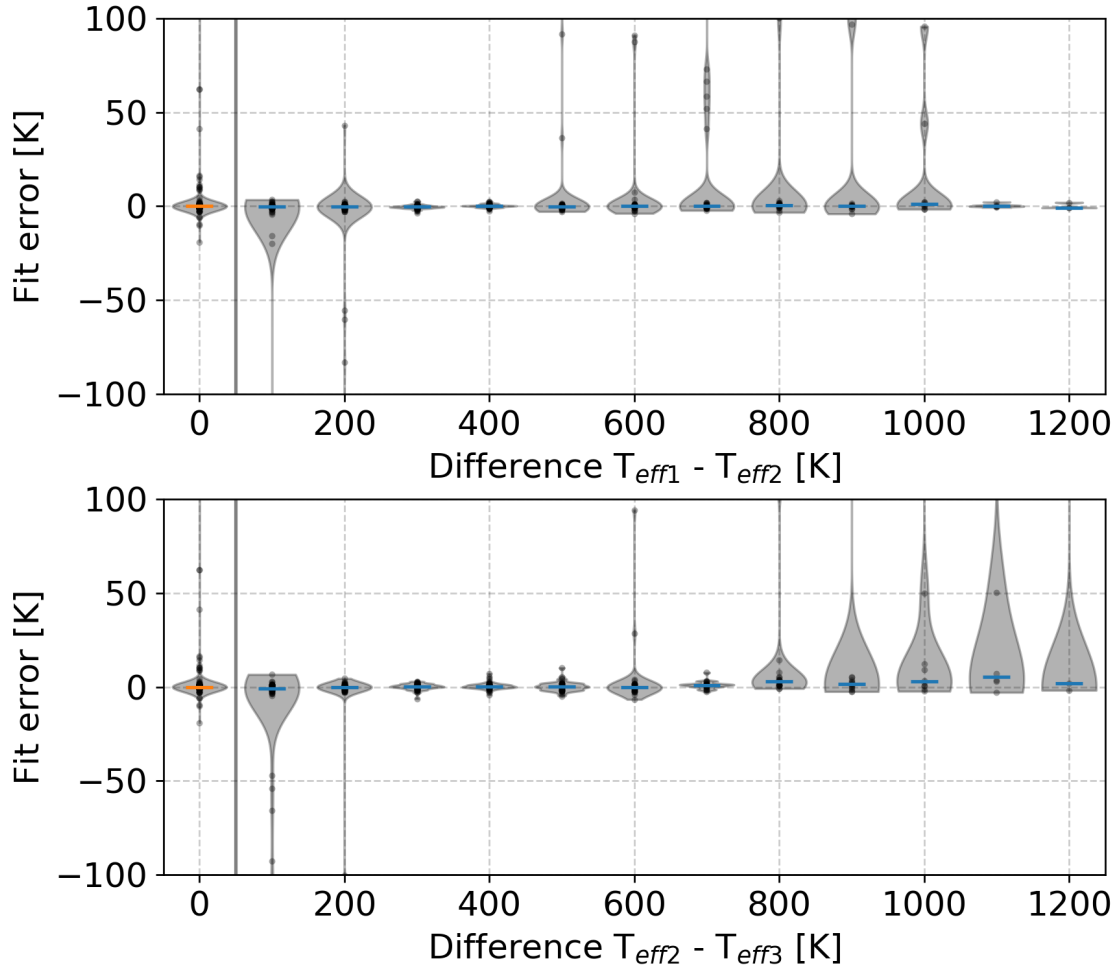


Figure 4.15: The accuracy of our analysis when the fitting procedure is applied to a synthetic triple system. Upper panel shows the distribution of  $T_{\text{eff}}$  prediction errors for a secondary star depending on the difference between selected temperatures of a primary and a secondary star. The lower panel shows the same relation but for a tertiary star in comparison to a secondary. As a reference, the prediction error of a primary star is shown on the left side of both panels. Labels  $T_{\text{eff}1}$ ,  $T_{\text{eff}2}$ , and  $T_{\text{eff}3}$  indicate decreasing effective temperatures of stars in a simulated system.

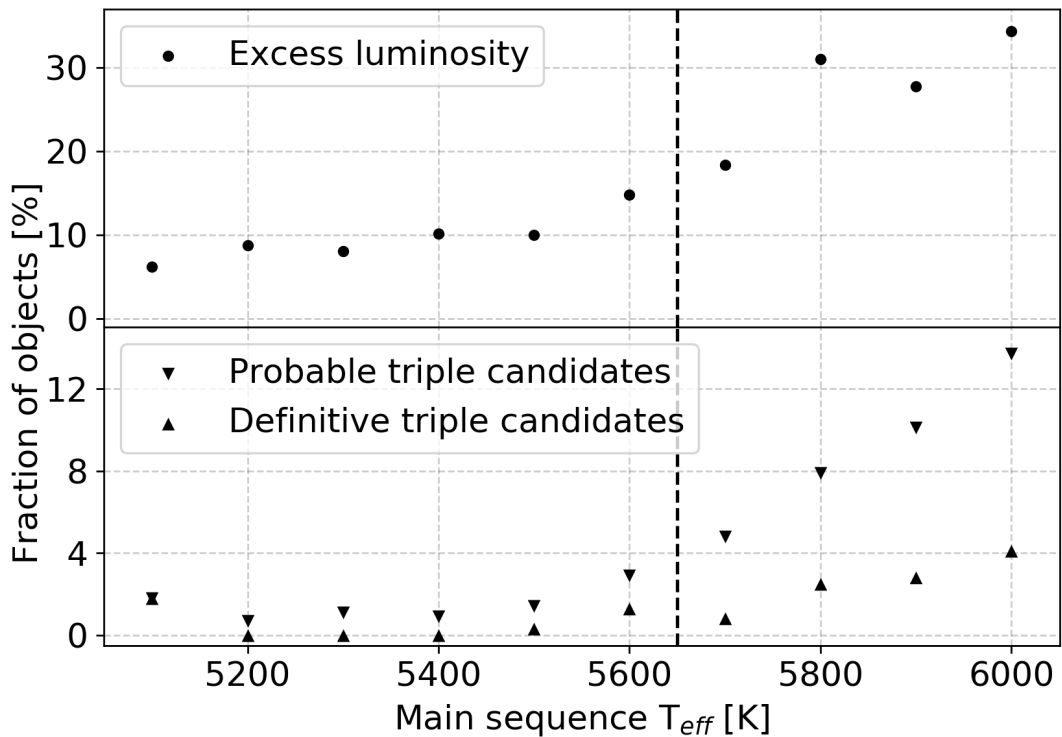


Figure 4.16: The upper panel shows the percentage of objects at different positions on the Kiel diagram shown in Figure 4.5 that show excessive luminosity and are spectroscopically similar to main sequence stars. Similarly, the lower panel shows upper and lower boundary on a percentage of triple system candidates at the same positions. For a definitive candidate, both fits must agree on a triple configuration. The strong dashed vertical line represents a point on Kiel diagram where the main sequence visually starts merging with the red-giant branch, the point where a region above the main sequence becomes polluted with more evolved stars.

surveys that show similar trends [35].

As the detected triple star candidates encompass a fairly small region in a colour-magnitude space, we were interested in the degree to which our analysed spectra are similar to those of other stars in the same region. For this purpose, the GALAH objects with absolute *Gaia* corrected magnitudes in the range  $3.3 < M_G < 3.6$  and  $0.77 < G_{BP}-G_{RP} < 0.84$  were selected and plotted in Figure 4.21, where spectra are arranged according to their similarity. In this 2D projection [details about the construction of which are given in 72, 84] it is obvious that spectra considered in this paper clearly exhibit a far greater degree of mutual similarity than other spectra with similar photometric signature. As expected, many of them lie inside the region of SB2 spectra. All of our Solar twin candidates were visually checked for the presence of a resolvable binary component. Nevertheless, this plot gives us additional proof of their absence as none of the analysed twins is located inside that region.

#### 4.9.4 Observational bias - Galaxia model

Every magnitude limited survey, such as the GALAH, will introduce observational bias into the frequency of observed binary stars as their additional flux changes the volume of the Galaxy from where they are sampled. Their distances and occupied volume of space is located further from the Sun and therefore also greater than for comparable single stars with the same apparent magnitude and colour.

To evaluate this bias for our type of analysed stars, we created a synthetic Milky Way population of single stars using the Galaxia code [94]. First, the code was run to create a complete population of stars in the apparent V magnitude range between 10 and 16 without any colour cuts. In order for the distribution of synthesized stars to mimic the GALAH survey as closely as possible, only stars located inside the observed GALAH  $2^\circ$  fields were retained. After the spatial filtering, only stars with Sun-like absolute magnitude  $M_V = 4.81 \pm 0.05$  and colour index  $B - V = 0.63 \pm 0.05$  were kept in the set [reference magnitudes were taken from 70].

From the filtered synthetic data set we took three different sub-sets representing a pool of observable single Solar twins ( $12.0 \leq V \leq 14.0$ ), binary twins ( $12.75 \leq V \leq 14.75$ ), and triple twins ( $13.2 \leq V \leq 15.2$ ) based on their apparent V magnitudes. Extinction and reddening were not used in this selection as their use did not significantly alter the relationship between the number of stars in sub-sets. Assuming that the frequency of multiple stars is constant and does not change in any of those sets, we can estimate the selection bias on the frequency of multiple stars. The number of stars in each sub-set was 15862, 35470, and 54567 respectively. According to those star counts, the derived frequency of binaries would be too high by a factor of 2.2 and a factor 3.4 for triple stars. Considering those factors, the fraction of unresolved triple candidates with Solar-like spectra is  $\sim 2\%$  and  $\sim 11\%$  for binary candidates.

Accidental visual binaries that lie along the same line-of-sight and have angular separation smaller than the field-of-view of the 2dF spectroscopic fiber ( $2''$ ) or smaller than the *Gaia* end-of-mission angular resolution ( $0.1''$ ) were not considered in this estimation.

## 4.10 Conclusions

Combining multiple photometric systems with spectroscopic data from the GALAH and astrometric measurements taken by *Gaia*, we showed the possible existence of triple stellar systems with long orbital periods whose combined spectrum mimics Solar spectrum. The average composition of such a system consists of three almost identical stars, where one of the stars is  $\sim 10$  K warmer than the Sun and the coldest has an effective temperature  $\sim 120$  K below the Sun. The derived percentage of such unresolved systems would be different for nearby/close stars as they become more/less spatially resolved. In the scope of our magnitude limited survey, we sampled only a fraction of possible distances to the systems.

Without any obvious signs of the orbital periodicity in the measured radial velocities of the systems, orbital periods were loosely constrained based on the observational limits and few assumptions. By the prior assumption that the *Gaia* spacecraft sees those systems as a single light source, we showed that they can be described by orbital periods where a difference between projected velocities of components does not sufficiently degrade an observed spectrum that it no longer recognized as Solar-like. The spectroscopic signature and radial velocity variations were further used to put a limit on the minimum orbital period of an inner pair to be at least 20 years. Shorter periods are not completely excluded as it could happen that the spectrum was acquired in a specific orbital phase where the difference between projected orbital speeds is negligible. From the fact that analysed objects are spatially unresolvable for the *Gaia* spacecraft, the orbital size of outer binary pair can extend up to 100-350 AU and therefore have orbital periods of order of a few hundred years.

To confirm their existence, detected systems are ideal candidates to be observed with precise interferometric measurements or high time-resolution photometers if they happen to be occulted by the Moon. Simulation of the lunar motion showed that four of the analysed multiple candidates lie in its path if the observations would be carried-out from the Asiago observatory that has suitable photon counting detectors.

The main drawback of the analysis was found to be its separate treatment of photometric and spectroscopic information in two independent fitting procedures. In future analyses, they should be combined to acquire even more precise results as different stellar physical parameters have a different degree of impact on these two types of measurements.

## 4.11 Table description and summary

In the Table 5.1 we provide a list of metadata available for every object detected using the methodology described in this paper. The complete table of detected objects and its metadata is available in electronic form at the CDS. An excerpt of the table, containing a subset of columns, for definitive and probable triple candidates is given in Table 4.7.

Table 4.6: List and description of the fields in the published catalogue of analysed objects.

Field	Unit	Description
<code>source_id</code>		<i>Gaia</i> DR2 source identifier
<code>sobject_id</code>		Unique internal per-observation star ID
<code>ra</code>	deg	Right ascension from <i>Gaia</i> DR2
<code>dec</code>	deg	Declination from <i>Gaia</i> DR2
<code>ruwe</code>		Value of re-normalized astrometric $\chi^2$
<code>m_sim_p</code>		Photometric $\chi^2$ for original parameters
<code>m_sim_f</code>		Spectroscopic $\chi^2$ for original parameters
<code>s1_teff1</code>	K	$T_{\text{eff}1}$ in a fitted single system
<code>s1_feh</code>		[Fe/H] of a fitted single system
<code>s1_sim_p</code>		Photometric $\chi^2$ of a fitted single system
<code>s1_sim_f</code>		Spectroscopic $\chi^2$ of a fitted single system
<code>s2_teff1</code>	K	$T_{\text{eff}1}$ in a fitted binary system
<code>s2_teff2</code>	K	$T_{\text{eff}2}$ in a fitted binary system
<code>s2_feh</code>		[Fe/H] of a fitted binary system
<code>s2_sim_p</code>		Photometric $\chi^2$ of a fitted binary system
<code>s2_sim_f</code>		Spectroscopic $\chi^2$ of a fitted binary system
<code>s3_teff1</code>	K	$T_{\text{eff}1}$ in a fitted triple system
<code>s3_teff2</code>	K	$T_{\text{eff}2}$ in a fitted triple system
<code>s3_teff3</code>	K	$T_{\text{eff}3}$ in a fitted triple system
<code>s3_feh</code>		[Fe/H] of a fitted triple system
<code>s3_sim_p</code>		Photometric $\chi^2$ of a fitted triple system
<code>s3_sim_f</code>		Spectroscopic $\chi^2$ of a fitted triple system
<code>n_stars_p</code>		Best fitting photometric configuration
<code>n_stars_f</code>		Best fitting spectroscopic configuration
<code>class</code>		Final configuration classification
<code>flag</code>		Result quality flags

Table 4.7: Subset of results for definitive and probable Solar-like triple candidates detected by our selection and fitting procedure. The complete table is given as a supplementary material to this paper in a form of the textual CSV file. It is also available in the electronic form at the CDS portal.

source_id	ruwe	s2_teff1	s2_teff2	s2_feh	s3_teff1	s3_teff2	s3_teff
6157059919188478720	11.1	6002	6000	0.24	5825	5787	5780
6777339306532222080	8.0	5875	5819	0.10	5642	5636	5631
6412815502155127808	1.1	5880	5316	-0.02	5922	4703	4701
6564302331580491904	1.1	5991	4701	0.13	5945	4702	4700
5386113598793714304	1.5	5882	5808	0.07	5878	5438	5313
2534579880633620992	1.2	5986	5876	0.15	5750	5739	5714
5484353352124904064	1.1	5876	5802	0.14	5844	5525	5425
5399712362903401984	1.3	5968	4703	0.08	5922	4703	4701
3688523450018482432	1.1	5820	5688	-0.015	5998	4717	4702
6220408320279116032	7.6	5923	5883	0.11	5724	5677	5669
6198738457927949440	0.9	6052	4798	0.15	5986	4704	4701
5822222074090352384	4.7	5651	5640	-0.04	5866	4702	4701
6355462192511955456	1.0	5700	5692	-0.11	5471	5449	5379
4678229218054642176	0.9	6028	4791	0.09	5968	4702	4700
4423111085550775680	1.6	5829	5774	-0.02	5645	5633	5398
6261736621608044416	4.7	5927	5890	0.07	6154	4702	4701
5947219160131475712	1.1	6071	5843	0.22	6007	5724	5265
6661888382295654656	1.5	5725	5678	-0.07	5956	4706	4701
6362136502970853120	1.8	5844	5826	0.013	5666	5658	5540
6645693508028329728	1.3	5936	4715	0.06	5833	4703	4701

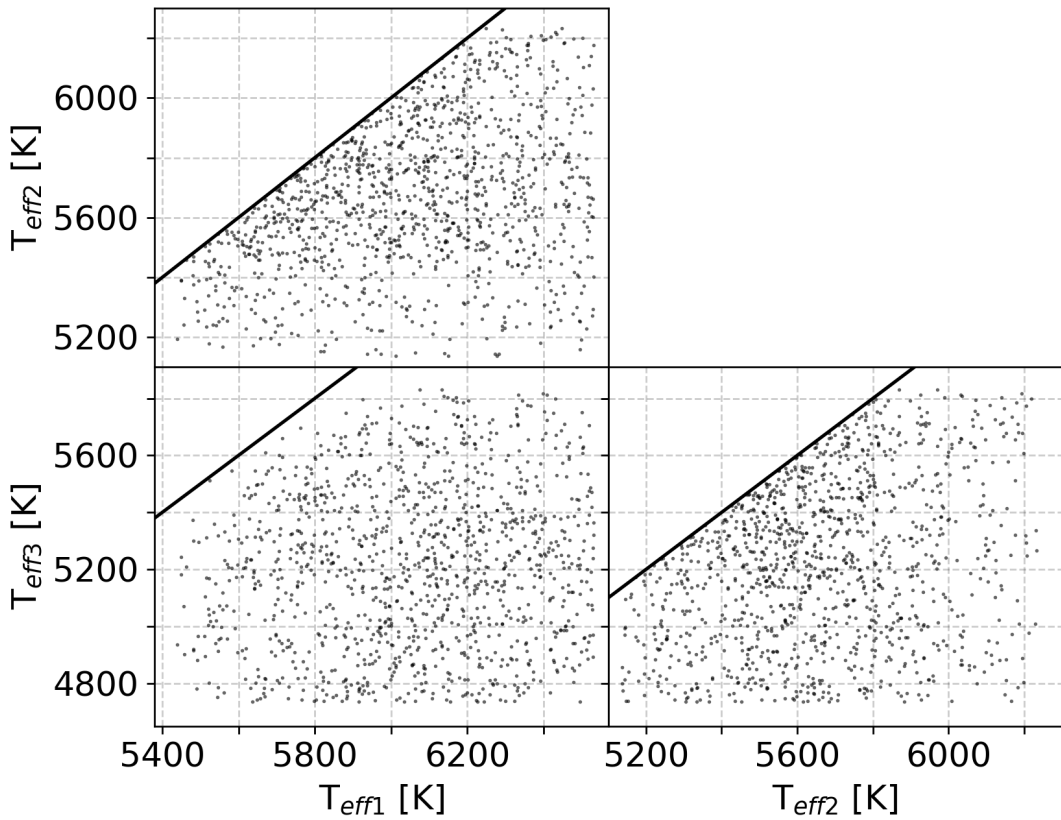


Figure 4.17: Initial distribution of walker parameters considered in the photometric fit. To ensure unique solutions with increasing  $T_{\text{eff}}$ , combinations above the linear line were not considered in the fit.

## 4.12 Additional figures

In order to increase the readability and transparency of the text, additional and repeated plots are supplied as appendices to the main text.

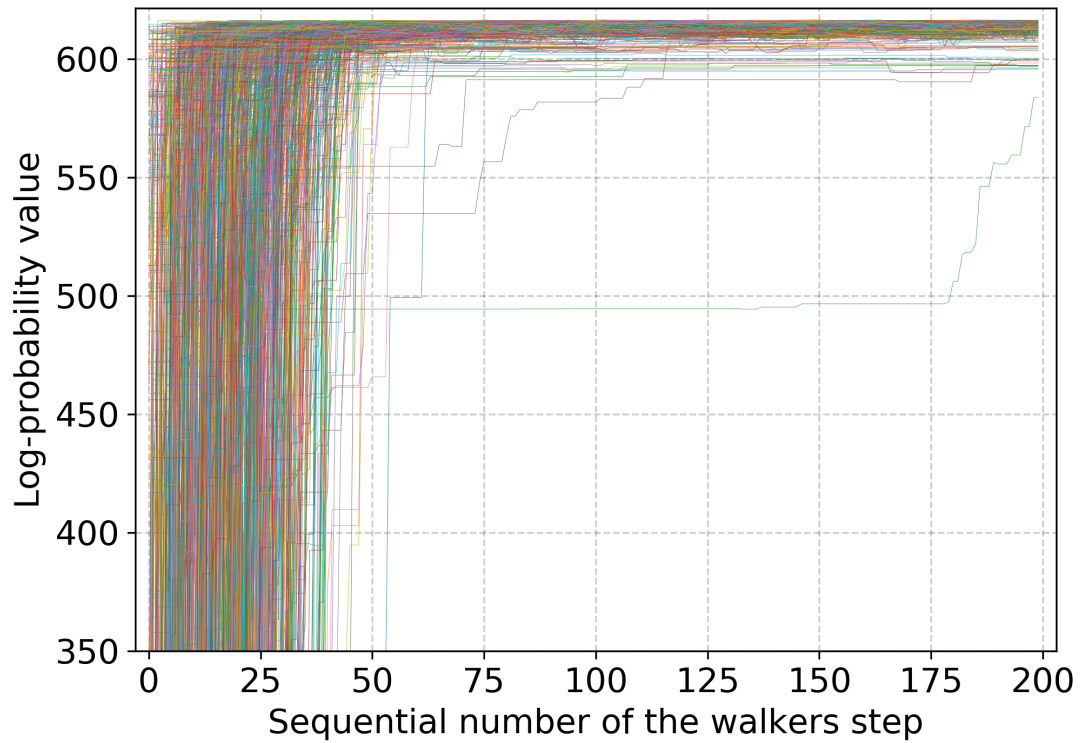


Figure 4.18: Convergence of walkers in the initial photometric fit. The plot shows a log-probability of the posteriors shown in the Figure 4.6. Walkers converge to the same value of log-probability after 50 steps. Every walker is plotted with different colour.

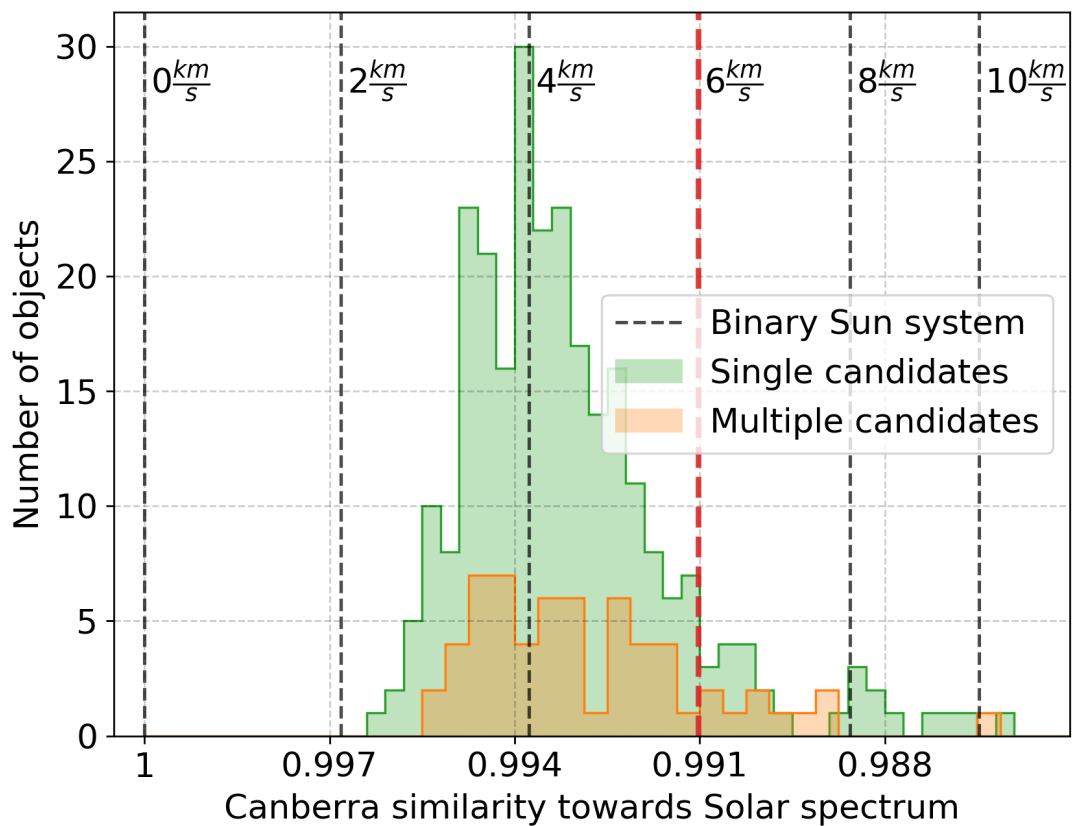


Figure 4.19: Same as Figure 4.14 but for the case of a triple system where only one component out of three has a radial velocity shift in comparison to other two.

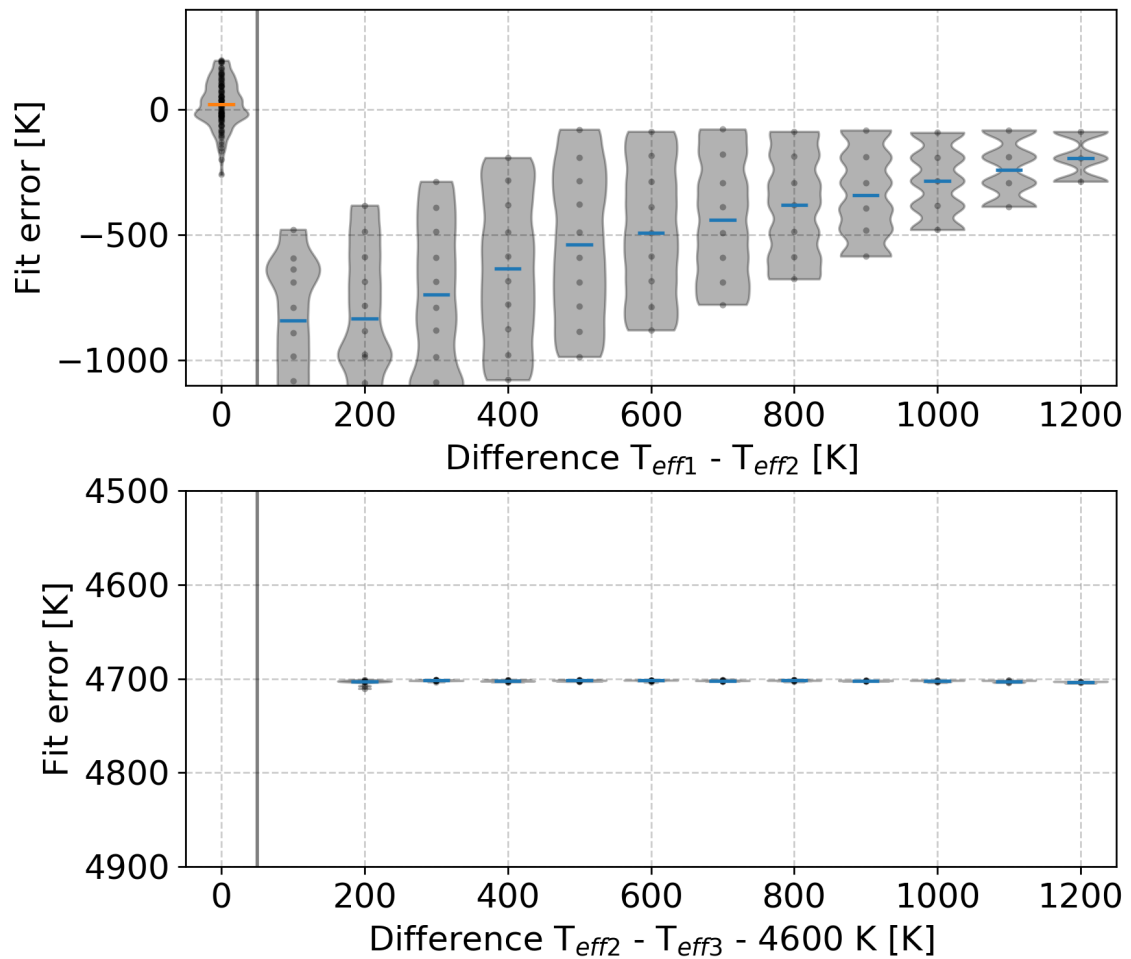


Figure 4.20: Similar to a plot in Figure 4.15, but representing a case when we try to describe a synthetic binary system with  $T_{eff3} = 0$  using a triple star model.

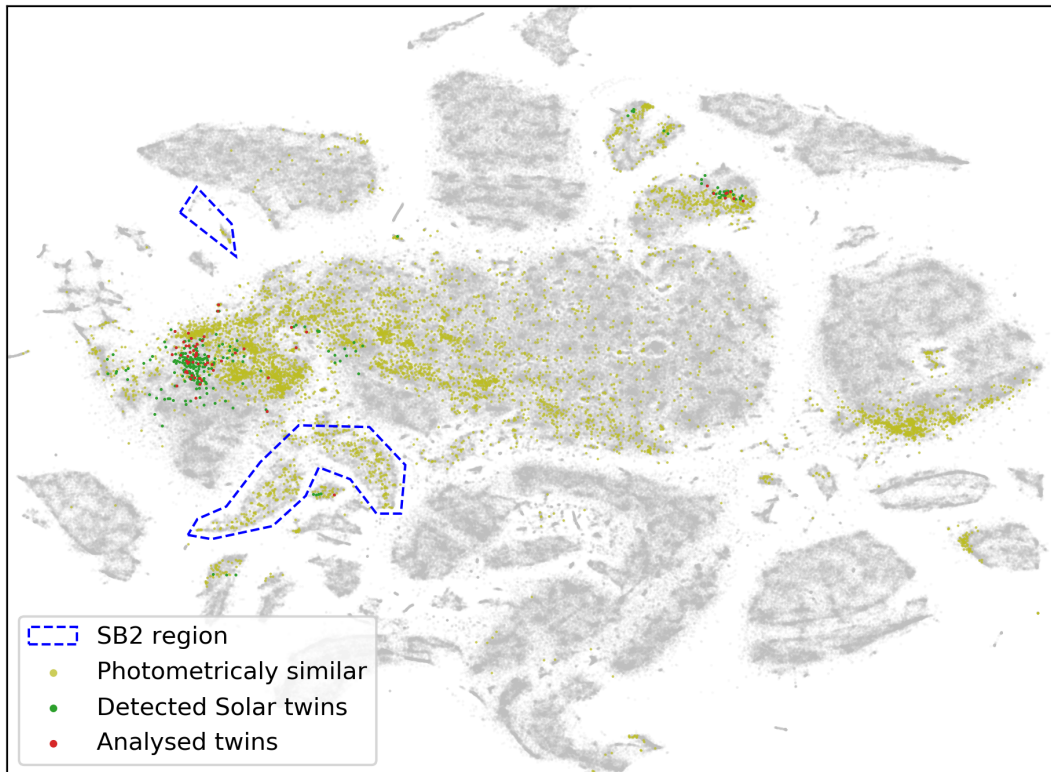


Figure 4.21: Visual representation of similarities between spectra using dimensionality reduction analysis. Clumps in this 2D projection represent morphologically similar spectra, whose features separate them from the rest of the data set. Blue-dashed polygons indicate over-densities, where SB2 spectra are located [projection and regions are taken from Figure 13 in 72]. Each grey dot represent one spectrum of GALAH survey. Green coloured dots represent objects considered in this paper, of which objects marked with red were analysed for higher order multiplicity. Yellowish dots represent objects whose *Gaia* magnitudes fall inside the range of determined triple star candidates.



# Chapter 5

## Peculiar stars

### 5.1 Abstract

Swan bands – characteristic molecular absorption features of the C<sub>2</sub> molecule – are a spectroscopic signature of carbon-enhanced stars. They can also be used to identify carbon-enhanced metal-poor (CEMP) stars. The GALAH (GALactic Archaeology with Hermes) is a magnitude-limited survey of stars producing high-resolution, high signal-to-noise spectra. We used 627,708 GALAH spectra to search for carbon-enhanced stars with a supervised and unsupervised classification algorithm, relying on the imprint of the Swan bands. We identified 918 carbon-enhanced stars, including 12 already described in the literature. An unbiased selection function of the GALAH survey allows us to perform a population study of carbon-enhanced stars. Most of them are giants, out of which we find 28 CEMP candidates. A large fraction of our carbon-enhanced stars with repeated observations show variation in radial velocity, hinting that there is a large fraction of variables among them. 32 of the detected stars also show strong Lithium enhancement in their spectra.

### 5.2 Introduction

Chemically peculiar stars whose spectra are dominated by carbon molecular bands were first identified by Secchi [95]. Their spectra are characterised by enhanced carbon absorption bands of CH, CN, SiC<sub>2</sub>, and C<sub>2</sub> molecules, also known as Swan bands. Possible sources of enhancement are dredge-up events in evolved stars [96], enrichment by carbon-rich stellar winds from a pulsating asymptotic giant branch (AGB) star, which settles on a main sequence companion [97], or it can be the result of a primordial enrichment [98]. Historically, high latitude carbon stars, presumed to be giants, were used as probes to measure the Galactic rotation curve [99], velocity dispersion in the Galactic halo [100], and to trace the gravitational potential of the Galaxy.

Because of their strong spectral features, the most prominent candidates can easily be identified from large photometric surveys [101, 102]. Specific photometric systems [103, 104, 105] were defined in the past to discover and further classify stars with enhanced carbon features in their spectra. Specifics of those systems were catalogued, compared, and homogenised by Moro and Munari [106] and Fiorucci and Munari [107].

Other useful data come from low-resolution spectroscopic surveys, whose classification identified from a few hundred to a few thousand of those objects [108, 109, 110, 111, 112]. High-resolution spectroscopy is required to search for candidates with less pronounced molecular absorption features or to determine their stellar chemical composition. Multiple studies have been carried out to determine accurate abundances of metal-poor stars [113, 114, 115, 116, 117, 118, 119, 120, 121, 122, 123, 124]. Such detailed abundance information is especially important for the analysis and classification of chemically peculiar objects [125].

Today, the most sought after, of all carbon-enhanced stars, are the carbon-enhanced metal-poor (CEMP) ones whose fraction, among metal-poor stars, increases with decreasing metallicity [M/H] [110, 113, 126, 127, 128, 129, 130, 131, 132, 133, 134, 135, 136]. Amongst these, those near the main-sequence turn-off are expected to be of particular importance, as they may have accreted enough material from their AGB companion to produce an observable change in their atmospheric chemical composition [123, 137, 138]. The accreted material could provide insight into the production efficiency of neutron capture elements in AGB stars [118]. Multiple studies show that a peculiar observed abundance pattern and carbon enrichment in a certain type of CEMP stars could be explained by the supernova explosions of first-generation stars that enriched the interstellar medium [139, 140, 141, 142]. The exact origin and underlying physical processes governing multiple classes of CEMP stars are not yet fully understood and are a topic of ongoing research [98, 143, 144]. Classification into multiple sub-classes is performed using the abundance information of neutron-capture elements [98, 145, 146, 147] that are thought to originate from different astrophysical phenomena responsible for the synthesis of those elements.

In this work, we propose a novel approach for the classification of carbon-enhanced stars using high-resolution stellar spectra covering parts of the visible domain. The goal is to identify a representative sample of carbon-enhanced stars, which can be used as an input to population studies. The paper is organised as follows; we start with a brief discussion of our spectroscopic observations and their reduction (Section 5.3), which is followed by the description of the used algorithms for the detection of carbon-enhanced stars in Section 5.4. Properties of the classified objects are investigated in Section 5.5, CEMP candidates are a focus of Section 5.6, with Section 5.7 describing a follow-up study for one of them. Final remarks are given in Section 5.8.

### 5.3 Data

The analysed set of stellar spectra was acquired by the High Efficiency and Resolution Multi-Element Spectrograph (HERMES), a fibre-fed multi-object spectrograph on the 3.9 m Anglo-Australian Telescope (AAT) of the Australian Astronomical Observatory. The spectrograph [21, 22] can simultaneously record spectra from up to 392 fibres distributed over a  $2^\circ$  field of the night sky, with an additional 8 fibres used for the telescope guiding. The spectrograph has a resolving power of  $R \sim 28,000$  and consists of four spectral arms centred at 4800, 5761, 6610, and 7740 Å, together covering approximately 1000 Å, including the H $\alpha$ , and H $\beta$  lines. Three dichroic beam splitters are used to separate incoming light into four separated colour beams that are analysed independently. The spectrograph can typically achieve a signal to noise ratio (SNR)  $\sim 100$  per resolution element at magnitude V=14 in the red arm

during a 1-hour long exposure.

Spectra used in this study have been taken from multiple different observing programmes using this spectrograph: the GALactic Archaeology with HERMES (GALAH) pilot survey [148], the main GALAH survey [19], the K2-HERMES survey [149], and the TESS-HERMES survey [24]. Most of those observing programmes exclude fields close to the Galactic plane (due to problems with high stellar density and Galactic extinction) or far away from it (not enough suitable targets to use all fibres), employ subtle different selection functions (position, limiting magnitude, crowding requirement, and photometric quality), but share the same observing procedures, reduction, and analysis pipeline [internal version 5.3, 25]. All programmes, except the pilot survey, are magnitude-limited, with no colour cuts. This leads to an unbiased sample of stars distributed mostly across the southern sky that can be used for different population studies. Additionally, all objects from different observing programmes are analysed with the same procedure named *The Cannon* [internal version 180325, 71, 72], so their stellar parameters are determined in a consistent manner and are hence comparable across the different programmes. *The Cannon* algorithm employs a data-driven interpolation approach trained on a set of high-quality benchmark stars spanning the majority of the stellar parameter space [for details, see 72].

The spectrum synthesis code Spectroscopy Made Easy [SME, 30, 31] was run on the spectra in the training set to determine their stellar parameters and atmospheric chemical abundances. These values were used to train *The Cannon* model, which was then run on every observed spectrum to determine its stellar parameters. Every determined parameter is accompanied by a quality flag identifying its usefulness and possible problems with grid interpolation. Therefore, we can easily remove parameters that were determined for stellar spectra far away from the training set or with possible problems in any of the HERMES spectral arms. An interpolation method proved beneficial in determining stellar physical parameters and up to 23 abundances (extendable up to 31 in future versions) for every analysed star, as described in Buder *et al.* [72]. The parameter [Fe/H] determined by *The Cannon* refers to an iron abundance and not overall metallicity [M/H] as often used in the literature. As both notations are used interchangeably in the literature to describe stellar metallicity, care must be taken when comparing those two measurements.

*The Cannon* approach has an advantage of treating stars with a peculiar composition, such as carbon-enhanced stars, in a consistent manner with common objects, thus avoiding arbitrary jumps or offsets that would depend on a degree of peculiarity or correctness of physics of the underlying model. As a data-driven approach, it only projects the learned training set onto the whole survey based on quadratic relations to stellar parameters.

Our data set consists of 627,708 successfully reduced spectra of 576,229 stars observed between November 2013 and February 2018.

## 5.4 Detection procedure

To search for carbon-enhanced stars in the GALAH data set we focused on spectral features that can be clearly distinguished and are known markers of carbon enhancement. Instead of using one very weak atomic carbon absorption line (at 6587.61 Å), used by *The Cannon* to determine [C/Fe] abundance, we focused on a

region between 4718 and 4760 Å observed in the blue arm that covers 4718–4903 Å in its rest-frame. In this range we can, depending on the radial velocity of the star, observe at least four Swan band features [150] with their band heads located at approximately 4715, 4722, 4737, and 4745 Å.

Carbon enhancement is observable in spectra as a strong additional absorption feature (Figure 5.1) that is the strongest at the wavelength of the band’s head. After that its power gradually decreases with decreasing wavelength. The most prominent and accessible for all of the spectra is a feature located at 4737 Å, produced by a  $^{12}\text{C}^{12}\text{C}$  molecule. If other carbon features, like the one produced by a  $^{13}\text{C}^{12}\text{C}$  molecule at 4745 Å (shown in Figure 5.16) are present in the spectrum, the carbon isotope ratio  $^{12}\text{C}/^{13}\text{C}$  in a star can be determined. Its determination was not attempted in the scope of this paper.

Detection of spectral features was tackled using two different classification procedures. First, a supervised procedure was used to identify the most prominent spectra with carbon enhancement. It is based on the assumption that we know where in the spectra those features are located and how they behave. This was augmented with an unsupervised dimensionality reduction algorithm that had no prior knowledge about the desired outcome. The goal of a dimensionality reduction was to transform n-dimensional spectra onto a 2D plane where differences between them are easier to analyse. The unsupervised algorithm was able to discern the majority of carbon-enhanced spectra from the rest of the data set and enabled us to discover spectra with less prominent carbon enhancement features.

#### 5.4.1 Supervised classification

To search for additional absorption features that are usually not found in spectra of chemically normal stars, we first built a spectral library of median spectra based on a rough estimates of stellar physical parameters derived by the automatic reduction pipeline, described in detail by Kos *et al.* [25]. The median spectrum for every observed spectrum in our data set was computed from physically similar spectra with stellar parameters in the range of  $\Delta T_{\text{eff}} = \pm 75$  K,  $\Delta \log g = \pm 0.125$  dex and  $\Delta [\text{Fe}/\text{H}] = \pm 0.05$  dex around the stellar parameters of the investigated spectrum. The median spectrum was calculated only for observed targets with at least 5 similar spectra in the defined parameter range and with minimal SNR=15 per resolution element, as determined for the blue spectral arm. All considered spectra were resampled to a common wavelength grid with 0.04 Å wide bins and then median combined. The normalisation of the spectra along with the radial velocity determination and the corresponding shift to the rest frame was performed by the automatic reduction pipeline [25]. We checked that spectral normalisation and radial velocity determination are adequate also for carbon-enhanced stars. The normalisation procedure is done using a polynomial of low-order that is not strongly affected by the Swan band features or similar spectral structures. The radial velocity of a star is determined as an average of radial velocities that were independently determined for the blue, green, and red spectral arm. If one of the arms has a radial velocity deviating for more than two times the difference between the other two, it is excluded from the average [further details in 25]. Therefore the final velocity should be correct even if one of those arms contains features that are not found in the set of reference spectra used in the cross-correlation procedure.

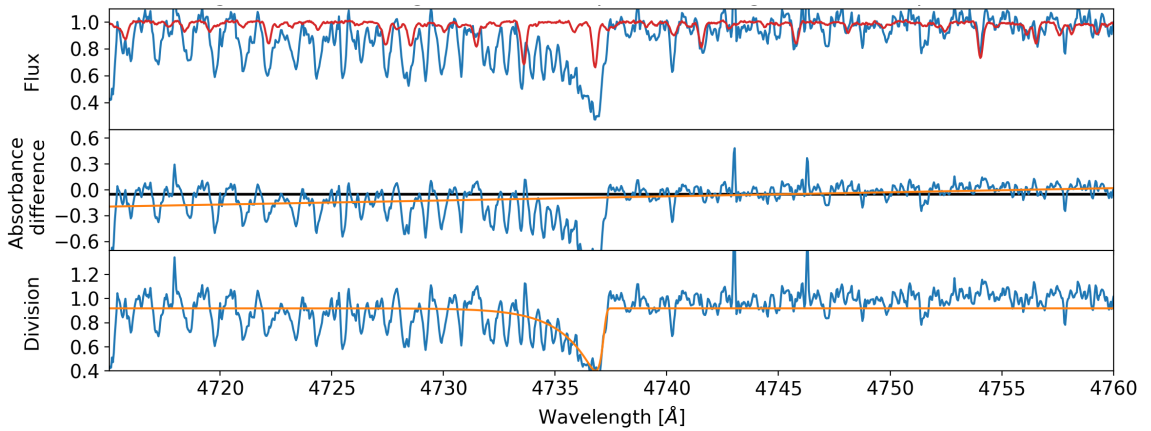


Figure 5.1: Example of a metal-poor carbon-enhanced candidate with strong Swan absorption feature at  $4737 \text{ \AA}$ , caused by the carbon  $\text{C}_2$  molecules. The first panel shows the stellar spectrum in blue and a corresponding reference median spectrum in red. The reference median spectrum was computed as the per-pixel median flux value of spectra with similar stellar parameters as the spectrum shown in blue. The spectral difference (second panel) and division (third panel) were computed from those two spectra. The middle panel shows in orange a linear fit to the spectral difference that was used to identify spectra with the reduction problems on the blue border of the spectral range. The median value of the spectral difference is given by the black horizontal line. The orange curve in the last panel shows a fit that was used to determine the strength of the observed carbon feature. The shown spectrum belongs to a star with a Two Micron All-Sky Survey (2MASS) identifier J11494247+0051023 and iron abundance  $[\text{Fe}/\text{H}]$  of  $-1.17$ , as determined by *The Cannon*.

With the limitation of at least 5 spectra used for the computation of the median spectrum, some possibly carbon-enhanced stars, could be excluded from the supervised classification. The final number of spectra analysed by this method was 558,053.

Spectra, for which we were able to determine the median spectrum of physically similar objects, were analysed further. In the next step, we tried to determine possible carbon enhancement by calculating a flux difference and flux division between the observed stellar and median spectra, as shown in Figure 5.1.

In order to describe the position, shape, and amplitude of the Swan feature with its head at 4737 Å, we fitted a function that is based on a Log Gamma ( $\log \Gamma$ ) distribution. The distribution, with three free parameters, was fitted to the division curve, where the Swan feature is most pronounced. Division curve, shown in the bottom panel of Figure 5.1, was computed by dividing observed spectrum with its corresponding median spectrum. The fitted function  $f$  can be written as:

$$f(\lambda) = f_0 - \log \Gamma(\lambda, S, \lambda_0, A). \quad (5.1)$$

The shape of the curve is defined by an offset  $f_0$ , shape parameter  $S$ , centre wavelength  $\lambda_0$ , and amplitude  $A$  of  $\log \Gamma$  distribution, where  $\lambda$  represents rest wavelengths of the observed spectrum. This function was selected because of its sharp rise followed by the gradual descent that matches well with the shape of a residual absorption observed in the Swan regions. The steepness of the rising part is determined by the parameter  $S$  (lower value indicates steeper raise) and its vertical scaling by the parameter  $A$ . We are not aware of any other profile shapes used for fitting Swan bands in the literature.

To narrow down possible solutions for the best fitting curve, we used the following priors and limits. The initial value for the parameter  $f_0$  was set to a median of all pixel values in the division curve and allowed to vary between 0.5 and 1.5. The limiting values are however never reached. The centre of the  $\log \Gamma$  distribution  $\lambda_0$  was set to 4737 Å and was allowed to vary by 2 Å. Wavelength limits were set to minimise the number of mis-fitted solutions, where the best fit would describe the nearby spectral absorption lines not present in the median spectra or problematic spectral feature caused by the spectral data reduction as shown by Figure 5.18. We did not set any limits on parameters  $A$  and  $S$  in order to catch fitted solutions describing a spectrum difference that is different from the expected shape of the molecular absorption band.

By integrating the surface between the offset  $f_0$  and the fitted curve we calculated the strength of the Swan band. The integral (`swan_integ` in Table 5.1) is derived between 4730 and 4738 Å. It should not be used as a substitute for a carbon abundance measurement, but only to sort the detections of carbon-enhanced stars by their perceivable strength of the Swan band.

With so many spectra in our data set, unexpected reduction and analysis problems can hinder the selection of carbon-enhanced stars. In the first iteration, the results were ordered only by the value of the integrated Swan band region, but this proved to select too many spectra with reduction problems. Most of the problematic detections were caused by the incorrect normalisation of spectra with strong, non-carbon molecular bands. This is best observable at the border of a spectral range, where Swan bands are located in the case of HERMES spectra. There, normalisation can be poorly defined in the case of numerous nearby absorption lines.

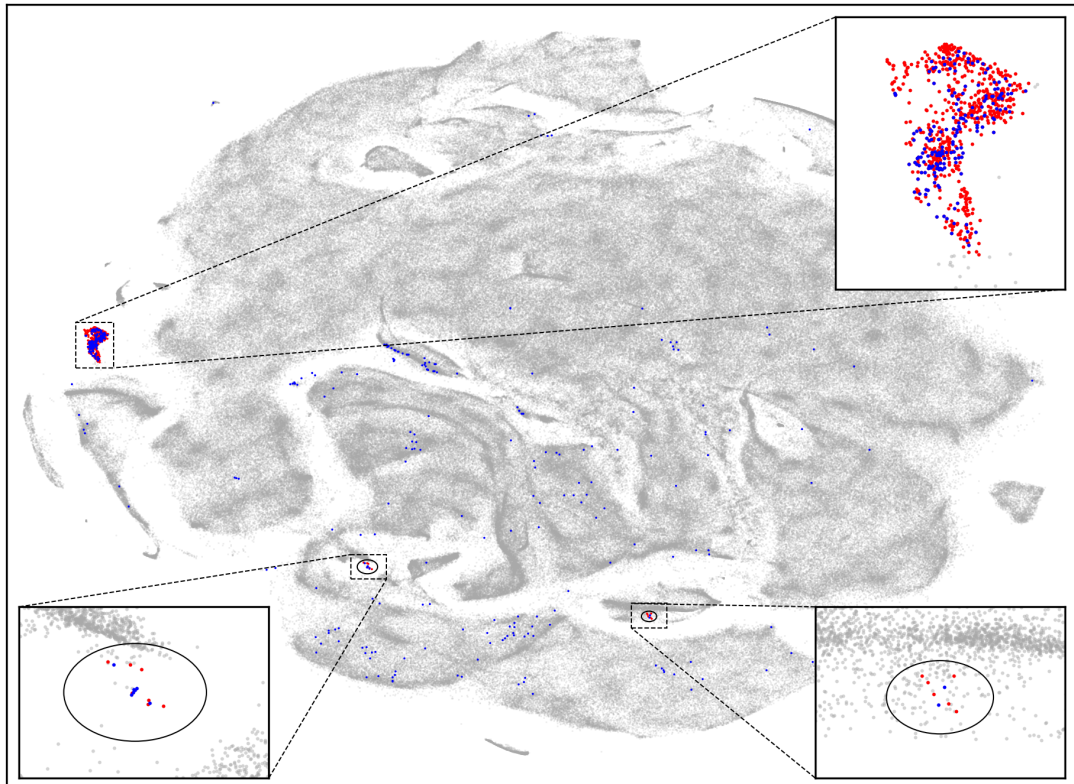


Figure 5.2: t-SNE projection of 588,681 observed spectra ranging between 4720 and 4890 Å. Red dots (756 spectra) mark a clump in the projection that was manually selected to contain carbon-enhanced spectra. Superimposed blue dots represent carbon-enhanced spectra determined by the supervised algorithm. Outside the t-SNE selected clump, we have 224 spectra that were determined to be carbon-enhanced only by the supervised method. All other analysed spectra are shown in grey shades, depending on their density in the 2D projection. Two ellipses indicate regions where the majority of CEMP candidates is located in the projection.

In order to prevent miss-detections, additional limits on the shape ( $S \leq 1$ ) and amplitude ( $A \leq 1$ ) of the  $\log \Gamma$  distribution were used to filter out faulty fitting solutions. Figure 5.19 represents one such example where the function  $f(\lambda)$  was fitted to the absorption lines of a double-lined spectroscopic binary, producing a shape of the function that is not characteristic for the analysed molecular band head. To remove spectra with reduction problems or peculiarity that would result in wrongly determined strength of the Swan band, we are also analysing the slope of the spectral difference and its integral in the limits of the Swan bands. One of the spectral trends that we are trying to catch with those indicators is shown in Figure 5.19, where spectral difference and its linear fit are steeply rising at the border of the spectrum.

By visual inspection of the algorithm diagnostic plots shown in Figure 5.1, we limited a final selection to 400 spectra with the strongest carbon enhancement that was still visually recognisable. The last selected spectrum is shown in the Figure 5.17. Selection of spectra with lower enhancement, would introduce possibly wrong classification of stars whose enhancement is driven by spectral noise levels, data reduction or any other process that has subtle effect on the spectral shape.

### 5.4.2 Unsupervised classification

With numerous spectra of different stellar types, chemical composition, and degree of carbon enhancement, some of them might show different carbon features or be insufficiently distinctive to be picked out by the above supervised algorithm.

Another analysis technique, which is becoming increasingly popular is a dimensionality reduction procedure named t-distributed Stochastic Neighbor Embedding [t-SNE, 151], that has already proved to be beneficial in comparison and sorting of unknown spectral features of the same data set [84]. This is done by projecting the complete spectra onto a 2D plane by computation of similarities between all pairs of investigated spectra. It has been shown that the algorithm can cluster and distinguish spectra with absorption or emission features. The algorithm arranges spectra in a 2D plane, such that it clusters similar spectra together based on their similarity measure. As the transformation is variable and non-linear, the actual distance between two objects in a final 2D plane does not linearly depend on the spectral similarity measure. This property of the t-SNE algorithm ensures more homogeneous coverage of the 2D plane in comparison to other dimensionality reduction methods.

The t-SNE projection shown in Figure 5.2 was computed from normalised spectra between 4720 and 4890 Å. To maximise the number of analysed spectra, no other limiting cuts than the validity of the wavelength solution [bit 1 in `red_flag` set to 0 by reduction pipeline, 25] in this arm was used. This resulted in 588,681 individual spectra being analysed by the automatic unsupervised algorithm. This is  $\sim 30k$  more spectra than in the case of supervised classification, where we applied more strict criteria for the selection of analysed spectra (Section 5.4.1).

Without any prior knowledge about the location of objects of interest in the obtained projection, we would have to visually analyse every significant clump of stars in order to discover whether the carbon-enhanced population is located in one of them. This can be simplified by adding the results of the supervised classification into this new projection. In Figure 5.2, the stars identified by the supervised classification are shown as blue dots plotted over grey dots representing all spectra

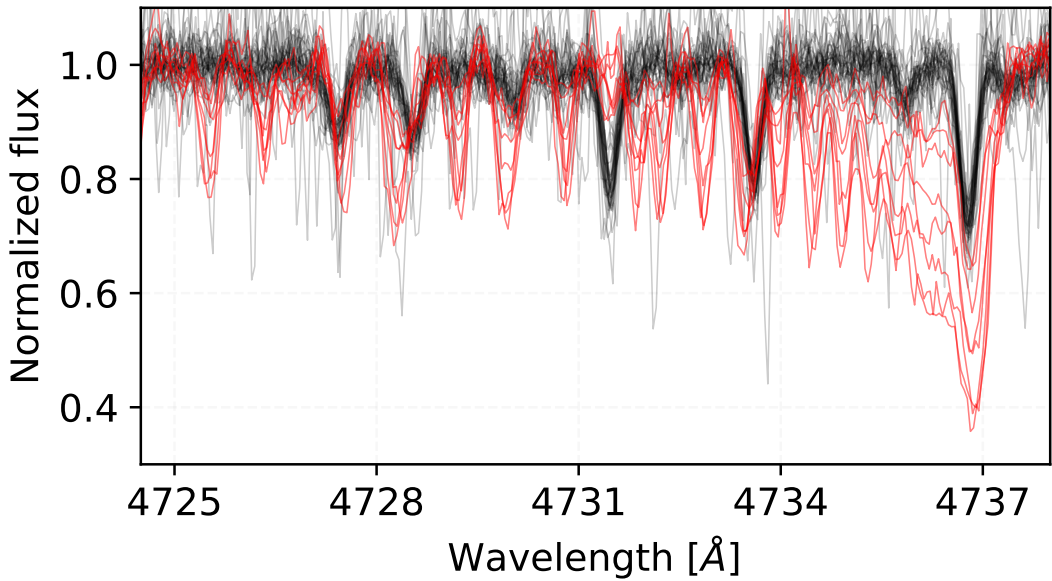


Figure 5.3: A collection of spectra that were determined to be mutually very similar by the t-SNE algorithm. Out of 46 spectra inside the right black ellipse in Figure 5.2 we identified 8 carbon-enhanced spectra with visually very different and distinctive spectrum in the region from 4734 to 4737 Å that is also depicted in this figure. For easier visual recognizability, they are coloured in red.

that went into the analysis. The majority of blue dots are located in a clump on the left side of the projection. A high concentration of objects detected by a supervised method leads us to believe, that this isolated clump represents carbon-enhanced objects in the t-SNE projection. To select stars inside the clump, we manually drew a polygon around it.

Inspection of other blue labelled spectra outside the main clump revealed that their slight carbon enhancement could not be identified by the t-SNE similarity metric as the spectra comparison might have been dominated by another spectral feature.

Additional exploration of the t-SNE projection revealed two smaller groups of metal-poor carbon-enhanced spectra located inside ellipses shown in Figure 5.2. A confirmation that those regions are populated with metal-poor stars can be found in Figure 5.14 where the dots representing spectra in the projection are colour coded by  $[Fe/H]$  and  $T_{eff}$ . To maximise the number of those objects in the published catalogue, we manually checked all undetected spectra in the vicinity of the detected ones. This produced additional 13 CEMP detections.

### t-SNE limitation

While checking the local neighbourhood of some of the blue dots in Figure 5.2 that are strewn across the t-SNE projection we identified a possible limitation of our approach for the automatic detection of specific peculiar spectra if their number is very small compared to the complete data set. Figure 5.3 shows a collection of a few carbon-enhanced spectra embedded between other normal spectra that were taken

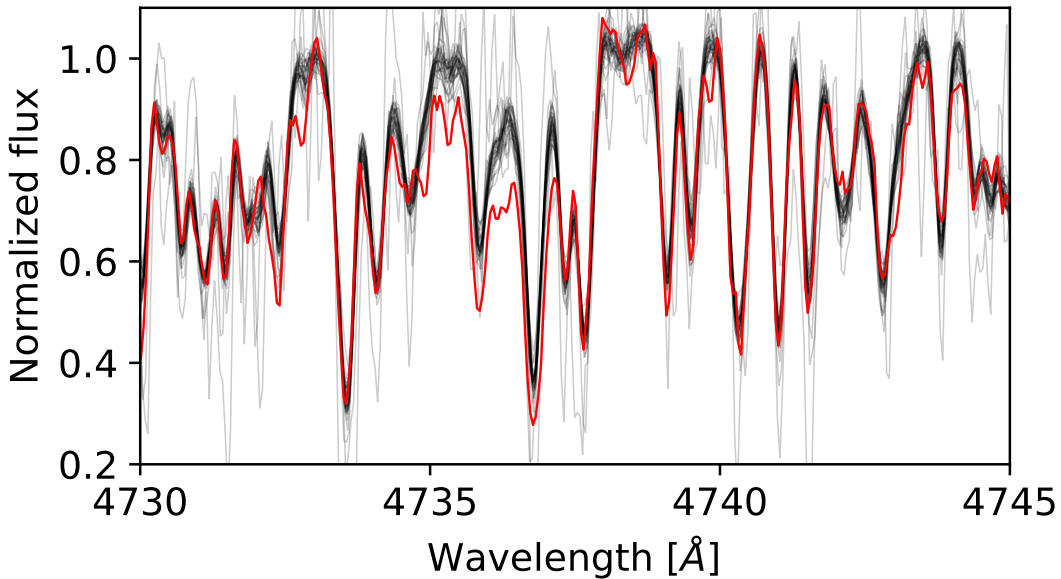


Figure 5.4: Spectral comparison between one of the detected carbon-enhanced stars in red and its 30 closest neighbours in the t-SNE projection shown as black curves. Enhancement in the spectrum was probably not sufficiently distinct and was dominated by the spectral noise. Therefore the spectrum was placed among other physically similar spectra without visible enhancement.

out of the right ellipsoidal region in Figure 5.2. As they are quite different from the others they were pushed against the edge of a larger cluster in the projection, but their number is not sufficient to form a distinctive group of points in the projection. Therefore any automatic algorithm that would try to distinguish those objects based solely on a local density of points would most probably fail.

Another specific of the t-SNE projection that we must be aware of is how it computes the similarity between analysed spectra. Combined similarity, which is computed as a sum of per pixel differences, has zero knowledge about the location where in the spectrum those differences occur. The red spectrum in Figure 5.4 with a slight signature of carbon enhancement in the range between 4734 and 4737 Å has been placed among spectra with similar physical properties. Its slight carbon enhancement and comparable spectral noise to other spectra in its vicinity are probably the reason why it was placed in such a region of the t-SNE projection. This could be solved by using a smaller portion of the spectrum in a dimensionality reduction, which could at the same time lead to a loss of other vital information about a star.

## 5.5 Candidate characteristics

The final list of detected carbon-enhanced stars consists of 918 stars, corresponding to 993 spectra detected by at least one of the described methods. Among them, 63 stars were observed and identified at least twice and up to a maximum of four times. Those identifications belong to repeated observations that were performed

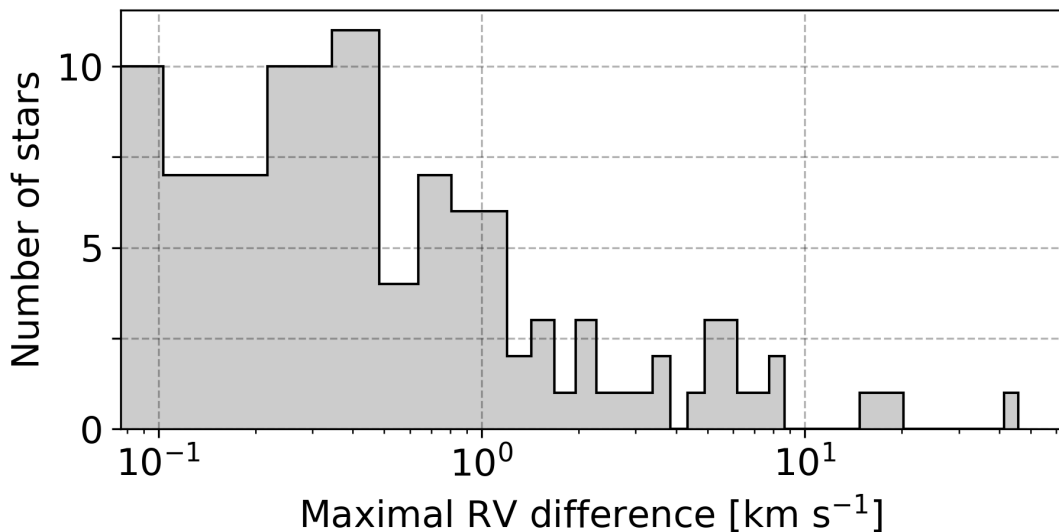


Figure 5.5: Distribution of maximal velocity change between repeated observations of the stars that were classified as carbon-enhanced.

at different epochs. Because not all of the observed spectra were considered in the classification procedure (due to the limitations described in Section 5.4) this is not the final number of stars with repeated observations. By searching among the complete observational data set, the number of carbon-enhanced stars with repeated observations increases to 90.

Out of those 90 stars, every repeated observation of 56 stars was classified as being carbon-enhanced. In total, we detected 76.5 % of the carbon-enhanced spectra among repeated observations where at least one of the repeats have been classified as having enhanced carbon features in its spectrum. The unclassified instances usually have a low SNR value that could decrease their similarity value towards other carbon-enhanced stars in the t-SNE analysis or have incorrect stellar parameters and were therefore compared to an incorrect median spectra during the supervised analysis.

### 5.5.1 Radial velocity variations

With repeated observations in the complete observational data set, we can look into measured radial velocities and investigate a number of possible variables that should be high for certain types of carbon-enhanced objects [152]. Taking into account all of the repeated observations in our data set and not just the repeats among the identified spectra, 52 out of 90 stars show a minimum velocity change of  $0.5 \text{ km s}^{-1}$  (70 stars with minimum change of  $0.25 \text{ km s}^{-1}$ ) and a maximum of  $45 \text{ km s}^{-1}$  in different time spans ranging from days to years. The detailed distribution is presented by Figure 5.5. That kind of change can hint at the presence of a secondary member or at intrinsic stellar pulsation [153, 154, 155], as carbon-enhanced stars are found among all long period variable classes [Mira, SRa, and SRb, 156, 157]. Follow-up observations are needed to determine their carbon sub-class and subsequently the reason behind variations of radial velocity.

Visual inspection of variable candidates revealed that none of them shows ob-

vious multiplications of absorption spectral lines, a characteristic of a double-lined binary system. Therefore we can conclude that none of them is a binary member in which both components are of comparable luminosity and a difference between their projected radial velocities is high enough to form a double-lined spectrum. From our simulations with median spectra, such line splitting becomes visually evident at the velocity difference of  $\sim 14 \text{ km s}^{-1}$ . If the components do not contribute the same amount of flux, the minimal difference increases to  $\sim 20 \text{ km s}^{-1}$ .

Chemical peculiarity of a dwarf carbon-enhanced star (dC) that exhibits enhancement of  $C_2$  in its spectra could be explained by its interaction with a primary star in a binary system [158]. Chemically enhanced material is thought to be accreted from the evolved AGB companion. Less than thirty of such systems, that show signs of the existence of an invisible evolved companion who might have enriched a dC by the carbon, have been identified spectroscopically to date [158, 159, 160], giving us the possibility to greatly increase the list with every additional confirmed object. The only detected dC star (for criteria see Section 5.5.2) with repeated observations shows that its radial velocity is unchanged on the order of  $0.1 \text{ km s}^{-1}$  during the 2 years between consecutive observations. Hence, it cannot be classified as a possible binary system from those two observations alone. The lack of a clear evidence for binarity among dC stars, especially among the most metal-poor, can also be explained by another enrichment mechanism. Farihi *et al.* [161] showed that a substantial fraction of those stars belongs to the halo population based on their kinematics information. Combined with the results of Yoon *et al.* [98] that classified the prototype dC star G 77-61 as a CEMP-no star, that are known to have intrinsically low binarity fraction [138, 162], their carbon-enhancement may be of a primordial origin.

### 5.5.2 Stellar parameters

For the analysis of stellar parameters, we used values determined by *The Cannon* data interpolation method that was trained on actual observed HERMES spectra. To exclude any potentially erroneous parameter, we applied a strict flagging rule of `flag_cannon=0` [an extensive description of flagging procedure can be found in 72], thus obtaining a set of 347 objects with trustworthy stellar parameters. Such a large percentage of flagged objects could be attributed to their nature as an additional elemental enhancement that we are looking for might not be a part of the training set. A raised quality flag would hint that the spectrum is different from any other in the training set or that the fit is uncertain and has a large  $\chi^2$ . Therefore flagged parameters have to be used with care, especially on the border of, and outside the training set.

The majority (338) of the unflagged detected objects are giants and only 9 are confirmed to be dwarf stars based on their spectroscopic stellar parameters (Figure 5.6).

### 5.5.3 S-process elements

Focusing on a spectral signature of the detected objects inside and outside the t-SNE selected clump (Figure 5.2) we can further investigate which spectral feature might have contributed to their separation. The distributions of their abundances

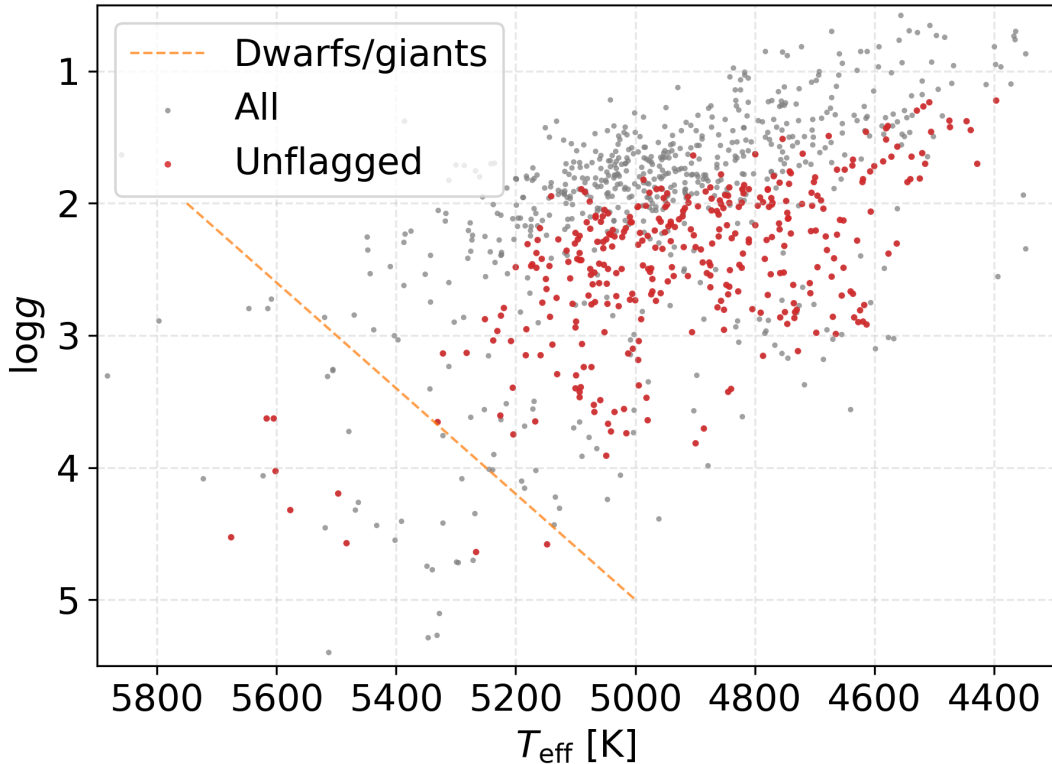


Figure 5.6: Kiel diagram for a subset of 338 detected carbon-enhanced stars with valid stellar parameters in red. Uncertain positions of flagged stars are shown with grey dots. Dashed orange line illustrates the border between giants and dwarfs.

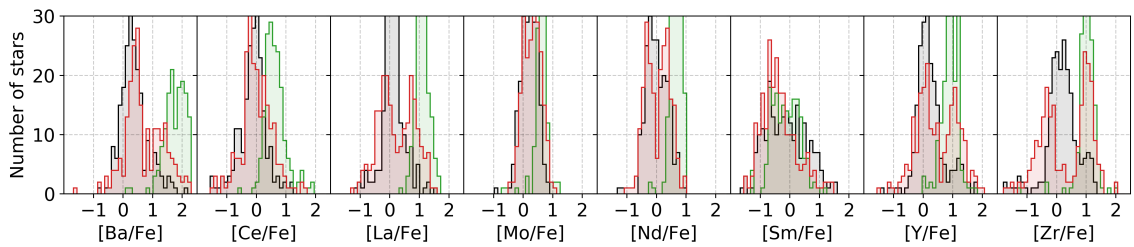


Figure 5.7: Distribution of s-process element abundances for stars in three different groups. The most enhanced group in green represent carbon-enhanced stars located in the t-SNE selected clump of stars. The red distribution presents all other detections that are placed around the projection, and outside the clump. As a control group, the same distribution in black is shown for their closest t-SNE neighbours, therefore the black and red distribution contain an equal number of objects. No abundance quality flags were used to limit abundance measurements.

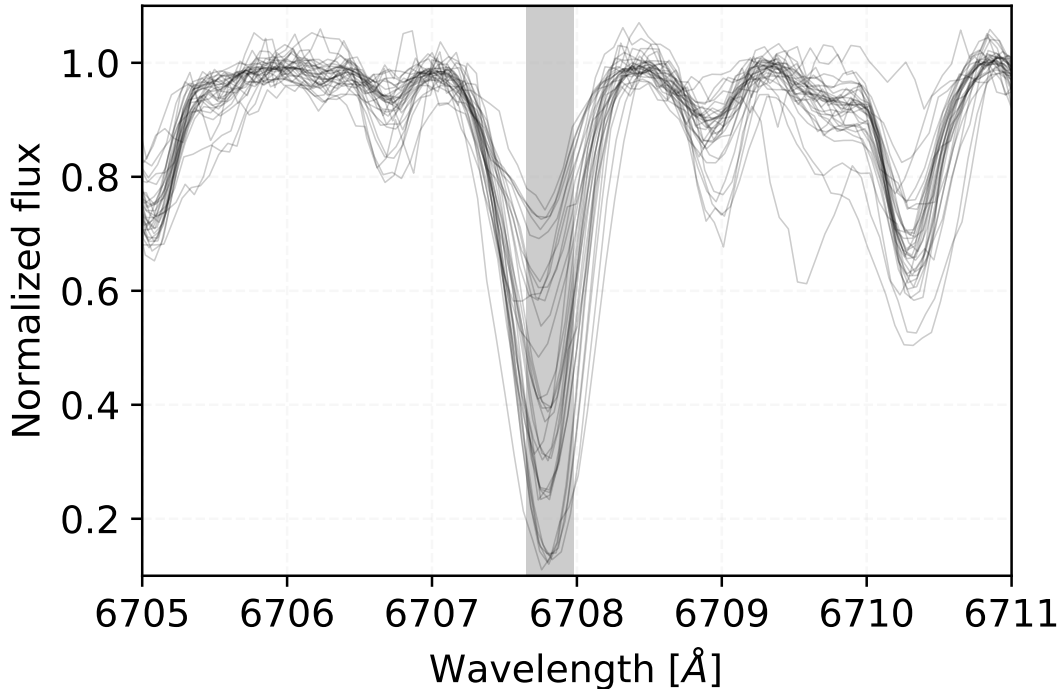


Figure 5.8: Spectral subset of 32 lithium-rich carbon-enhanced stars among the identified stars. The highlighted wavelength region is used by *The Cannon* to determine the lithium abundance of a star.

in Figure 5.7 and strength of spectral features corresponding to the same elements in Figure 5.20 hints to an enhancement of s-process elements among stars inside the selected clump. This additional enhancement might be another reason, besides the carbon enhancement, for the algorithm to cluster all of those stars as being different from the majority of spectra.

#### 5.5.4 Lithium abundance

The derivation of elemental abundances for known carbon-enhanced stars has shown that some of them can exhibit strongly enhanced levels of Li in their atmosphere [163]. Lithium is thought to be produced by hot-bottom burning [164] and brought to the surface from the stellar interior. Investigation of the Li line at 6707 Å revealed 32 of such stars. Their spectra, centred around the Li feature, show a greatly varying degree of absorption in Figure 5.8.

#### 5.5.5 Sub-classes

Following a revision of the original MK classification [165] introduced by Barnbaum *et al.* [166], carbon stars are separated into five different classes named C-H, C-R, C-J, C-N, and Barium stars. Of all the spectral indices proposed for the spectral classification, we are only able to measure a small part of Swan C<sub>2</sub> bands and Ba II line at 6496 Å. For a more detailed classification of detected objects into

proposed classes, we would need to carry out additional observations with a different spectroscopic setup to cover all the significant features.

Additionally, the features caused by the  $^{13}\text{C}^{12}\text{C}$  molecule are strongly enhanced only for a handful of spectra in our data set, therefore we did not perform any isotopic ratio analysis or identification of possible C-J objects, which are characterised by strong Swan bands produced by the heavier isotopes.

According to the abundance trends presented in Section 5.5.3 and the classification criteria defined by Barnbaum *et al.* [166], we could argue that the stars selected from the t-SNE projection belong to the C-N sub-class. Their s-process elements are clearly enhanced over Solar values (Figure 5.7), but the actual values should be treated with care as they are mostly flagged by *The Cannon*. This uncertainty might come from the fact that the training set does not cover carbon-enhanced stars and/or stars with such enhancement of s-process elements.

### 5.5.6 Match with other catalogues

In the literature we can find numerous published catalogues of carbon-enhanced (CH) stars [108, 111, 167] and CEMP stars [135, 168, 169, 170, 171, 172] observed by different telescopes and analysed in inhomogeneous ways. Most of those analyses were also performed on spectra of lower resolving power than the HERMES, therefore some visual differences are expected for wide molecular bands. By matching published catalogues with the GALAH observations that were analysed by our procedures, we identified 44 stars that matched with at least one of the catalogues. Of these, 28 were found in CH catalogues and 16 in CEMP catalogues.

From the stars recognised as CEMPs in the literature, we were able to recover only 1 of them. Visual assessment of the diagnostic plots provided by our analysis pipeline proved that the remaining 15 CEMP matches do not express any observable carbon enhancement in Swan bands and were therefore impossible to detect with the combination of our algorithms. The reason for this difference between our and literature results might be in the CEMP selection procedure employed by the aforementioned literature. Every considered study selects their set of interesting stars from one or multiple literature sources based on values of [M/H] and [C/Fe] that were measured from the atomic spectral lines and not molecular lines.

The match is larger in the case of CH matches, where we were able to confirm 11 out of 33 possible matched carbon-enhanced stars. As the observed molecular bands are prominent features in the spectra, we explored possible reasons for our low detection rate. Visual inspection of spectra for the remaining undetected matched stars proved that they also show no or barely noticeable carbon enhancement in the spectral region of Swan bands, therefore reason must lie in the detection procedures used in the cited literature. Christlieb *et al.* [108] used low-resolution spectra to evaluate enhancement of  $\text{C}_2$  and CN bands. The results are also summarised in their electronic table. In here, all of our undetected stars are marked to contain enhanced CN bands but no  $\text{C}_2$  bands. Combining this with Figure 5.9 we speculate that those stars occupy a narrow range of parameter space where  $\text{C}_2$  is not expressed and therefore undetectable in the HERMES spectra.

Number of successfully detected stars matched between the surveys could also be influenced by different excitation temperatures of analysed carbon-rich molecules. Frequently studied photometric G-band, that is not present in our spectra, covers

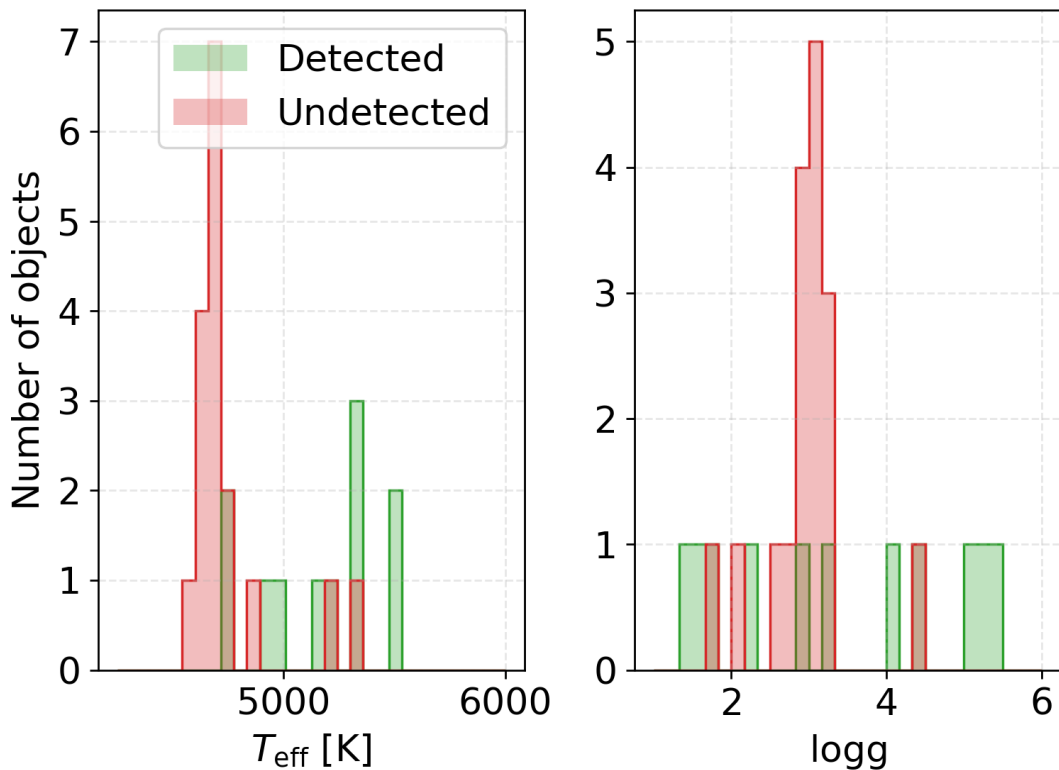


Figure 5.9: Comparison between the stellar parameters of detected (green histogram) and undetected (red histogram) carbon-enhanced stars found in literature.

a spectral region rich in CH molecule features whose temperature dependence is different than for a C<sub>2</sub> molecule. Presence of those bands is identified by classifying a carbon-enhanced star into C-H sub-class (see Section 5.5.5). As we detected all C-H stars identified by Ji *et al.* [111], that are also present in the GALAH data set, we are unable to discuss about the selection effect in the  $T_{\text{eff}}$  range between  $\sim 5100$  and  $\sim 5300$  K where those three stars were found.

The position of all stars matched with the literature is also visualised on the t-SNE projection in Figure 5.15, where it can be clearly seen that they lie outside the selected clump with identified carbon enhancement and are strewn across the projection. Close inspection of spectra that are spatially near the aggregation of CEMP stars from the literature, revealed no visible carbon enhancement. The enhancement is present neither in form of molecular bands nor expressed as stronger atomic carbon line. They therefore are indistinguishable from other metal-poor stars with similar physical parameters.

## 5.6 Metal-poor candidates

CEMP stars are defined in the literature as having low metallicity  $[\text{M}/\text{H}] < -1$  and strong carbon enrichment  $[\text{C}/\text{Fe}] > +1$ . In the scope of this analysis, we assume that our measurement of  $[\text{Fe}/\text{H}]$  is a good approximation for the metallicity. To be sure about this we compared  $[\text{M}/\text{H}]$  values of CEMP stars found in the literature and

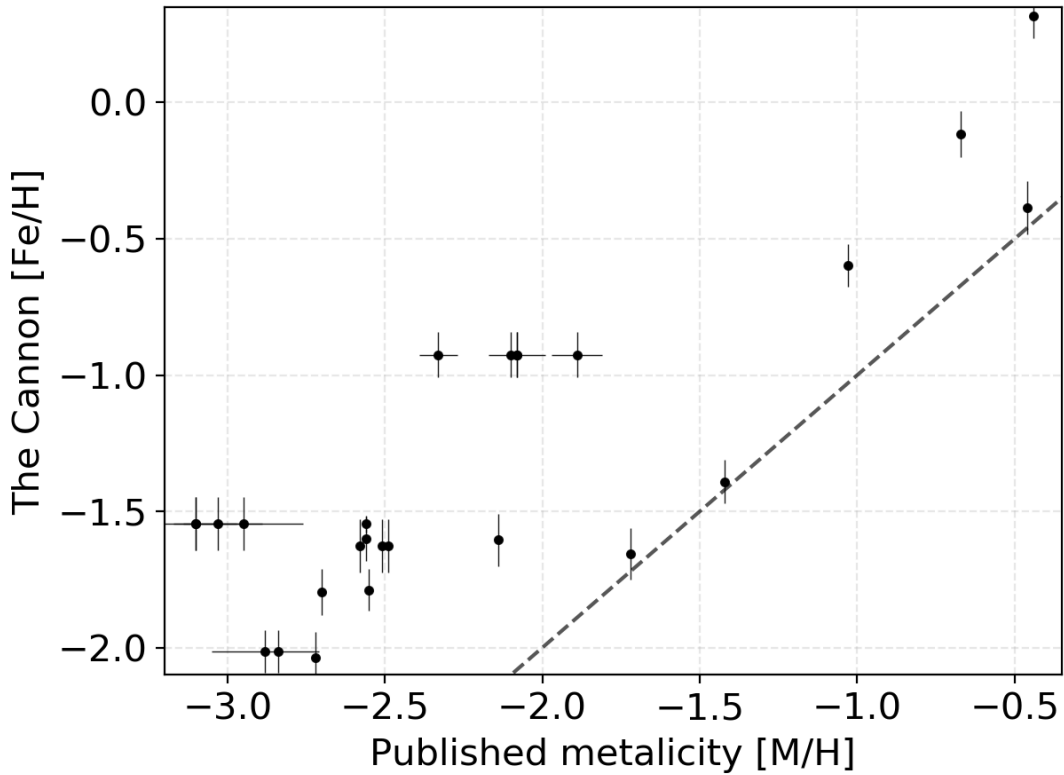


Figure 5.10: Correlation between published metallicities and *The Cannon* iron abundance for the stars that were classified as CEMPs in the literature. As some of those stars were taken from multiple literature sources, we also have multiple determinations of  $[M/H]$  for them. This can be identified as horizontal clusters of dots at different  $[M/H]$ , but with the same  $[Fe/H]$ . Where available, uncertainties of parameters are shown. The dashed line follows a 1:1 relation.

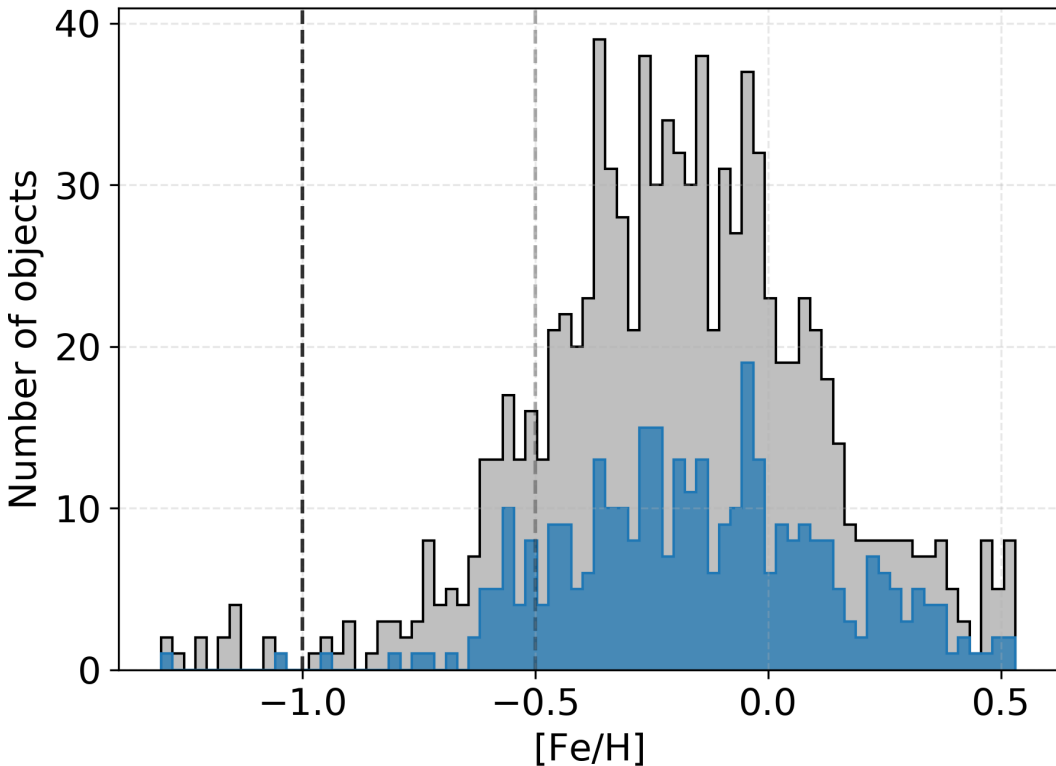


Figure 5.11: Histogram of  $[{\rm Fe}/{\rm H}]$  for detected carbon-enhanced stars with valid *The Cannon* stellar parameters in blue and for every detected carbon-enhanced star in grey. Two vertical lines are located at iron abundances of  $-1.0$  and  $-0.5$ .

$[{\rm Fe}/{\rm H}]$  derived by *The Cannon* for the same stars. The relation between them is shown in Figure 5.10. We see that our values start deviating from the published values at metallicities below  $-1.5$ . Below that threshold the differences are in the range of  $\sim 1$  dex, but the same trend is obvious for both data sets. The uncertainty of the published  $[{\rm M}/{\rm H}]$ , derived from multiple sources, can reach up to 0.5.

Taking unflagged *The Cannon* parameters and abundances of the detected objects we can determine possible CEMP candidates among our sample. As also shown by Figure 5.11 our set of carbon-enhanced stars consists of 41 objects with  $[{\rm Fe}/{\rm H}] < -0.5$  and 2 objects with  $[{\rm Fe}/{\rm H}] < -1.0$ . If we also include potentially incorrect parameters, the number of objects with  $[{\rm Fe}/{\rm H}] < -1.0$  increases to 28, which is equal to 2.8 % of detected carbon-enhanced spectra. In any case, none of them has a valid determination of carbon abundance. Analysing HERMES spectra in order to determine carbon abundance is difficult because the automatic analysis is based on only one very weak atomic absorption line that is believed to be free of any blended lines. Consequently, we are also not able to measure the  $[{\rm C}/{{\rm O}}]$  abundance ratio, as a majority of determined  $[{\rm C}/{{\rm Fe}}]$  abundances is flagged as unreliable. Complementary observations are needed to determine the abundance and confirm suggested CEMP candidates.

A low number of metal-poor candidates could also be explained by the specification of the HERMES spectrograph as its spectral bands were not selected in a way to search for and confirm most metal-poor stars. With the release of *Gaia* DR2 data

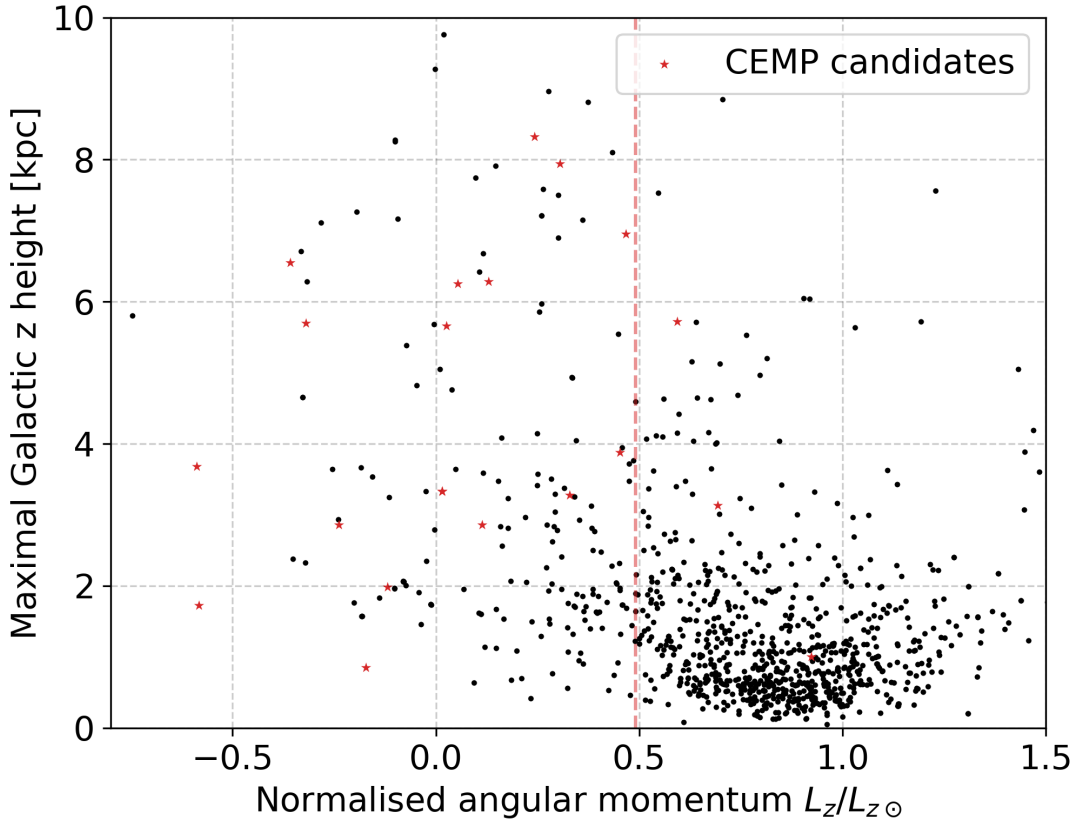


Figure 5.12: Distributions of maximal height above/below the Galactic plane reached by detected stars on their orbit around the centre of the Galaxy in comparison to their normalised angular momentum  $L_z$ . Vertical dashed line at  $1000 \text{ km s}^{-1} \text{ kpc}$  highlights the transition from the halo to the disk population, where a majority of the halo stars is located below this threshold [the threshold was visually estimated from similar plots in 175]. CEMP candidates are marked with star symbols.

[173], stars low/high-metallicity could also be compared with their Galactic orbits. To determine the distribution of detected stars among different Galactic components, we performed an orbital integration in `MWPotential2014` Galactic potential using the `galpy` package [174]. In order to construct a complete 6D kinematics information, *Gaia* parallax and proper motion measurements were supplemented with the GALAH radial velocities. Results shown in Figure 5.12 suggest that our CEMP candidates could belong to two different components of the Galaxy. Stars with maximal  $z < 4 \text{ kpc}$  most probably belong to the thick disk and stars with  $z > 5 \text{ kpc}$  to the halo population that is inherently metal-poor. This is also supported by their angular momentum in the same plot and their Galactic velocities shown in Figure 5.21.

When looking at the distribution of  $[\text{Fe}/\text{H}]$  for the complete set of observed stars, we find a comparable distribution as for carbon-enhanced stars. Similarly, about 1.8 % of stars are found to be metal-poor with  $[\text{Fe}/\text{H}] < -1.0$ .

## 5.7 Follow-up observation

To further classify and analyse one of the detected objects, a star with 2MASS identifier J11333341-0043060 was selected for a follow-up observation. We acquired its high-resolution Echelle spectrum (with the resolving power  $R \sim 20,000$ ), using a spectrograph mounted on the 1.82 m Copernico telescope located at Cima Ekar (Asiago, Italy). Because only a few of our detected candidates are observable from the Asiago observatory, we selected the best observable CEMP candidate, whose  $[\text{Fe}/\text{H}]$  was determined by *The Cannon* to be  $-0.96$ . The selected star, with  $V = 12.79$ , was on the dark limit of the used telescope, therefore low SNR was expected. The one-hour long exposure of the selected object was fully reduced, normalised order by order, and shifted to the rest frame.

Although the acquired spectrum covers a much wider and continuous spectral range (from 3900 to 7200 Å) than the HERMES spectra, only subsets, relevant for the classification of carbon-enhanced stars are presented in Figure 5.13. They were identified by visually matching our observed spectrum with the published moderate-resolution spectral atlas [166] of peculiar carbon stars. Where available, the GALAH spectrum is shown alongside the Asiago spectrum. Carbon enhancement is not expected to vary over a period of several years, therefore both spectra should show similar features. The second and fourth panel in Figure 5.13 confirm that both observations indicate a similar degree of carbon enhancement.

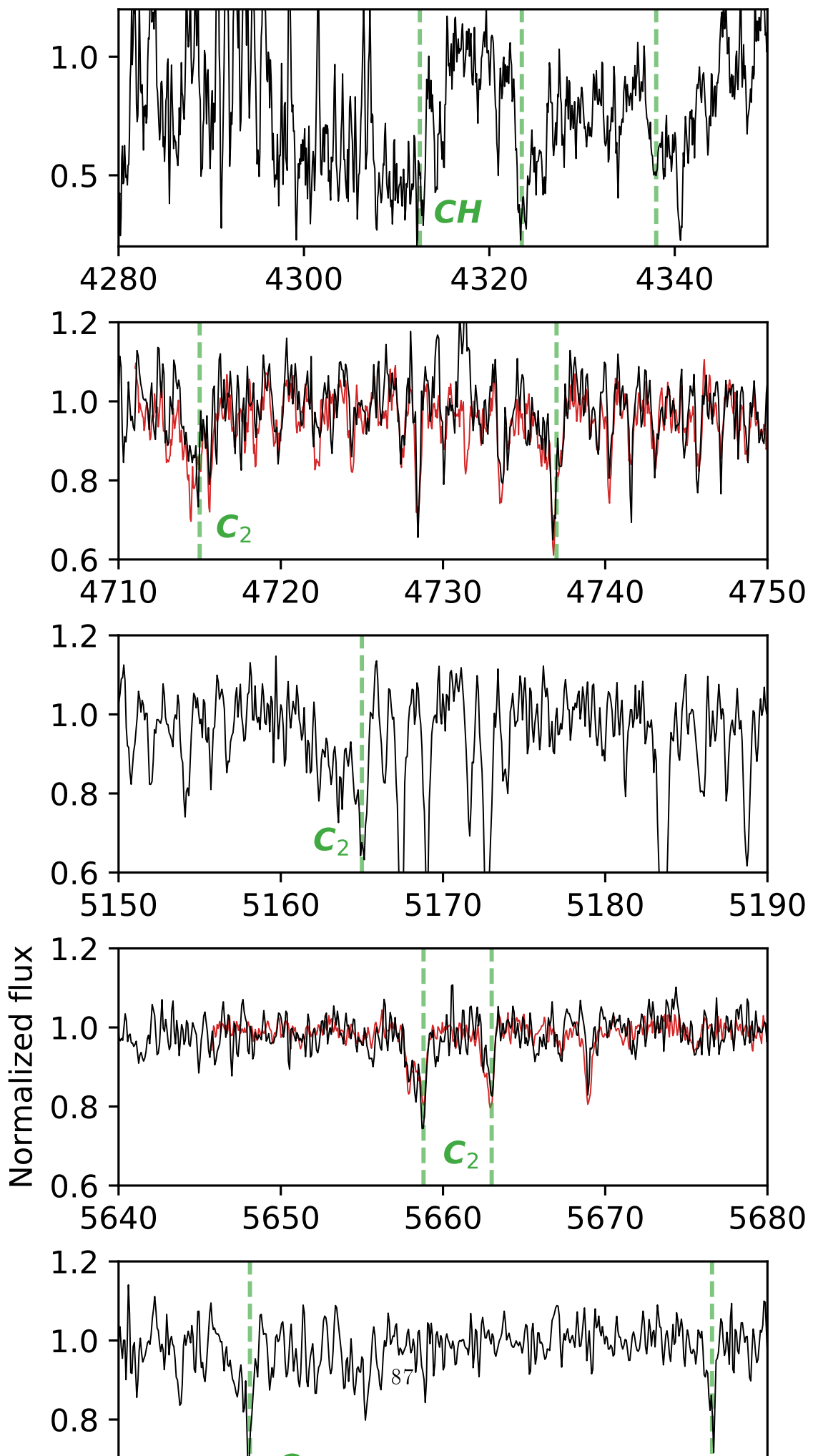
Following the classification criteria of carbon stars, we determined that the star belongs to the C-H sub-class. The definitive features for this class are strong molecular CH bands, prominent secondary P-branch head near 4342 Å (top panel in Figure 5.13), and noticeable Ba II lines at 4554 and 6496 Å [112], which are all present in the spectrum. The star definitely does not have a high ratio between  $^{13}\text{C}$  and  $^{12}\text{C}$  isotopes as the Swan features corresponding to  $^{13}\text{C}$  are clearly not present, therefore it can not be of a C-J sub-class.

Following the current state of knowledge [152, 176, 177] that most, if not all, C-H stars show clear evidence for binarity, we compared the radial velocity between both observations. They hint at the variability of the object as the follow-up radial velocity ( $126.75 \pm 1.63 \text{ km s}^{-1}$ ) deviates by more than  $3 \text{ km s}^{-1}$  from the velocity ( $123.43 \pm 0.08 \text{ km s}^{-1}$ ) observed as part of the GALAH survey. The time span between the two observations is more than 2.5 years, where the exact JD of the observation is 2458090.702 for the Asiago spectrum, and 2457122.095 for the GALAH spectrum. Further observations along the variability period would be needed to confirm whether it is a multiple stellar system.

## 5.8 Conclusions

This work explores stellar spectra acquired by the HERMES spectrograph in order to discover peculiar carbon-enhanced stars, which were observed in the scope of multiple observing programmes conducted with the same spectrograph.

We show that the spectra of such stars are sufficiently different from other stellar types to be recognisable in high-resolution spectra with limited wavelength ranges. This can be done using a supervised procedure, where some knowledge about the effects of carbon enhancement on the observed spectra is put into the algorithm, or using an unsupervised method. The latter was used to identify observed stars solely



on the basis of acquired spectra. By combining both methodologies we identified 918 unique stars with evident signs of carbon enhancement of which 12 were already reported in the literature. Out of all matched objects from the literature, we were unable to detect and confirm 16 (57 %) CH and 15 (93 %) CEMP stars with our procedures. As some of those objects were proven to contain carbon enhancement detectable outside the HERMES wavelength ranges, this would have to be taken into account to say more about the underlying population of carbon-enhanced stars. In addition to a detection bias imposed by the analysis of C<sub>2</sub> bands and exclusion of CN, and CH molecular bands that might be excited in different temperature ranges, varying degree of carbon-enhancement also has to be accounted for accurate population studies. As shown by Yoon *et al.* [98], CEMP stars can be found within a wide range of absolute carbon abundances. When an object selection is performed with a pre-defined threshold, as in the case of our supervised methodology, this may reduce the number of objects in only one of the sub-classes. In the case of CEMP stars, this selection may influence a number CEMP-no stars that are known to have lower absolute carbon abundance [98].

The identified objects were separated into dwarf and giant populations using their stellar atmospheric parameters that were also used to select possible CEMP candidates. All of the detections, with multiple observations at different epochs, were investigated for signs of variability. More than half of the repeats show signs of variability in their measured radial velocities. This could be an indicator that we are looking at a pulsating object or a multiple stellar system.

With a follow-up observation of one of the identified stars, we were able to confirm the existence of carbon-rich molecules in its atmosphere in a wider wavelength range. The acquired spectrum was also used to determine its sub-class. Variation in radial velocity points to a possible variable nature of the star or binarity that is common for C-H stars.

Follow-up observations are required to confirm variability of radial velocities observed for some of the detected carbon-enhanced stars and further investigate their nature. Careful spectral analysis, with the inclusion of carbon enhancement in models, is needed to confirm the metallicity levels of the metal-poor candidates.

The list of detected stars presented in this paper is accessible as electronic table through the CDS. Detailed structure is presented in Table 5.1. The list also includes stars from the literature, matched with our observations, for which we were unable to confirm their carbon enhancement. The list could be used to plan further observations, allowing a better understanding of these objects.

## 5.9 Table description

In the Table 5.1 we provide a list of metadata available for every object detected using the methodology described in this paper. The complete table of detected objects and its metadata is available only in electronic form at the CDS.

Table 5.1: List and description of the fields in the published catalogue of detected objects and objects matched with multiple literature sources.

Field	Unit	Description
<code>source_id</code>		<i>Gaia</i> DR2 source identifier
<code>sobject_id</code>		Unique internal per-observation star ID
<code>ra</code>	deg	Right ascension from 2MASS, J2000
<code>dec</code>	deg	Declination from 2MASS, J2000
<code>det_sup</code>	bool	Detected by supervised fitting method
<code>det_usup</code>	bool	Detected by t-SNE method
<code>swan_integ</code>		Swan band strength if determined
<code>teff</code>	K	<i>The Cannon</i> effective temperature $T_{\text{eff}}$
<code>e_teff</code>	K	Uncertainty of determined $T_{\text{eff}}$
<code>logg</code>		<i>The Cannon</i> surface gravity $\log g$
<code>e_logg</code>		Uncertainty of determined $\log g$
<code>feh</code>		<i>The Cannon</i> iron abundance [Fe/H]
<code>e_feh</code>		Uncertainty of determined [Fe/H]
<code>flag_cannon</code>	int	<i>The Cannon</i> flags in a bit mask format
<code>type</code>		G for giants and D for dwarfs
<code>rv_var</code>	bool	Is radial velocity variable
<code>li_strong</code>	bool	Shows strong lithium absorption
<code>cemp_cand</code>	bool	Is star CEMP candidate
<code>bib_code</code>		ADS bibcode of the literature match

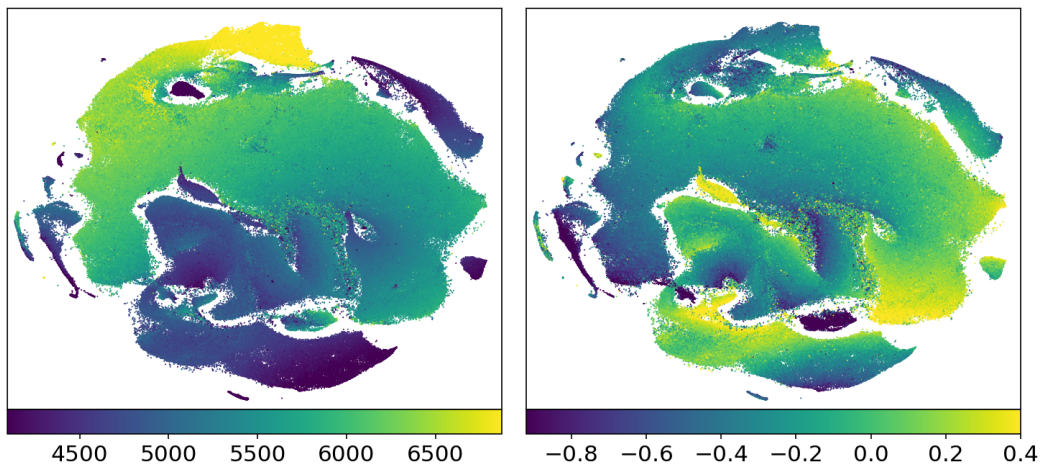


Figure 5.14: Spatial distribution of all available measurements of  $T_{\text{eff}}$  (left panel) and [Fe/H] (right panel) as determined by *The Cannon*. Dots, representing analysed spectra in the t-SNE projection, are colour coded by their parameter values. Colours and their corresponding values are explained by a colourbar under the graph.

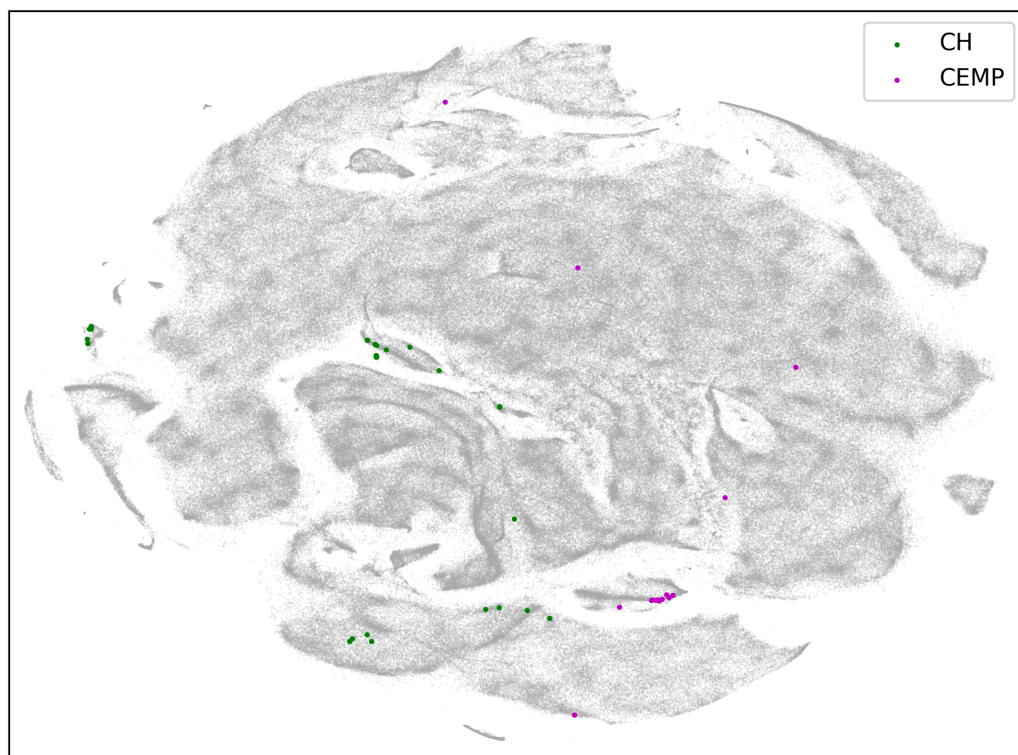


Figure 5.15: t-SNE projection with marked known carbon-enhanced and CEMP objects from multiple different catalogues found in the literature that are also part of our analysed set of spectra.

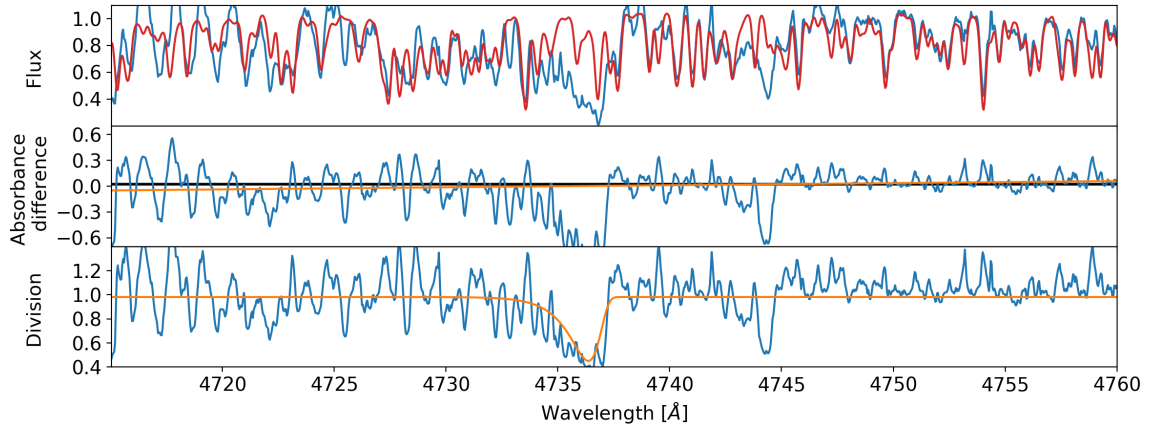


Figure 5.16: Equivalent plot as in the Figure 5.1 but presenting an example of a metal-rich star with multiple strong Swan features around 4737 and 4745 Å. Presented star has a 2MASS identifier J13121354-3533120 and is known Galactic carbon star [167].

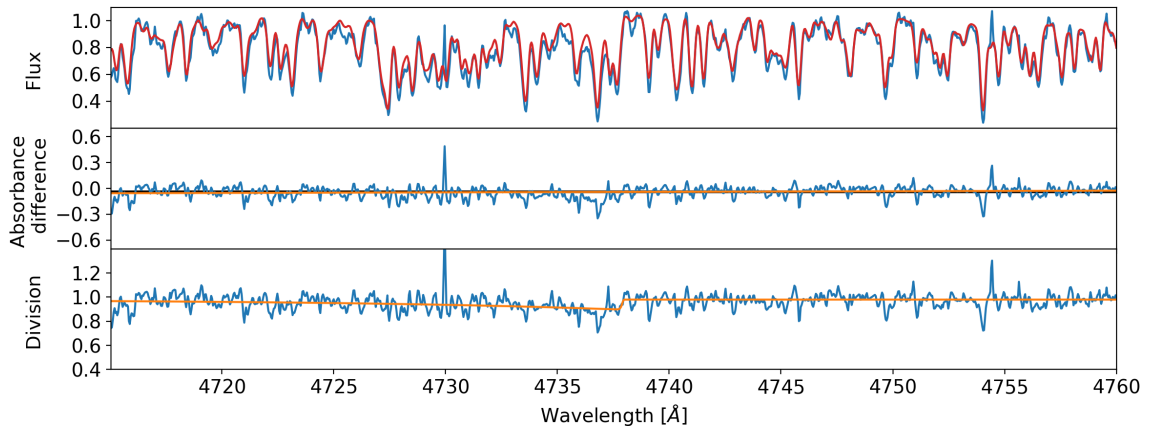


Figure 5.17: Equivalent plot as in the Figure 5.1 showing the last of 400 spectra, ordered by their degree of carbon enhancement, selected by the supervised methodology.

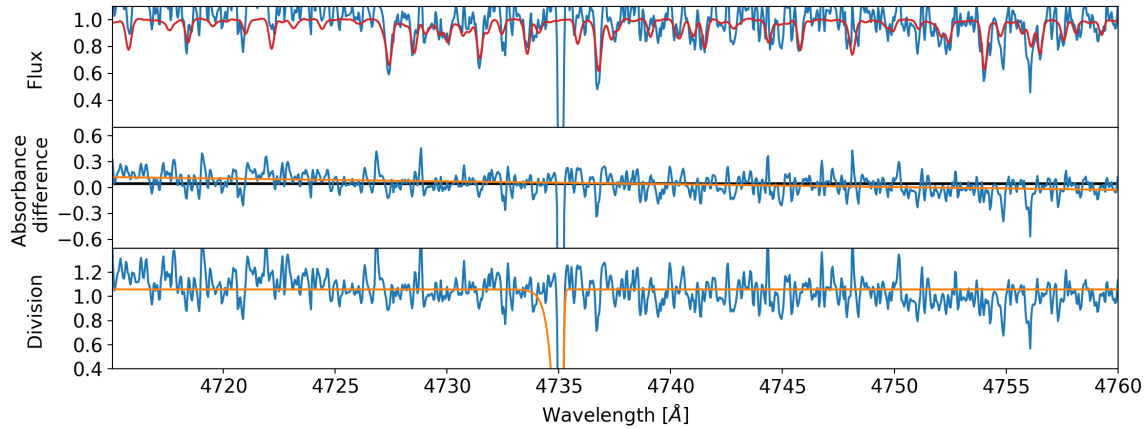


Figure 5.18: Equivalent plot as in the Figure 5.1 but representing grossly over exaggerated carbon enhancement by a fit that describes a reduction problem (a cosmic ray in a subtracted sky spectrum).

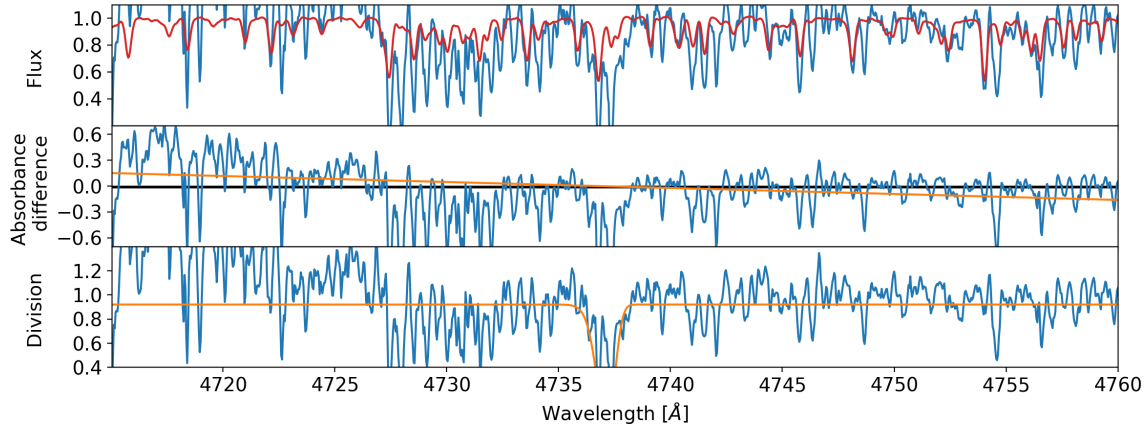


Figure 5.19: Equivalent plot as in the Figure 5.1 but representing a fit to absorption lines of a double-lined spectroscopic binary. Final fit is not skewed as would be expected in the case of carbon enhancement.

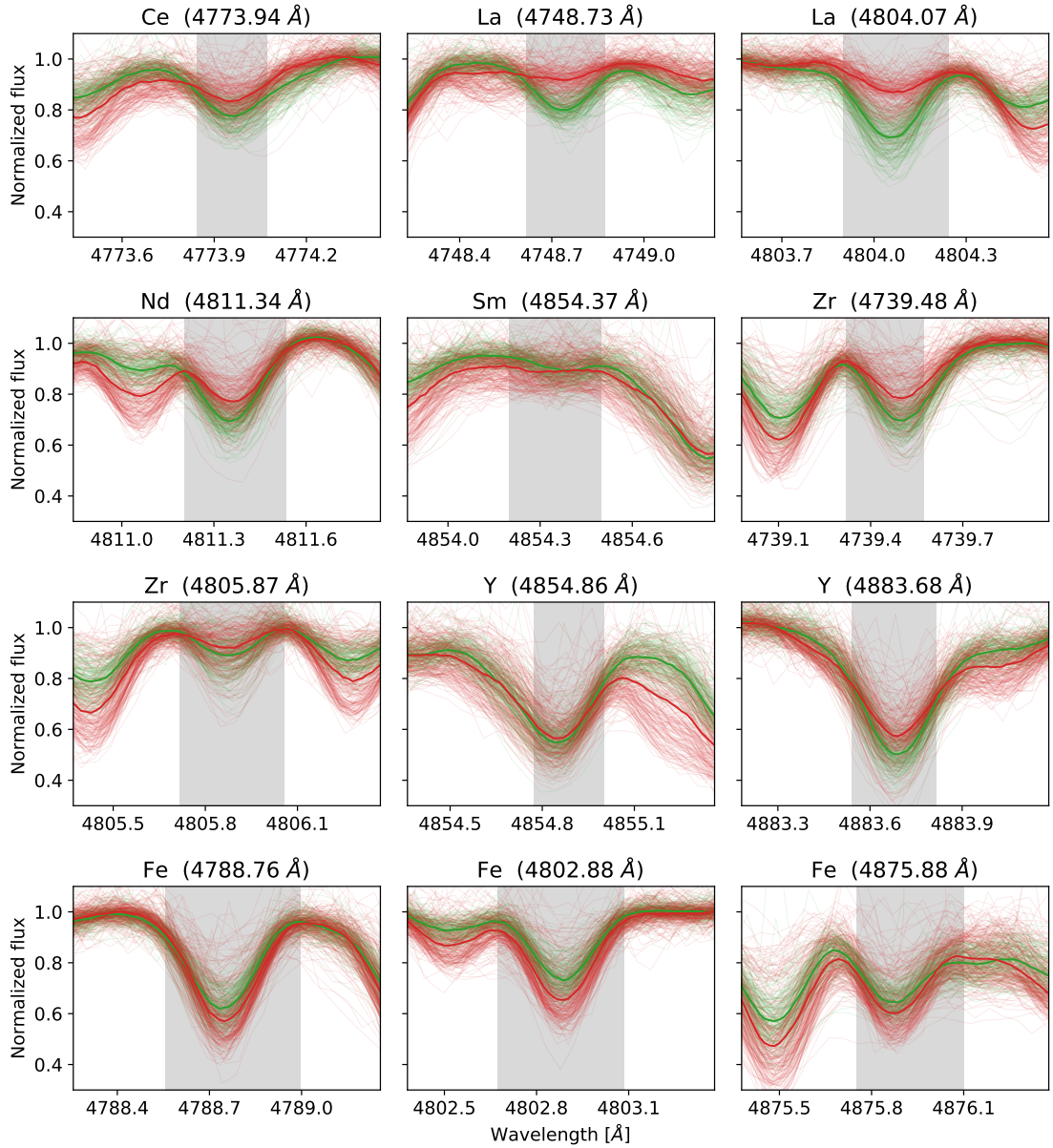


Figure 5.20: Spectral subset around the absorption features in the blue arm that were used to determine abundances of Fe and s-process elements. Same colour coding is used as in Figure 5.7. Spectra inside the t-SNE determined clump are shown in red, and outside it in green. Median of all spectra is shown with a bold line of the same colour. The shaded area gives the wavelength range considered in the computation of abundances.

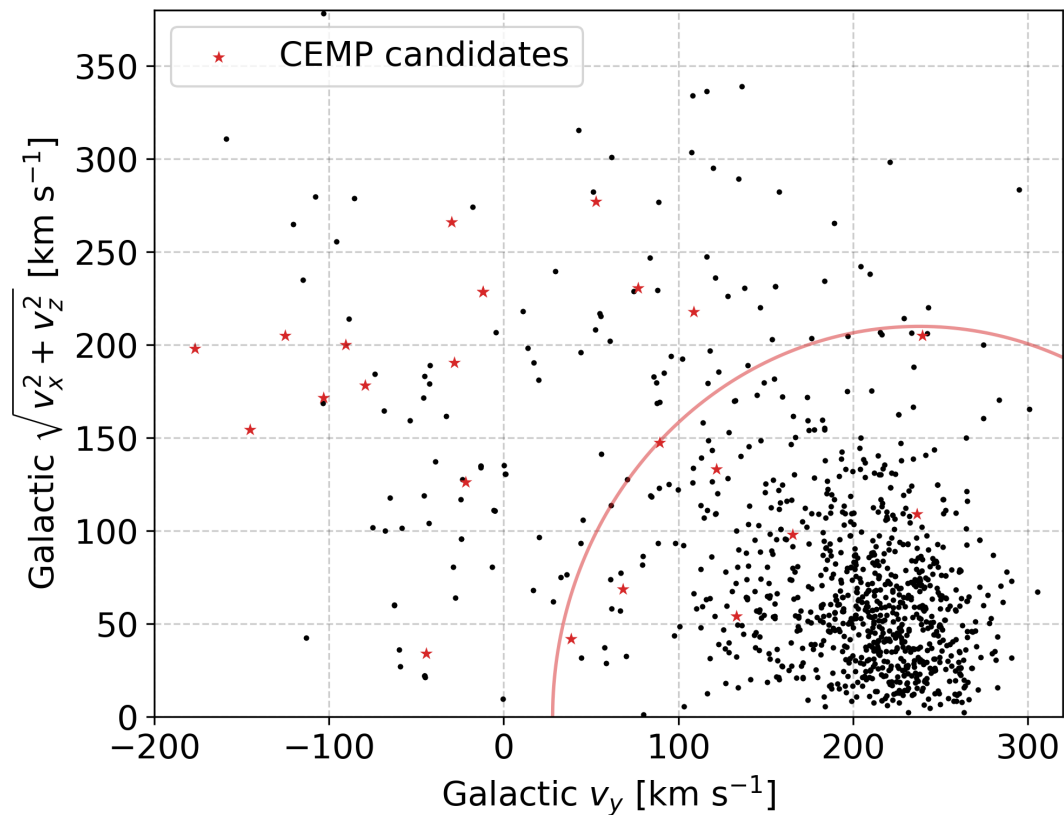


Figure 5.21: Toomre diagram used to identify possible local halo stars among our detected carbon-enhanced stars, especially CEMP candidates. Halo stars in this diagram are located above the red circular line, satisfying the velocity condition  $|\mathbf{v} - \mathbf{v}_{\text{LSR}}| > 210 \text{ km s}^{-1}$  [the threshold taken from 175]. CEMP candidates are marked with star symbols.

# Chapter 6

## Conclusions



# Bibliography

- [1] Gaia Collaboration, T. Prusti, J. H. J. de Bruijne, A. G. A. Brown, A. Vallenari, C. Babusiaux, C. A. L. Bailer-Jones, U. Bastian, M. Biermann, D. W. Evans and et al., *The Gaia mission*, **595**, A1 (2016).
- [2] M. Cropper, D. Katz, P. Sartoretti, T. Prusti, J. H. J. de Bruijne, F. Chassat, P. Charvet, J. Boyadjian, M. Perryman, G. Sarri, P. Gare, M. Erdmann, U. Munari, T. Zwitter, M. Wilkinson, F. Arenou, A. Vallenari, A. Gómez, P. Panuzzo, G. Seabroke, C. Allende Prieto, K. Benson, O. Marchal, H. Huckle, M. Smith, C. Dolding, K. Janßen, Y. Viala, R. Blomme, S. Baker, S. Boudreault, F. Crifo, C. Soubiran, Y. Frémat, G. Jasniewicz, A. Guerrier, L. P. Guy, C. Turon, A. Jean-Antoine-Piccolo, F. Thévenin, M. David, E. Gosset and Y. Damerdji, *Gaia Data Release 2. Gaia Radial Velocity Spectrometer*, **616**, A5 (2018).
- [3] Gaia Collaboration, F. Mignard, S. A. Klioner, L. Lindegren, J. Hernández, U. Bastian, A. Bombrun, D. Hobbs, U. Lammers, D. Michalik, M. Ramos-Lerate, M. Biermann, J. Fernández-Hernández, R. Geyer, T. Hilger, H. I. Siddiqui, H. Steidelmüller, C. Babusiaux, C. Barache, S. Lambert, A. H. Andrei, G. Bourda, P. Charlot, A. G. A. Brown, A. Vallenari, T. Prusti, J. H. J. de Bruijne, C. A. L. Bailer-Jones, D. W. Evans, L. Eyer, F. Jansen, C. Jordi, X. Luri, C. Panem, D. Pourbaix, S. Randich, P. Sartoretti, C. Soubiran, F. van Leeuwen, N. A. Walton, F. Arenou, M. Cropper, R. Drimmel, D. Katz, M. G. Lattanzi, J. Bakker, C. Cacciari, J. Castañeda, L. Chaoul, N. Cheek, F. De Angeli, C. Fabricius, R. Guerra, B. Holl, E. Masana, R. Messineo, N. Mowlavi, K. Nienartowicz, P. Panuzzo, J. Portell, M. Riello, G. M. Seabroke, P. Tanga, F. Thévenin, G. Gracia-Abril, G. Comoretto, M. Garcia-Reinaldos, D. Teyssier, M. Altmann, R. Andrae, M. Audard, I. Bellas-Velidis, K. Benson, J. Berthier, R. Blomme, P. Burgess, G. Busso, B. Carry, A. Cellino, G. Clementini, M. Clotet, O. Cleevey, M. Davidson, J. De Ridder, L. Delchambre, A. Dell’Oro, C. Ducourant, M. Fouesneau, Y. Frémat, L. Galluccio, M. García-Torres, J. González-Núñez, J. J. González-Vidal, E. Gosset, L. P. Guy, J. L. Halbwachs, N. C. Hambly, D. L. Harrison, D. Hestroffer, S. T. Hodgkin, A. Hutton, G. Jasniewicz, A. Jean-Antoine-Piccolo, S. Jordan, A. J. Korn, A. Krone-Martins, A. C. Lanzafame, T. Lebzelter, W. Löffler, M. Manteiga, P. M. Marrese, J. M. Martín-Fleitas, A. Moitinho, A. Mora, K. Muinonen, J. Osinde, E. Pancino, T. Pauwels, J. M. Petit, A. Recio-Blanco, P. J. Richards, L. Rimoldini, A. C. Robin, L. M. Sarro, C. Siopis, M. Smith, A. Sozzetti, M. Süveges, J. Torra, W. van Reeven, U. Abbas, A. Abreu Aramburu, S. Accart, C. Aerts, G. Altavilla, M. A. Álvarez, R. Alvarez, J. Alves, R. I. Anderson, E. Anglada Varela, E. Antiche, T. Antoja, B. Arcay, T. L.

## Bibliography

---

Astraatmadja, N. Bach, S. G. Baker, L. Balaguer-Núñez, P. Balm, C. Barata, D. Barbato, F. Barblan, P. S. Barklem, D. Barrado, M. Barros, M. A. Barstow, L. Bartholomé Muñoz, J. L. Bassilana, U. Becciani, M. Bellazzini, A. Berihuete, S. Bertone, L. Bianchi, O. Bienaymé, S. Blanco-Cuaresma, T. Boch, C. Boeche, R. Borrachero, D. Bossini, S. Bouquillon, A. Bragaglia, L. Bramante, M. A. Breddels, A. Bressan, N. Brouillet, T. Brüsemeister, E. Brugaletta, B. Bucciarelli, A. Burlacu, D. Busonero, A. G. Butkevich, R. Buzzi, E. Caffau, R. Cancellerie, G. Cannizzaro, T. Cantat-Gaudin, R. Carballo, T. Carlucci, J. M. Carrasco, L. Casamiquela, M. Castellani, A. Castro-Ginard, L. Chemin, A. Chiavassa, G. Cocozza, G. Costigan, S. Cowell, F. Crifo, M. Crosta, C. Crowley, J. Cuypers, C. Dafonte, Y. Damerdji, A. Dapergolas, P. David, M. David, P. de Laverny, F. De Luise, R. De March, R. de Souza, A. de Torres, J. Debosscher, E. del Pozo, M. Delbo, A. Delgado, H. E. Delgado, S. Diakite, C. Diener, E. Distefano, C. Dolding, P. Drazinos, J. Durán, B. Edvardsson, H. Enke, K. Eriksson, P. Esquej, G. Eynard Bon-temps, C. Fabre, M. Fabrizio, S. Faigler, A. J. Falcão, M. Farràs Casas, L. Federici, G. Fedorets, P. Fernique, F. Figueras, F. Filippi, K. Findeisen, A. Fonti, E. Fraile, M. Fraser, B. Frézouls, M. Gai, S. Galleti, D. Garabato, F. García-Sedano, A. Garofalo, N. Garralda, A. Gavel, P. Gavras, J. Gerssen, P. Giacobbe, G. Gilmore, S. Girona, G. Giuffrida, F. Glass, M. Gomes, M. Granvik, A. Gueguen, A. Guerrier, J. Guiraud, R. Gutié, R. Haigron, D. Hatzidimitriou, M. Hauser, M. Haywood, U. Heiter, A. Helmi, J. Heu, W. Hofmann, G. Holland, H. E. Huckle, A. Hypki, V. Icardi, K. Janßen, G. Jevardat de Fombelle, P. G. Jonker, A. L. Juhász, F. Julbe, A. Karampelas, A. Kewley, J. Klar, A. Kochoska, R. Kohley, K. Kolenberg, M. Kontizas, E. Kontizas, S. E. Koposov, G. Kordopatis, Z. Kostrzewska-Rutkowska, P. Koubsky, A. F. Lanza, Y. Lasne, J. B. Lavigne, Y. Le Fustec, C. Le Poncin-Lafitte, Y. Lebreton, S. Leccia, N. Leclerc, I. Lecoer-Taibi, H. Lenhardt, F. Leroux, S. Liao, E. Licata, H. E. P. Lindstrøm, T. A. Lister, E. Livanou, A. Lobel, M. López, S. Managau, R. G. Mann, G. Mantelet, O. Marchal, J. M. Marchant, M. Marconi, S. Marinoni, G. Marschalkó, D. J. Marshall, M. Martino, G. Marton, N. Mary, D. Massari, G. Matijević, T. Mazeh, P. J. McMillan, S. Messina, N. R. Millar, D. Molina, R. Molinaro, L. Molnár, P. Montegriffo, R. Mor, R. Morbidelli, T. Morel, D. Morris, A. F. Mulone, T. Muraveva, I. Musella, G. Nelemans, L. Nicastro, L. Noval, W. O'Mullane, C. Ordénovic, D. Ordóñez-Blanco, P. Osborne, C. Pagani, I. Pagano, F. Pailler, H. Palacin, L. Palaversa, A. Panahi, M. Pawlak, A. M. Piersimoni, F. X. Pineau, E. Plachy, G. Plum, E. Poggio, E. Poujoulet, A. Prša, L. Pulone, E. Racero, S. Ragaini, N. Rambaux, S. Regibo, C. Reylé, F. Riclet, V. Ripepi, A. Riva, A. Rivard, G. Rixon, T. Roegiers, M. Roelens, M. Romero-Gómez, N. Rowell, F. Royer, L. Ruiz-Dern, G. Sadowski, T. Sagristà Sellés, J. Sahlmann, J. Salgado, E. Salguero, N. Sanna, T. Santana-Ros, M. Sarasso, H. Savietto, M. Schultheis, E. Sciacca, M. Segol, J. C. Segovia, D. Ségransan, I. C. Shih, L. Siltala, A. F. Silva, R. L. Smart, K. W. Smith, E. Solano, F. Solitro, R. Sordo, S. Soria Nieto, J. Souchay, A. Spagna, F. Spoto, U. Stampa, I. A. Steele, C. A. Stephenson, H. Stoev, F. F. Suess, J. Surdej, L. Szabados, E. Szegedi-Elek, D. Tapiador, F. Taris, G. Tauran, M. B. Taylor, R. Teixeira, D. Terrett, P. Teyssandier, W. Thuillot, A. Titarenko, F. Torra Clotet, C. Turon, A. Ulla, E. Utrilla,

- S. Uzzi, M. Vaillant, G. Valentini, V. Valette, A. van Elteren, E. Van Hemelryck, M. van Leeuwen, M. Vaschetto, A. Vecchiato, J. Veljanoski, Y. Viala, D. Vicente, S. Vogt, C. von Essen, H. Voss, V. Votruba, S. Voutsinas, G. Walm-sley, M. Weiler, O. Wertz, T. Wevers, Ł. Wyrzykowski, A. Yoldas, M. Źerjal, H. Ziaeepour, J. Zorec, S. Zschocke, S. Zucker, C. Zurbach and T. Zwitter, *Gaia Data Release 2. The celestial reference frame (Gaia-CRF2)*, **616**, A14 (2018).
- [4] L. Lindegren, "Re-normalising the astrometric chi-square in Gaia DR2", *Gaia Technical Note: GAIA-C3-TN-LU-LL-124-0* (2018).
- [5] L. Lindegren, J. Hernández, A. Bombrun, S. Klioner, U. Bastian, M. Ramos-Lerate, A. de Torres, H. Steidelmüller, C. Stephenson, D. Hobbs, U. Lammers, M. Biermann, R. Geyer, T. Hilger, D. Michalik, U. Stampa, P. J. McMillan, J. Castañeda, M. Clotet, G. Comoretto, M. Davidson, C. Fabricius, G. Gracia, N. C. Hambly, A. Hutton, A. Mora, J. Portell, F. van Leeuwen, U. Abbas, A. Abreu, M. Altmann, A. Andrei, E. Anglada, L. Balaguer-Núñez, C. Barache, U. Becciani, S. Bertone, L. Bianchi, S. Bouquillon, G. Bourda, T. Brüsemeister, B. Bucciarelli, D. Busonero, R. Buzzi, R. Cancelliere, T. Carlucci, P. Charlot, N. Cheek, M. Crosta, C. Crowley, J. de Bruijne, F. de Felice, R. Drimmel, P. Esquej, A. Fienga, E. Fraile, M. Gai, N. Garralda, J. J. González-Vidal, R. Guerra, M. Hauser, W. Hofmann, B. Holl, S. Jordan, M. G. Lattanzi, H. Lenhardt, S. Liao, E. Licata, T. Lister, W. Löffler, J. Marchant, J. M. Martin-Fleitas, R. Messineo, F. Mignard, R. Morbidelli, E. Poggio, A. Riva, N. Rowell, E. Salguero, M. Sarasso, E. Sciacca, H. Siddiqui, R. L. Smart, A. Spagna, I. Steele, F. Taris, J. Torra, A. van Elteren, W. van Reeven and A. Vecchiato, *Gaia Data Release 2. The astrometric solution*, **616**, A2 (2018).
- [6] X. Luri, A. G. A. Brown, L. M. Sarro, F. Arenou, C. A. L. Bailer-Jones, A. Castro-Ginard, J. de Bruijne, T. Prusti, C. Babusiaux and H. E. Delgado, *Gaia Data Release 2. Using Gaia parallaxes*, **616**, A9 (2018).
- [7] D. W. Evans, M. Riello, F. De Angeli, J. M. Carrasco, P. Montegriffo, C. Fabricius, C. Jordi, L. Palaversa, C. Diener, G. Busso, C. Cacciari, F. van Leeuwen, P. W. Burgess, M. Davidson, D. L. Harrison, S. T. Hodgkin, E. Pancino, P. J. Richards, G. Altavilla, L. Balaguer-Núñez, M. A. Barstow, M. Bellazzini, A. G. A. Brown, M. Castellani, G. Cocozza, F. De Luise, A. Delgado, C. Ducourant, S. Galleti, G. Gilmore, G. Giuffrida, B. Holl, A. Kewley, S. E. Koposov, S. Marinoni, P. M. Marrese, P. J. Osborne, A. Piersimoni, J. Portell, L. Pulone, S. Ragagni, N. Sanna, D. Terrett, N. A. Walton, T. Wevers and Ł. Wyrzykowski, *Gaia Data Release 2. Photometric content and validation*, **616**, A4 (2018).
- [8] M. Riello, F. De Angeli, D. W. Evans, G. Busso, N. C. Hambly, M. Davidson, P. W. Burgess, P. Montegriffo, P. J. Osborne, A. Kewley, J. M. Carrasco, C. Fabricius, C. Jordi, C. Cacciari, F. van Leeuwen and G. Holland, *Gaia Data Release 2. Processing of the photometric data*, **616**, A3 (2018).
- [9] C. Soubiran, G. Jasniewicz, L. Chemin, C. Zurbach, N. Brouillet, P. Panuzzo, P. Sartoretti, D. Katz, J. F. Le Campion, O. Marchal, D. Hestroffer,

## Bibliography

---

- F. Thévenin, F. Crifo, S. Udry, M. Cropper, G. Seabroke, Y. Viala, K. Benson, R. Blomme, A. Jean-Antoine, H. Huckle, M. Smith, S. G. Baker, Y. Damerdji, C. Dolding, Y. Frémat, E. Gosset, A. Guerrier, L. P. Guy, R. Haigron, K. Janßen, G. Plum, C. Fabre, Y. Lasne, F. Pailler, C. Panem, F. Riclet, F. Royer, G. Tauran, T. Zwitter, A. Gueguen and C. Turon, *Gaia Data Release 2. The catalogue of radial velocity standard stars*, **616**, A7 (2018).
- [10] P. Sartoretti, D. Katz, M. Cropper, P. Panuzzo, G. M. Seabroke, Y. Viala, K. Benson, R. Blomme, G. Jasniewicz, A. Jean-Antoine, H. Huckle, M. Smith, S. Baker, F. Crifo, Y. Damerdji, M. David, C. Dolding, Y. Frémat, E. Gosset, A. Guerrier, L. P. Guy, R. Haigron, K. Janßen, O. Marchal, G. Plum, C. Soubiran, F. Thévenin, M. Ajaj, C. Allende Prieto, C. Babusiaux, S. Boudreault, L. Chemin, C. Delle Luche, C. Fabre, A. Gueguen, N. C. Hambly, Y. Lasne, F. Meynadier, F. Pailler, C. Panem, F. Riclet, F. Royer, G. Tauran, C. Zurbach, T. Zwitter, F. Arenou, A. Gomez, V. Lemaitre, N. Leclerc, T. Morel, U. Munari, C. Turon and M. Žerjal, *Gaia Data Release 2. Processing the spectroscopic data*, **616**, A6 (2018).
- [11] B. Holl, M. Audard, K. Nienartowicz, G. Jevardat de Fombelle, O. Marchal, N. Mowlavi, G. Clementini, J. De Ridder, D. W. Evans, L. P. Guy, A. C. Lanzafame, T. Lebzelter, L. Rimoldini, M. Roelens, S. Zucker, E. Distefano, A. Garofalo, I. Lecoeur-Taïbi, M. Lopez, R. Molinaro, T. Muraveva, A. Panahi, S. Regibo, V. Ripepi, L. M. Sarro, C. Aerts, R. I. Anderson, J. Charnas, F. Barblan, S. Blanco-Cuaresma, G. Busso, J. Cuypers, F. De Angeli, F. Glass, M. Grenon, Á. L. Juhász, A. Kochoska, P. Koubeky, A. F. Lanza, S. Leccia, D. Lorenz, M. Marconi, G. Marschalkó, T. Mazeh, S. Messina, F. Mignard, A. Moitinho, L. Molnár, S. Morgenthaler, I. Musella, C. Ordenovic, D. Ordóñez, I. Pagano, L. Palaversa, M. Pawlak, E. Plachy, A. Prša, M. Riello, M. Süveges, L. Szabados, E. Szegedi-Elek, V. Votruba and L. Eyer, *Gaia Data Release 2. Summary of the variability processing and analysis results*, **618**, A30 (2018).
- [12] N. Mowlavi, I. Lecoeur-Taïbi, T. Lebzelter, L. Rimoldini, D. Lorenz, M. Audard, J. De Ridder, L. Eyer, L. P. Guy, B. Holl, G. Jevardat de Fombelle, O. Marchal, K. Nienartowicz, S. Regibo, M. Roelens and L. M. Sarro, *Gaia Data Release 2. The first Gaia catalogue of long-period variable candidates*, **618**, A58 (2018).
- [13] L. Molnár, E. Plachy, Á. L. Juhász and L. Rimoldini, *Gaia Data Release 2. Validating the classification of RR Lyrae and Cepheid variables with the Kepler and K2 missions*, **620**, A127 (2018).
- [14] G. Clementini, V. Ripepi, R. Molinaro, A. Garofalo, T. Muraveva, L. Rimoldini, L. P. Guy, G. Jevardat de Fombelle, K. Nienartowicz, O. Marchal, M. Audard, B. Holl, S. Leccia, M. Marconi, I. Musella, N. Mowlavi, I. Lecoeur-Taibi, L. Eyer, J. De Ridder, S. Regibo, L. M. Sarro, L. Szabados, D. W. Evans and M. Riello, *Gaia Data Release 2. Specific characterisation and validation of all-sky Cepheids and RR Lyrae stars*, **622**, A60 (2019).
- [15] R. Andrae, M. Fouesneau, O. Creevey, C. Ordenovic, N. Mary, A. Burlacu, L. Chaoul, A. Jean-Antoine-Piccolo, G. Kordopatis, A. Korn, Y. Lebreton,

- C. Panem, B. Pichon, F. Thévenin, G. Walmsley and C. A. L. Bailer-Jones, *Gaia Data Release 2. First stellar parameters from Apsis*, **616**, A8 (2018).
- [16] Gaia Collaboration, F. Spoto, P. Tanga, F. Mignard, J. Berthier, B. Carry, A. Cellino, A. Dell’Oro, D. Hestroffer, K. Muinonen, T. Pauwels, J. M. Petit, P. David, F. De Angeli, M. Delbo, B. Frézouls, L. Galluccio, M. Granvik, J. Guiraud, J. Hernández, C. Ordénovic, J. Portell, E. Poujoulet, W. Thuillot, G. Walmsley, A. G. A. Brown, A. Vallenari, T. Prusti, J. H. J. de Bruijne, C. Babusiaux, C. A. L. Bailer-Jones, M. Biermann, D. W. Evans, L. Eyer, F. Jansen, C. Jordi, S. A. Klioner, U. Lammers, L. Lindegren, X. Luri, C. Panem, D. Pourbaix, S. Randich, P. Sartoretti, H. I. Siddiqui, C. Soubiran, F. van Leeuwen, N. A. Walton, F. Arenou, U. Bastian, M. Cropper, R. Drimmel, D. Katz, M. G. Lattanzi, J. Bakker, C. Cacciari, J. Castañeda, L. Chaoul, N. Cheek, C. Fabricius, R. Guerra, B. Holl, E. Masana, R. Messineo, N. Mowlavi, K. Nienartowicz, P. Panuzzo, M. Riello, G. M. Seabroke, F. Thévenin, G. Gracia-Abril, G. Comoretto, M. Garcia-Reinaldos, D. Teyssier, M. Altmann, R. Andrae, M. Audard, I. Bellas-Velidis, K. Benson, R. Blomme, P. Burgess, G. Busso, G. Clementini, M. Clotet, O. Creevey, M. Davidson, J. De Ridder, L. Delchambre, C. Ducourant, J. Fernández-Hernández, M. Fouesneau, Y. Frémat, M. García-Torres, J. González-Núñez, J. J. González-Vidal, E. Gosset, L. P. Guy, J. L. Halbwachs, N. C. Hambly, D. L. Harrison, S. T. Hodgkin, A. Hutton, G. Jasniewicz, A. Jean-Antoine-Piccolo, S. Jordan, A. J. Korn, A. Krone-Martins, A. C. Lanzafame, T. Lebzelter, W. Lö, M. Manteiga, P. M. Marrese, J. M. Martín-Fleitas, A. Moitinho, A. Mora, J. Osinde, E. Pancino, A. Recio-Blanco, P. J. Richards, L. Rimoldini, A. C. Robin, L. M. Sarro, C. Siopis, M. Smith, A. Sozzetti, M. Süveges, J. Torra, W. van Reeven, U. Abbas, A. Abreu Aramburu, S. Accart, C. Aerts, G. Altavilla, M. A. Álvarez, R. Alvarez, J. Alves, R. I. Anderson, A. H. Andrei, E. Anglada Varela, E. Antiche, T. Antoja, B. Arcay, T. L. Astraatmadja, N. Bach, S. G. Baker, L. Balaguer-Núñez, P. Balm, C. Barache, C. Barata, D. Barbato, F. Barblan, P. S. Barklem, D. Barrado, M. Barros, M. A. Barstow, L. Bartholomé Muñoz, J. L. Bassilana, U. Becciani, M. Bellazzini, A. Berihuete, S. Bertone, L. Bianchi, O. Bienaymé, S. Blanco-Cuaresma, T. Boch, C. Boeche, A. Bombrun, R. Borrachero, D. Bossini, S. Bouquillon, G. Bourda, A. Bragaglia, L. Bramante, M. A. Breddels, A. Bressan, N. Brouillet, T. Brüsemeister, E. Brugaletta, B. Buccarelli, A. Burlacu, D. Busonero, A. G. Butkevich, R. Buzzi, E. Caffau, R. Cancelliere, G. Cannizzaro, T. Cantat-Gaudin, R. Carballo, T. Carlucci, J. M. Carrasco, L. Casamiquela, M. Castellani, A. Castro-Ginard, P. Charlot, L. Chemin, A. Chiavassa, G. Cocozza, G. Costigan, S. Cowell, F. Crifo, M. Crosta, C. Crowley, J. Cuypers, C. Dafonte, Y. Damerdji, A. Dapergolas, M. David, P. de Laverny, F. De Luise, R. De March, R. de Souza, A. de Torres, J. Debosscher, E. del Pozo, A. Delgado, H. E. Delgado, S. Diakite, C. Diener, E. Distefano, C. Dolding, P. Drazinos, J. Durán, B. Edvardsson, H. Enke, K. Eriksson, P. Esquej, G. Eynard Bon-temps, C. Fabre, M. Fabrizio, S. Faigler, A. J. Falcão, M. Farràs Casas, L. Federici, G. Fedorets, P. Fernique, F. Figueras, F. Filippi, K. Findeisen, A. Fonti, E. Fraile, M. Fraser, M. Gai, S. Galleti, D. Garabato, F. García-Sedano, A. Garofalo, N. Garralda, A. Gavel, P. Gavras, J. Gerssen, R. Geyer, P. Giacobbe, G. Gilmore, S. Girona, G. Giuffrida, F. Glass, M. Gomes, A. Gueguen,

## Bibliography

---

- A. Guerrier, R. Gutié, R. Haigron, D. Hatzidimitriou, M. Hauser, M. Haywood, U. Heiter, A. Helmi, J. Heu, T. Hilger, D. Hobbs, W. Hofmann, G. Holland , H. E. Huckle, A. Hypki, V. Icardi, K. Janßen, G. Jevardat de Fombelle, P. G. Jonker, Á. L. Juhász, F. Julbe, A. Karampelas, A. Kewley, J. Klar, A. Kochoska, R. Kohley, K. Kolenberg, M. Kontizas, E. Kontizas, S. E. Koposov, G. Kordopatis, Z. Kostrzewska-Rutkowska, P. Koubsky, S. Lambert, A. F. Lanza, Y. Lasne, J. B. Lavigne, Y. Le Fustec, C. Le Poncin-Lafitte, Y. Lebreton, S. Leccia, N. Leclerc, I. Lecoeur-Taibi, H. Lenhardt, F. Leroux, S. Liao, E. Licata, H. E. P. Lindstrøm, T. A. Lister, E. Livanou, A. Lobel, M. López, S. Managau, R. G. Mann, G. Mantelet, O. Marchal, J. M. Marchant, M. Marconi, S. Marinoni, G. Marschalkó, D. J. Marshall, M. Martino, G. Marton, N. Mary, D. Massari, G. Matijević, T. Mazeh, P. J. McMillan, S. Messina, D. Michalik, N. R. Millar, D. Molina, R. Molinaro, L. Molnár, P. Montegriffo, R. Mor, R. Morbidelli, T. Morel, D. Morris, A. F. Mulone, T. Muraveva, I. Musella, G. Nelemans, L. Nicastro, L. Noval, W. O'Mullane, D. Ordóñez-Blanco, P. Osborne, C. Pagani, I. Pagano, F. Pailler, H. Palacin, L. Palaversa, A. Panahi, M. Pawlak, A. M. Piersimoni, F. X. Pineau, E. Plachy, G. Plum, E. Poggio, A. Prša, L. Pulone, E. Racero, S. Ragaini, N. Rambaux, M. Ramos-Lerate, S. Regibo, C. Reylé, F. Riclet, V. Ripepi, A. Riva, A. Rivard, G. Rixon, T. Roegiers, M. Roelens, M. Romero-Gómez, N. Rowell, F. Royer, L. Ruiz-Dern, G. Sadowski, T. Sagristà Sellés, J. Sahlmann, J. Salgado, E. Salguero, N. Sanna, T. Santana-Ros, M. Sarasso, H. Savietto, M. Schultheis, E. Sciacca, M. Segol, J. C. Segovia, D. Ségransan, I. C. Shih, L. Siltala, A. F. Silva, R. L. Smart, K. W. Smith, E. Solano, F. Solitro, R. Sordo, S. Soria Nieto, J. Souchay, A. Spagna, U. Stampa, I. A. Steele, H. Steidelmüller, C. A. Stephenson, H. Stoev, F. F. Suess, J. Surdej, L. Szabados, E. Szegedi-Elek, D. Tapiador, F. Taris, G. Tauran, M. B. Taylor, R. Teixeira, D. Terrett, P. Teyssand ier, A. Titarenko, F. Torra Clotet, C. Turon, A. Ulla, E. Utrilla, S. Uzzi, M. Vaillant, G. Valentini, V. Valette, A. van Elteren, E. Van Hemelryck, M. van Leeuwen, M. Vaschetto, A. Vecchiato, J. Veljanoski, Y. Viala, D. Vicente, S. Vogt, C. von Essen, H. Voss, V. Votruba, S. Voutsinas, M. Weiler, O. Wertz, T. Wevers, Ł. Wyrzykowski, A. Yoldas, M. Žerjal, H. Ziaeepour, J. Zorec, S. Zschocke, S. Zucker, C. Zurbach and T. Zwitter, *Gaia Data Release 2. Observations of solar system objects*, **616**, A13 (2018).
- [17] Gaia Collaboration, A. G. A. Brown, A. Vallenari, T. Prusti, J. H. J. de Bruijne, C. Babusiaux, C. A. L. Bailer-Jones, M. Biermann, D. W. Evans, L. Eyer and et al., *Gaia Data Release 2. Summary of the contents and survey properties*, **616**, A1 (2018).
- [18] Gaia Helpdesk, *Gaia DR2 primer: Everything you wish you had known before you started working with Gaia Data Release 2, issue 1.0* (2019), [view 20. 12. 2019].
- [19] G. M. De Silva, K. C. Freeman, J. Bland-Hawthorn, S. Martell, E. W. de Boer, M. Asplund, S. Keller, S. Sharma, D. B. Zucker, T. Zwitter, B. Anguiano, C. Bacigalupo, D. Bayliss, M. A. Beavis, M. Bergemann, S. Campbell, R. Cannon, D. Carollo, L. Casagrande, A. R. Casey, G. Da Costa, V. D’Orazi, A. Dotter, L. Duong, A. Heger, M. J. Ireland, P. R. Kafle, J. Kos, J. Lattanzio,

- G. F. Lewis, J. Lin, K. Lind, U. Munari, D. M. Nataf, S. O'Toole, Q. Parker, W. Reid, K. J. Schlesinger, A. Sheinis, J. D. Simpson, D. Stello, Y.-S. Ting, G. Traven, F. Watson, R. Wittenmyer, D. Yong and M. Žerjal, *The GALAH survey: scientific motivation*, **449**, 2604 (2015).
- [20] K. Freeman and J. Bland-Hawthorn, *The New Galaxy: Signatures of Its Formation*, **40**, 487 (2002).
- [21] S. C. Barden, D. J. Jones, S. I. Barnes, J. Heijmans, A. Heng, G. Knight, D. R. Orr, G. A. Smith, V. Churilov, J. Brzeski, L. G. Waller, K. Shortridge, A. J. Horton, D. Mayfield, R. Haynes, D. M. Haynes, D. Whittard, M. Goodwin, S. Smedley, I. Saunders, P. R. Gillingham, E. Penny, T. J. Farrell, M. Vuong, R. Heald, S. Lee, R. Muller, K. Freeman, J. Bland-Hawthorn, D. F. Zucker and G. De Silva, *HERMES: revisions in the design for a high-resolution multi-element spectrograph for the AAT*, in *Ground-based and Airborne Instrumentation for Astronomy III*, , Vol. 7735 (2010) p. 773509.
- [22] A. Sheinis, B. Anguiano, M. Asplund, C. Bacigalupo, S. Barden, M. Birchall, J. Bland-Hawthorn, J. Brzeski, R. Cannon, D. Carollo, S. Case, A. Casey, V. Churilov, C. Warrick, R. Dean, G. De Silva, V. D'Orazi, L. Duong, T. Farrell, K. Fiegert, K. Freeman, F. Gabriella, L. Gers, M. Goodwin, D. Gray, A. Green, R. Heald, J. Heijmans, M. Ireland, D. Jones, P. Kafle, S. Keller, U. Klauser, Y. Kondrat, J. Kos, J. Lawrence, S. Lee, S. Mali, S. Martell, D. Mathews, D. Mayfield, S. Miziarski, R. Muller, N. Pai, R. Patterson, E. Penny, D. Orr, K. Schlesinger, S. Sharma, K. Shortridge, J. Simpson, S. Smedley, G. Smith, D. Stafford, N. Staszak, M. Vuong, L. Waller, E. W. de Boer, P. Xavier, J. Zheng, R. Zhelem, D. Zucker and T. Zwitter, *First light results from the High Efficiency and Resolution Multi-Element Spectrograph at the Anglo-Australian Telescope*, *Journal of Astronomical Telescopes, Instruments, and Systems* **1**, 035002 (2015).
- [23] R. A. Wittenmyer, S. Sharma, D. Stello, S. Buder, J. Kos, M. Asplund, L. Duong, J. Lin, K. Lind, M. Ness, T. Zwitter, J. Horner, J. Clark, S. R. Kane, D. Huber, J. Bland-Hawthorn, A. R. Casey, G. M. De Silva, V. D'Orazi, K. Freeman, S. Martell, J. D. Simpson, D. B. Zucker, B. Anguiano, L. Casagrande, J. Esdaile, M. Hon, M. Ireland, P. R. Kafle, S. Khanna, J. P. Marshall, M. H. M. Saddon, G. Traven and D. Wright, *The K2-HERMES Survey. I. Planet-candidate Properties from K2 Campaigns 1-3*, **155**, 84 (2018).
- [24] S. Sharma, D. Stello, S. Buder, J. Kos, J. Bland-Hawthorn, M. Asplund, L. Duong, J. Lin, K. Lind, M. Ness, D. Huber, T. Zwitter, G. Traven, M. Hon, P. R. Kafle, S. Khanna, H. Saddon, B. Anguiano, A. R. Casey, K. Freeman, S. Martell, G. M. De Silva, J. D. Simpson, R. A. Wittenmyer and D. B. Zucker, *The TESS-HERMES survey data release 1: high-resolution spectroscopy of the TESS southern continuous viewing zone*, **473**, 2004 (2018).
- [25] J. Kos, J. Lin, T. Zwitter, M. Žerjal, S. Sharma, J. Bland-Hawthorn, M. Asplund, A. R. Casey, G. M. De Silva, K. C. Freeman, S. L. Martell, J. D. Simpson, K. J. Schlesinger, D. Zucker, B. Anguiano, C. Bacigalupo, T. R. Bedding, C. Betters, G. Da Costa, L. Duong, E. Hyde, M. Ireland, P. R.

## Bibliography

---

- Kafle, S. Leon-Saval, G. F. Lewis, U. Munari, D. Nataf, D. Stello, C. G. Tinney, G. Traven, F. Watson and R. A. Wittenmyer, *The GALAH survey: the data reduction pipeline*, **464**, 1259 (2017).
- [26] M. F. Skrutskie, R. M. Cutri, R. Stiening, M. D. Weinberg, S. Schneider, J. M. Carpenter, C. Beichman, R. Capps, T. Chester, J. Elias, J. Huchra, J. Liebert, C. Lonsdale, D. G. Monet, S. Price, P. Seitzer, T. Jarrett, J. D. Kirkpatrick, J. E. Gizis, E. Howard, T. Evans, J. Fowler, L. Fullmer, R. Hurt, R. Light, E. L. Kopan, K. A. Marsh, H. L. McCallon, R. Tam, S. Van Dyk and S. Wheelock, *The Two Micron All Sky Survey (2MASS)*, **131**, 1163 (2006).
- [27] S. B. Howell, C. Sobeck, M. Haas, M. Still, T. Barclay, F. Mullally, J. Troeltzsch, S. Aigrain, S. T. Bryson, D. Caldwell, W. J. Chaplin, W. D. Cochran, D. Huber, G. W. Marcy, A. Miglio, J. R. Najita, M. Smith, J. D. Twicken and J. J. Fortney, *The K2 Mission: Characterization and Early Results*, **126**, 398 (2014).
- [28] G. R. Ricker, J. N. Winn, R. Vanderspek, D. W. Latham, G. Á. Bakos, J. L. Bean, Z. K. Berta-Thompson, T. M. Brown, L. Buchhave, N. R. Butler, R. P. Butler, W. J. Chaplin, D. Charbonneau, J. Christensen-Dalsgaard, M. Clampin, D. Deming, J. Doty, N. De Lee, C. Dressing, E. W. Dunham, M. Endl, F. Fressin, J. Ge, T. Henning, M. J. Holman, A. W. Howard, S. Ida, J. M. Jenkins, G. Jernigan, J. A. Johnson, L. Kaltenegger, N. Kawai, H. Kjeldsen, G. Laughlin, A. M. Levine, D. Lin, J. J. Lissauer, P. MacQueen, G. Marcy, P. R. McCullough, T. D. Morton, N. Narita, M. Paegert, E. Palle, F. Pepe, J. Pepper, A. Quirrenbach, S. A. Rinehart, D. Sasselov, B. Sato, S. Seager, A. Sozzetti, K. G. Stassun, P. Sullivan, A. Szentgyorgyi, G. Torres, S. Udry and J. Villasenor, *Transiting Exoplanet Survey Satellite (TESS)*, Journal of Astronomical Telescopes, Instruments, and Systems **1**, 014003 (2015).
- [29] P. de Laverny, A. Recio-Blanco, C. C. Worley and B. Plez, *The AMBRE project: A new synthetic grid of high-resolution FGKM stellar spectra*, **544**, A126 (2012).
- [30] J. A. Valenti and N. Piskunov, *Spectroscopy made easy: A new tool for fitting observations with synthetic spectra.*, **118**, 595 (1996).
- [31] N. Piskunov and J. A. Valenti, *Spectroscopy Made Easy: Evolution*, **597**, A16 (2017).
- [32] U. Munari, K. Cotar, V. Andreoli, S. Dallaporta and L. N. Yalyalieva, *Recent developments in optical spectra of nova AT 2019qwf (Nova V2891 Cyg)*, The Astronomer's Telegram **13340**, 1 (2019).
- [33] U. Munari, V. Joshi, D. P. K. Banerjee, K. Čotar, S. Y. Shugarov, Jurdana-Šepić, R. , R. Belligoli, A. Bergamini, M. Graziani, G. L. Righetti, A. Vagozzi and P. Valisa, *The 2018 eruption and long-term evolution of the new high-mass Herbig Ae/Be object Gaia-18azl = VES 263*, **488**, 5536 (2019).
- [34] D. Raghavan, H. A. McAlister, T. J. Henry, D. W. Latham, G. W. Marcy, B. D. Mason, D. R. Gies, R. J. White and T. A. ten Brummelaar, *A Survey of Stellar Families: Multiplicity of Solar-type Stars*, **190**, 1 (2010).

- [35] G. Duchêne and A. Kraus, *Stellar Multiplicity*, **51**, 269 (2013).
- [36] M. Moe and R. Di Stefano, *Mind Your Ps and Qs: The Interrelation between Period ( $P$ ) and Mass-ratio ( $Q$ ) Distributions of Binary Stars*, **230**, 15 (2017).
- [37] A. Tokovinin, *From Binaries to Multiples. II. Hierarchical Multiplicity of F and G Dwarfs*, **147**, 87 (2014).
- [38] C. F. Quist and L. Lindegren, *Statistics of Hipparcos binaries: probing the 1-10 AU separation range*, **361**, 770 (2000).
- [39] D. Pourbaix, A. A. Tokovinin, A. H. Batten, F. C. Fekel, W. I. Hartkopf, H. Levato, N. I. Morrell, G. Torres and S. Udry,  $S_{B<sup>9</sup>}:$  *The ninth catalogue of spectroscopic binary orbits*, **424**, 727 (2004).
- [40] G. Matijević, T. Zwitter, U. Munari, O. Bienaymé, J. Binney, J. Bland-Hawthorn, C. Boeche, R. Campbell, K. C. Freeman, B. Gibson, G. Gilmore, E. K. Grebel, A. Helmi, J. F. Navarro, Q. A. Parker, G. M. Seabroke, A. Siebert, A. Siviero, M. Steinmetz, F. G. Watson, M. Williams and R. F. G. Wyse, *Double-lined Spectroscopic Binary Stars in the Radial Velocity Experiment Survey*, **140**, 184 (2010).
- [41] M. A. Fernandez, K. R. Covey, N. De Lee, S. D. Chojnowski, D. Nidever, R. Ballantyne, M. Cottaar, N. Da Rio, J. B. Foster, S. R. Majewski, M. R. Meyer, A. M. Reyna, G. W. Roberts, J. Skinner, K. Stassun, J. C. Tan, N. Troup and G. Zasowski, *IN-SYNC VI. Identification and Radial Velocity Extraction for 100+ Double-Lined Spectroscopic Binaries in the APOGEE/IN-SYNC Fields*, **129**, 084201 (2017).
- [42] T. Merle, S. Van Eck, A. Jorissen, M. Van der Swaelmen, T. Masseron, T. Zwitter, D. Hatzidimitriou, A. Klutsch, D. Pourbaix, R. Blomme, C. C. Worley, G. Sacco, J. Lewis, C. Abia, G. Traven, R. Sordo, A. Bragaglia, R. Smiljanic, E. Pancino, F. Damiani, A. Hourihane, G. Gilmore, S. Randich, S. Koposov, A. Casey, L. Morbidelli, E. Franciosini, L. Magrini, P. Jofre, M. T. Costado, R. D. Jeffries, M. Bergemann, A. C. Lanzafame, A. Bayo, G. Carraro, E. Flaccomio, L. Monaco and S. Zaggia, *The Gaia-ESO Survey: double-, triple-, and quadruple-line spectroscopic binary candidates*, **608**, A95 (2017).
- [43] A. Duquennoy and M. Mayor, *Multiplicity among solar-type stars in the solar neighbourhood. II - Distribution of the orbital elements in an unbiased sample*, **248**, 485 (1991).
- [44] B. Nordström, M. Mayor, J. Andersen, J. Holmberg, F. Pont, B. R. Jørgensen, E. H. Olsen, S. Udry and N. Mowlavi, *The Geneva-Copenhagen survey of the Solar neighbourhood. Ages, metallicities, and kinematic properties of 14 000 F and G dwarfs*, **418**, 989 (2004).
- [45] G. Matijević, T. Zwitter, O. Bienaymé, J. Bland-Hawthorn, K. C. Freeman, G. Gilmore, E. K. Grebel, A. Helmi, U. Munari, J. F. Navarro, Q. A. Parker, W. Reid, G. M. Seabroke, A. Siebert, A. Siviero, M. Steinmetz, F. G. Watson, M. Williams and R. F. G. Wyse, *Single-lined Spectroscopic Binary Star Candidates in the RAVE Survey*, **141**, 200 (2011).

## Bibliography

---

- [46] N. W. Troup, D. L. Nidever, N. De Lee, J. Carlberg, S. R. Majewski, M. Fernandez, K. Covey, S. D. Chojnowski, J. Pepper, D. T. Nguyen, K. Stassun, D. C. Nguyen, J. P. Wisniewski, S. W. Fleming, D. Bizyaev, P. M. Frinchaboy, D. A. García-Hernández, J. Ge, F. Hearty, S. Meszaros, K. Pan, C. Allende Prieto, D. P. Schneider, M. D. Shetrone, M. F. Skrutskie, J. Wilson and O. Zamora, *Companions to APOGEE Stars. I. A Milky Way-spanning Catalog of Stellar and Substellar Companion Candidates and Their Diverse Hosts*, **151**, 85 (2016).
- [47] C. Badenes, C. Mazzola, T. A. Thompson, K. Covey, P. E. Freeman, M. G. Walker, M. Moe, N. Troup, D. Nidever, C. Allende Prieto, B. Andrews, R. H. Barbá, T. C. Beers, J. Bovy, J. K. Carlberg, N. De Lee, J. Johnson, H. Lewis, S. R. Majewski, M. Pinsonneault, J. Sobeck, K. G. Stassun, G. S. Stringfellow and G. Zasowski, *Stellar Multiplicity Meets Stellar Evolution and Metallicity: The APOGEE View*, **854**, 147 (2018).
- [48] P. M. Garnavich, *Wide binary stars at the Galactic poles*, **335**, L47 (1988).
- [49] L. M. Close, H. B. Richer and D. R. Crabtree, *A complete sample of wide binaries in the solar neighborhood*, **100**, 1968 (1990).
- [50] A. Gould, J. N. Bahcall, D. Maoz and B. Yanny, *Star counts from the HST Snapshot Survey. 2: Wide binaries*, **441**, 200 (1995).
- [51] A. L. Kraus and L. A. Hillenbrand, *Unusually Wide Binaries: Are They Wide or Unusual?*, **703**, 1511 (2009).
- [52] E. J. Shaya and R. P. Olling, *Very Wide Binaries and Other Comoving Stellar Companions: A Bayesian Analysis of the Hipparcos Catalogue*, **192**, 2 (2011).
- [53] J. J. Andrews, J. Chanamé and M. A. Agüeros, *Wide binaries in Tycho-Gaia: search method and the distribution of orbital separations*, **472**, 675 (2017).
- [54] J. Coronado, M. P. Sepúlveda, A. Gould and J. Chanamé, *A distant sample of halo wide binaries from SDSS*, **480**, 4302 (2018).
- [55] S. Oh, A. M. Price-Whelan, D. W. Hogg, T. D. Morton and D. N. Spergel, *Comoving Stars in Gaia DR1: An Abundance of Very Wide Separation Comoving Pairs*, **153**, 257 (2017).
- [56] F. M. Jiménez-Esteban, E. Solano and C. Rodrigo, *A Catalog of Wide Binary and Multiple Systems of Bright Stars from Gaia-DR2 and the Virtual Observatory*, **157**, 78 (2019).
- [57] K. El-Badry, H.-W. Rix, Y.-S. Ting, D. R. Weisz, M. Bergemann, P. Cargile, C. Conroy and A.-C. Eilers, *Signatures of unresolved binaries in stellar spectra: implications for spectral fitting*, **473**, 5043 (2018).
- [58] K. El-Badry, Y.-S. Ting, H.-W. Rix, E. Quataert, D. R. Weisz, P. Cargile, C. Conroy, D. W. Hogg, M. Bergemann and C. Liu, *Discovery and characterization of 3000+ main-sequence binaries from APOGEE spectra*, **476**, 528 (2018).

- [59] A. Skopal, *Disentangling the composite continuum of symbiotic binaries. I. S-type systems*, **440**, 995 (2005).
- [60] A. Rebassa-Mansergas, B. T. Gänsicke, P. Rodríguez-Gil, M. R. Schreiber and D. Koester, *Post-common-envelope binaries from SDSS - I. 101 white dwarf main-sequence binaries with multiple Sloan Digital Sky Survey spectroscopy*, **382**, 1377 (2007).
- [61] A. Rebassa-Mansergas, A. Nebot Gómez-Morán, M. R. Schreiber, B. T. Gänsicke, A. Schwape, J. Gallardo and D. Koester, *Post-common envelope binaries from SDSS - XIV. The DR7 white dwarf-main-sequence binary catalogue*, **419**, 806 (2012).
- [62] J. Ren, A. Luo, Y. Li, P. Wei, J. Zhao, Y. Zhao, Y. Song and G. Zhao, *White-dwarf-Main-sequence Binaries Identified from the LAMOST Pilot Survey*, **146**, 82 (2013).
- [63] A. Rebassa-Mansergas, J. J. Ren, S. G. Parsons, B. T. Gänsicke, M. R. Schreiber, E. García-Berro, X.-W. Liu and D. Koester, *The SDSS spectroscopic catalogue of white dwarf-main-sequence binaries: new identifications from DR 9-12*, **458**, 3808 (2016).
- [64] C. Bergmann, M. Endl, J. B. Hearnshaw, R. A. Wittenmyer and D. J. Wright, *Searching for Earth-mass planets around  $\alpha$  Centauri: precise radial velocities from contaminated spectra*, International Journal of Astrobiology **14**, 173 (2015).
- [65] A. Widmark, B. Leistedt and D. W. Hogg, *Inferring Binary and Trinary Stellar Populations in Photometric and Astrometric Surveys*, **857**, 114 (2018).
- [66] F. R. Ferraro, E. Carretta, F. Fusi Pecci and A. Zamboni, *Binary stars in globular clusters: detection of a binary sequence in NGC 2808?*, **327**, 598 (1997).
- [67] J. Hurley and C. A. Tout, *The binary second sequence in cluster colour-magnitude diagrams*, **300**, 977 (1998).
- [68] A. P. Milone, A. F. Marino, L. R. Bedin, A. Dotter, H. Jerjen, D. Kim, D. Nardiello, G. Piotto and J. Cong, *The binary populations of eight globular clusters in the outer halo of the Milky Way*, **455**, 3009 (2016).
- [69] M. Žerjal, M. J. Ireland, T. Nordlander, J. Lin, S. Buder, L. Casagrande, K. Čotar, G. De Silva, J. Horner, S. Martell, G. Traven and T. Zwitter, *The GALAH Survey: lithium-strong KM dwarfs*, **484**, 4591 (2019).
- [70] C. N. A. Willmer, *The Absolute Magnitude of the Sun in Several Filters*, **236**, 47 (2018).
- [71] M. Ness, D. W. Hogg, H.-W. Rix, A. Y. Q. Ho and G. Zasowski, *The Cannon: A data-driven approach to Stellar Label Determination*, **808**, 16 (2015).

## Bibliography

---

- [72] S. Buder, M. Asplund, L. Duong, J. Kos, K. Lind, M. K. Ness, S. Sharma, J. Bland-Hawthorn, A. R. Casey, G. M. De Silva, V. D’Orazi, K. C. Freeman, G. F. Lewis, J. Lin, S. L. Martell, K. J. Schlesinger, J. D. Simpson, D. B. Zucker, T. Zwitter, A. M. Amarsi, B. Anguiano, D. Carollo, L. Casagrande, K. Čotar, P. L. Cottrell, G. Da Costa, X. D. Gao, M. R. Hayden, J. Horner, M. J. Ireland, P. R. Kafle, U. Munari, D. M. Nataf, T. Nordlander, D. Stello, Y.-S. Ting, G. Traven, F. Watson, R. A. Wittenmyer, R. F. G. Wyse, D. Yong, J. C. Zinn and M. Žerjal, *The GALAH Survey: second data release*, **478**, 4513 (2018).
- [73] T. Zwitter, J. Kos, A. Chiavassa, S. Buder, G. Traven, K. Čotar, J. Lin, M. Asplund, J. Bland-Hawthorn, A. R. Casey, G. De Silva, L. Duong, K. C. Freeman, K. Lind, S. Martell, V. D’Orazi, K. J. Schlesinger, J. D. Simpson, S. Sharma, D. B. Zucker, B. Anguiano, L. Casagrande, R. Collet, J. Horner, M. J. Ireland, P. R. Kafle, G. Lewis, U. Munari, D. M. Nataf, M. Ness, T. Nordlander, D. Stello, Y.-S. Ting, C. G. Tinney, F. Watson, R. A. Wittenmyer and M. Žerjal, *The GALAH survey: accurate radial velocities and library of observed stellar template spectra*, **481**, 645 (2018).
- [74] A. Kunder, G. Kordopatis, M. Steinmetz, T. Zwitter, P. J. McMillan, L. Casagrande, H. Enke, J. Wojno, M. Valentini, C. Chiappini, G. Matijević, A. Siviero, P. de Laverny, A. Recio-Blanco, A. Bijaoui, R. F. G. Wyse, J. Binney, E. K. Grebel, A. Helmi, P. Jofre, T. Antoja, G. Gilmore, A. Siebert, B. Famaey, O. Bienaymé, B. K. Gibson, K. C. Freeman, J. F. Navarro, U. Munari, G. Seabroke, B. Anguiano, M. Žerjal, I. Minchev, W. Reid, J. Bland-Hawthorn, J. Kos, S. Sharma, F. Watson, Q. A. Parker, R.-D. Scholz, D. Burton, P. Cass, M. Hartley, K. Fiegert, M. Stupar, A. Ritter, K. Hawkins, O. Gerhard, W. J. Chaplin, G. R. Davies, Y. P. Elsworth, M. N. Lund, A. Miglio and B. Mosser, *The Radial Velocity Experiment (RAVE): Fifth Data Release*, **153**, 75 (2017).
- [75] A. A. Henden, S. Levine, D. Terrell and D. L. Welch, *APASS - The Latest Data Release*, in *American Astronomical Society Meeting Abstracts #225*, American Astronomical Society Meeting Abstracts, Vol. 225 (2015) p. 336.16.
- [76] E. L. Wright, P. R. M. Eisenhardt, A. K. Mainzer, M. E. Ressler, R. M. Cutri, T. Jarrett, J. D. Kirkpatrick, D. Padgett, R. S. McMillan, M. Skrutskie, S. A. Stanford, M. Cohen, R. G. Walker, J. C. Mather, D. Leisawitz, T. N. Gautier, III, I. McLean, D. Benford, C. J. Lonsdale, A. Blain, B. Mendez, W. R. Irace, V. Duval, F. Liu, D. Royer, I. Heinrichsen, J. Howard, M. Shannon, M. Kendall, A. L. Walsh, M. Larsen, J. G. Cardon, S. Schick, M. Schwalm, M. Abid, B. Fabinsky, L. Naes and C.-W. Tsai, *The Wide-field Infrared Survey Explorer (WISE): Mission Description and Initial On-orbit Performance*, **140**, 1868 (2010).
- [77] G. N. Lance and W. T. Williams, *Mixed-Data Classificatory Programs I - Agglomerative Systems.*, Australian Computer Journal **1**, 15 (1967).
- [78] D. W. Evans, M. Riello, F. De Angeli, J. M. Carrasco, P. Montegriffo, C. Fabricius, C. Jordi, L. Palaversa, C. Diener, G. Busso, C. Cacciari, F. van Leeuwen,

- P. W. Burgess, M. Davidson, D. L. Harrison, S. T. Hodgkin, E. Pancino, P. J. Richards, G. Altavilla, L. Balaguer-Núñez, M. A. Barstow, M. Bellazzini, A. G. A. Brown, M. Castellani, G. Cocozza, F. De Luise, A. Delgado, C. Ducourant, S. Galleti, G. Gilmore, G. Giuffrida, B. Holl, A. Kewley, S. E. Koposov, S. Marinoni, P. M. Marrese, P. J. Osborne, A. Piersimoni, J. Portell, L. Pulone, S. Ragagni, N. Sanna, D. Terrett, N. A. Walton, T. Wevers and Ł. Wyrzykowski, *Gaia Data Release 2. Photometric content and validation*, **616**, A4 (2018).
- [79] L. Casagrande and D. A. VandenBerg, *On the use of Gaia magnitudes and new tables of bolometric corrections*, **479**, L102 (2018).
- [80] C. A. L. Bailer-Jones, J. Rybizki, M. Fouesneau, G. Mantelet and R. Andrae, *Estimating Distance from Parallaxes. IV. Distances to 1.33 Billion Stars in Gaia Data Release 2*, **156**, 58 (2018).
- [81] L. Capitanio, R. Lallement, J. L. Vergely, M. Elyajouri and A. Monreal-Ibero, *Three-dimensional mapping of the local interstellar medium with composite data*, **606**, A65 (2017).
- [82] E. F. Schlafly and D. P. Finkbeiner, *Measuring Reddening with Sloan Digital Sky Survey Stellar Spectra and Recalibrating SFD*, **737**, 103 (2011).
- [83] P. Marigo, L. Girardi, A. Bressan, P. Rosenfield, B. Aringer, Y. Chen, M. Dussin, A. Nanni, G. Pastorelli, T. S. Rodrigues, M. Trabucchi, S. Bladh, J. Dalcanton, M. A. T. Groenewegen, J. Montalbán and P. R. Wood, *A New Generation of PARSEC-COLIBRI Stellar Isochrones Including the TP-AGB Phase*, **835**, 77 (2017).
- [84] G. Traven, G. Matijević, T. Zwitter, M. Žerjal, J. Kos, M. Asplund, J. Bland-Hawthorn, A. R. Casey, G. De Silva, K. Freeman, J. Lin, S. L. Martell, K. J. Schlesinger, S. Sharma, J. D. Simpson, D. B. Zucker, B. Anguiano, G. Da Costa, L. Duong, J. Horner, E. A. Hyde, P. R. Kafle, U. Munari, D. Nataf, C. A. Navin, W. Reid and Y.-S. Ting, *The Galah Survey: Classification and Diagnostics with t-SNE Reduction of Spectral Information*, **228**, 24 (2017).
- [85] H. Kamdar, C. Conroy, Y.-S. Ting, A. Bonaca, B. Johnson and P. Cargile, *A Dynamical Model for Clustered Star Formation in the Galactic Disk*, arXiv e-prints , arXiv:1902.10719 (2019).
- [86] H. Kamdar, C. Conroy, Y.-S. Ting, A. Bonaca, M. Smith and A. G. A. Brown, *Stars that Move Together Were Born Together*, arXiv e-prints , arXiv:1904.02159 (2019).
- [87] D. Foreman-Mackey, D. W. Hogg, D. Lang and J. Goodman, *emcee: The MCMC Hammer*, **125**, 306 (2013).
- [88] P. Eggleton, *Evolutionary Processes in Binary and Multiple Stars, by Peter Eggleton, pp. . ISBN 0521855578. Cambridge, UK: Cambridge University Press, 2006.* (2006).

## Bibliography

---

- [89] A. Tokovinin, *Comparative statistics and origin of triple and quadruple stars*, **389**, 925 (2008).
- [90] A. Tokovinin, *The Updated Multiple Star Catalog*, **235**, 6 (2018).
- [91] A. A. Tokovinin, *On the origin of binaries with twin components*, **360**, 997 (2000).
- [92] F. Arenou, X. Luri, C. Babusiaux, C. Fabricius, A. Helmi, T. Muraveva, A. C. Robin, F. Spoto, A. Vallenari, T. Antoja, T. Cantat-Gaudin, C. Jordi, N. Leclerc, C. Reylé, M. Romero-Gómez, I.-C. Shih, S. Soria, C. Barache, D. Bossini, A. Bragaglia, M. A. Breddels, M. Fabrizio, S. Lambert, P. M. Marrese, D. Massari, A. Moitinho, N. Robichon, L. Ruiz-Dern, R. Sordo, J. Veljanoski, L. Eyer, G. Jasniewicz, E. Pancino, C. Soubiran, A. Spagna, P. Tanga, C. Turon and C. Zurbach, *Gaia Data Release 2. Catalogue validation*, **616**, A17 (2018).
- [93] D. F. Evans, *Evidence for Unresolved Exoplanet-hosting Binaries in Gaia DR2*, Research Notes of the American Astronomical Society **2**, 20 (2018).
- [94] S. Sharma, J. Bland-Hawthorn, K. V. Johnston and J. Binney, *Galaxia: A Code to Generate a Synthetic Survey of the Milky Way*, **730**, 3 (2011).
- [95] A. Secchi, *Schreiben des Herrn Professors Secchi an den Herausgeber*, Astronomische Nachrichten **73**, 129 (1869).
- [96] I. Iben, Jr., *Carbon star formation and neutron-rich isotope formation in low-mass asymptotic giant branch stars*, **275**, L65 (1983).
- [97] Z. Han, P. P. Eggleton, P. Podsiadlowski and C. A. Tout, *The formation of barium and CH stars and related objects*, **277**, 1443 (1995).
- [98] J. Yoon, T. C. Beers, V. M. Placco, K. C. Rasmussen, D. Carollo, S. He, T. T. Hansen, I. U. Roederer and J. Zeanah, *Observational Constraints on First-star Nucleosynthesis. I. Evidence for Multiple Progenitors of CEMP-No Stars*, **833**, 20 (2016).
- [99] P. Battinelli, S. Demers, C. Rossi and K. S. Gigoyan, *Extension of the C Star Rotation Curve of the Milky Way to 24 kpc*, Astrophysics **56**, 68 (2013).
- [100] G. Bothun, J. H. Elias, G. MacAlpine, K. Matthews, J. R. Mould, G. Neugebauer and I. N. Reid, *Carbon stars at high Galactic latitude*, **101**, 2220 (1991).
- [101] B. Margon, S. F. Anderson, H. C. Harris, M. A. Strauss, G. R. Knapp, X. Fan, D. P. Schneider, D. E. Vanden Berk, D. J. Schlegel, E. W. Deutsch, Ž. Ivezić, P. B. Hall, B. F. Williams, A. F. Davidsen, J. Brinkmann, I. Csabai, J. J. E. Hayes, G. Hennessy, E. K. Kinney, S. J. Kleinman, D. Q. Lamb, D. Long, E. H. Neilsen, R. Nichol, A. Nitta, S. A. Snedden and D. G. York, *Faint High-Latitude Carbon Stars Discovered by the Sloan Digital Sky Survey: Methods and Initial Results*, **124**, 1651 (2002).

- [102] R. A. Downes, B. Margon, S. F. Anderson, H. C. Harris, G. R. Knapp, J. Schroeder, D. P. Schneider, D. G. York, J. R. Pier and J. Brinkmann, *Faint High-Latitude Carbon Stars Discovered by the Sloan Digital Sky Survey: An Initial Catalog*, **127**, 2838 (2004).
- [103] R. F. Griffin and R. O. Redman, *Photoelectric measurements of the  $\lambda 4200\text{ \AA}$  CN band and the G band in G8-K5 spectra*, **120**, 287 (1960).
- [104] R. D. McClure and S. van den Bergh, *Five-color intermediate-band photometry of stars, clusters, and galaxies.*, **73**, 313 (1968).
- [105] L. Häggkvist and T. Oja, *Narrow-band photometry of late-type stars*, **1**, 199 (1970).
- [106] D. Moro and U. Munari, *The Asiago Database on Photometric Systems (ADPS). I. Census parameters for 167 photometric systems*, **147**, 361 (2000).
- [107] M. Fiorucci and U. Munari, *The Asiago Database on Photometric Systems (ADPS). II. Band and reddening parameters*, **401**, 781 (2003).
- [108] N. Christlieb, P. J. Green, L. Wisotzki and D. Reimers, *The stellar content of the Hamburg/ESO survey II. A large, homogeneously-selected sample of high latitude carbon stars*, **375**, 366 (2001).
- [109] P. Green, *Innocent Bystanders: Carbon Stars from the Sloan Digital Sky Survey*, **765**, 12 (2013).
- [110] Y. S. Lee, T. C. Beers, T. Masseron, B. Plez, C. M. Rockosi, J. Sobeck, B. Yanny, S. Lucatello, T. Sivarani, V. M. Placco and D. Carollo, *Carbon-enhanced Metal-poor Stars in SDSS/SEGUE. I. Carbon Abundance Estimation and Frequency of CEMP Stars*, **146**, 132 (2013).
- [111] W. Ji, W. Cui, C. Liu, A. Luo, G. Zhao and B. Zhang, *Carbon Stars from LAMOST DR2 Data*, **226**, 1 (2016).
- [112] Y.-B. Li, A.-L. Luo, C.-D. Du, F. Zuo, M.-X. Wang, G. Zhao, B.-W. Jiang, H.-W. Zhang, C. Liu, L. Qin, R. Wang, B. Du, Y.-X. Guo, B. Wang, Z.-W. Han, M.-S. Xiang, Y. Huang, B.-Q. Chen, J.-J. Chen, X. Kong, W. Hou, Y.-H. Song, Y.-F. Wang, K.-F. Wu, J.-N. Zhang, Y. Zhang, Y.-F. Wang, Z.-H. Cao, Y.-H. Hou and Y.-H. Zhao, *Carbon Stars Identified from LAMOST DR4 Using Machine Learning*, **234**, 31 (2018).
- [113] J. E. Norris, S. G. Ryan and T. C. Beers, *Extremely Metal-poor Stars. IV. The Carbon-rich Objects*, **488**, 350 (1997).
- [114] W. Aoki, J. E. Norris, S. G. Ryan, T. C. Beers and H. Ando, *The Chemical Composition of Carbon-rich, Very Metal Poor Stars: A New Class of Mildly Carbon Rich Objects without Excess of Neutron-Capture Elements*, **567**, 1166 (2002).
- [115] R. Cayrel, E. Depagne, M. Spite, V. Hill, F. Spite, P. François, B. Plez, T. Beers, F. Primas, J. Andersen, B. Barbuy, P. Bonifacio, P. Molaro and B. Nordström, *First stars V - Abundance patterns from C to Zn and supernova yields in the early Galaxy*, **416**, 1117 (2004).

## Bibliography

---

- [116] P. S. Barklem, N. Christlieb and T. C. Beers, *Metal-poor star abundances from the HERES project*, in *13th Cambridge Workshop on Cool Stars, Stellar Systems and the Sun*, ESA Special Publication, Vol. 560, edited by F. Favata, G. A. J. Hussain and B. Battrick (2005) p. 433.
- [117] J. G. Cohen, A. McWilliam, S. Shectman, I. Thompson, N. Christlieb, J. Melendez, S. Ramirez, A. Swensson and F.-J. Zickgraf, *Carbon Stars in the Hamburg/ESO Survey: Abundances*, **132**, 137 (2006).
- [118] W. Aoki, T. C. Beers, N. Christlieb, J. E. Norris, S. G. Ryan and S. Tsangarides, *Carbon-enhanced Metal-poor Stars. I. Chemical Compositions of 26 Stars*, **655**, 492 (2007).
- [119] J. E. Norris, N. Christlieb, A. J. Korn, K. Eriksson, M. S. Bessell, T. C. Beers, L. Wisotzki and D. Reimers, *HE 0557-4840: Ultra-Metal-Poor and Carbon-Rich*, **670**, 774 (2007).
- [120] J. K. Hollek, A. Frebel, I. U. Roederer, C. Sneden, M. Shetrone, T. C. Beers, S. Kang and C. Thom, *The Chemical Abundances of Stars in the Halo (CASH) Project. II. A Sample of 14 Extremely Metal-poor Stars*, **742**, 54 (2011).
- [121] D. Yong, J. E. Norris, M. S. Bessell, N. Christlieb, M. Asplund, T. C. Beers, P. S. Barklem, A. Frebel and S. G. Ryan, *The Most Metal-poor Stars. II. Chemical Abundances of 190 Metal-poor Stars Including 10 New Stars with [Fe/H] = -3.5*, **762**, 26 (2013).
- [122] I. U. Roederer, G. W. Preston, I. B. Thompson, S. A. Shectman, C. Sneden, G. S. Burley and D. D. Kelson, *A Search for Stars of Very Low Metal Abundance. VI. Detailed Abundances of 313 Metal-poor Stars*, **147**, 136 (2014).
- [123] T. Hansen, C. J. Hansen, N. Christlieb, T. C. Beers, D. Yong, M. S. Bessell, A. Frebel, A. E. García Pérez, V. M. Placco, J. E. Norris and M. Asplund, *An Elemental Assay of Very, Extremely, and Ultra-metal-poor Stars*, **807**, 173 (2015).
- [124] H. R. Jacobson, S. Keller, A. Frebel, A. R. Casey, M. Asplund, M. S. Bessell, G. S. Da Costa, K. Lind, A. F. Marino, J. E. Norris, J. M. Peña, B. P. Schmidt, P. Tisserand, J. M. Walsh, D. Yong and Q. Yu, *High-Resolution Spectroscopic Study of Extremely Metal-Poor Star Candidates from the SkyMapper Survey*, **807**, 171 (2015).
- [125] J. G. Cohen, N. Christlieb, I. Thompson, A. McWilliam, S. Shectman, D. Reimers, L. Wisotzki and E. Kirby, *Normal and Outlying Populations of the Milky Way Stellar Halo at [Fe/H] -2*, **778**, 56 (2013).
- [126] T. C. Beers, G. W. Preston and S. A. Shectman, *A search for stars of very low metal abundance. II*, **103**, 1987 (1992).
- [127] S. Rossi, T. C. Beers and C. Sneden, *Carbon Abundances for Metal-Poor Stars Based on Medium-Resolution Spectra*, in *The Third Stromlo Symposium: The Galactic Halo*, Astronomical Society of the Pacific Conference Series, Vol. 165, edited by B. K. Gibson, R. S. Axelrod and M. E. Putman (1999) p. 264.

- [128] J. G. Cohen, S. Shectman, I. Thompson, A. McWilliam, N. Christlieb, J. Melendez, F.-J. Zickgraf, S. Ramírez and A. Swenson, *The Frequency of Carbon Stars among Extremely Metal-poor Stars*, **633**, L109 (2005).
- [129] S. Lucatello, S. Tsangarides, T. C. Beers, E. Carretta, R. G. Gratton and S. G. Ryan, *The Binary Frequency Among Carbon-enhanced, s-Process-rich, Metal-poor Stars*, **625**, 825 (2005).
- [130] S. Rossi, T. C. Beers, C. Sneden, T. Sevastyanenko, J. Rhee and B. Marsteller, *Estimation of Carbon Abundances in Metal-Poor Stars. I. Application to the Strong G-Band Stars of Beers, Preston, and Shectman*, **130**, 2804 (2005).
- [131] A. Frebel, N. Christlieb, J. E. Norris, T. C. Beers, M. S. Bessell, J. Rhee, C. Fechner, B. Marsteller, S. Rossi, C. Thom, L. Wisotzki and D. Reimers, *Bright Metal-poor Stars from the Hamburg/ESO Survey. I. Selection and Follow-up Observations from 329 Fields*, **652**, 1585 (2006).
- [132] B. E. Marsteller, *The frequency of carbon-enhanced metal-poor stars and the origin of carbon in the universe*, Ph.D. thesis, Michigan State University (2007).
- [133] D. Carollo, T. C. Beers, J. Bovy, T. Sivarani, J. E. Norris, K. C. Freeman, W. Aoki, Y. S. Lee and C. R. Kennedy, *Carbon-enhanced Metal-poor Stars in the Inner and Outer Halo Components of the Milky Way*, **744**, 195 (2012).
- [134] D. Yong, J. E. Norris, M. S. Bessell, N. Christlieb, M. Asplund, T. C. Beers, P. S. Barklem, A. Frebel and S. G. Ryan, *The Most Metal-poor Stars. III. The Metallicity Distribution Function and Carbon-enhanced Metal-poor Fraction*, **762**, 27 (2013).
- [135] V. M. Placco, A. Frebel, T. C. Beers and R. J. Stancliffe, *Carbon-enhanced Metal-poor Star Frequencies in the Galaxy: Corrections for the Effect of Evolutionary Status on Carbon Abundances*, **797**, 21 (2014).
- [136] J. Yoon, T. C. Beers, S. Dietz, Y. S. Lee, V. M. Placco, G. Da Costa, S. Keller, C. I. Owen and M. Sharma, *Galactic Archeology with the AEGIS Survey: The Evolution of Carbon and Iron in the Galactic Halo*, **861**, 146 (2018).
- [137] T. Suda, M. Aikawa, M. N. Machida, M. Y. Fujimoto and I. Iben, Jr., *Is HE 0107-5240 A Primordial Star? The Characteristics of Extremely Metal-Poor Carbon-Rich Stars*, **611**, 476 (2004).
- [138] E. Starkenburg, M. D. Shetrone, A. W. McConnachie and K. A. Venn, *Binarity in carbon-enhanced metal-poor stars*, **441**, 1217 (2014).
- [139] H. Umeda and K. Nomoto, *First-generation black-hole-forming supernovae and the metal abundance pattern of a very iron-poor star*, **422**, 871 (2003).
- [140] H. Umeda and K. Nomoto, *Variations in the Abundance Pattern of Extremely Metal-Poor Stars and Nucleosynthesis in Population III Supernovae*, **619**, 427 (2005).

## Bibliography

---

- [141] N. Tominaga, N. Iwamoto and K. Nomoto, *Abundance Profiling of Extremely Metal-poor Stars and Supernova Properties in the Early Universe*, **785**, 98 (2014).
- [142] P. Banerjee, Y.-Z. Qian and A. Heger, *s-Process in Massive Carbon-Enhanced Metal-Poor Stars*, 10.1093/mnras/sty2251 (2018).
- [143] D. Carollo, K. Freeman, T. C. Beers, V. M. Placco, J. Tumlinson and S. L. Martell, *Carbon-enhanced Metal-poor Stars: CEMP-s and CEMP-no Subclasses in the Halo System of the Milky Way*, **788**, 180 (2014).
- [144] M. A. Cruz, H. Cogo-Moreira and S. Rossi, *Searching for chemical classes among metal-poor stars using medium-resolution spectroscopy*, **475**, 4781 (2018).
- [145] T. C. Beers and N. Christlieb, *The Discovery and Analysis of Very Metal-Poor Stars in the Galaxy*, **43**, 531 (2005).
- [146] M. Spite, E. Caffau, P. Bonifacio, F. Spite, H.-G. Ludwig, B. Plez and N. Christlieb, *Carbon-enhanced metal-poor stars: the most pristine objects?*, **552**, A107 (2013).
- [147] J. K. Hollek, A. Frebel, V. M. Placco, A. I. Karakas, M. Shetrone, C. Sneden and N. Christlieb, *The Chemical Abundances of Stars in the Halo (CASH) Project. III. A New Classification Scheme for Carbon-enhanced Metal-poor Stars with s-process Element Enhancement*, **814**, 121 (2015).
- [148] L. Duong, K. C. Freeman, M. Asplund, L. Casagrande, S. Buder, K. Lind, M. Ness, J. Bland-Hawthorn, G. M. De Silva, V. D’Orazi, J. Kos, G. F. Lewis, J. Lin, S. L. Martell, K. Schlesinger, S. Sharma, J. D. Simpson, D. B. Zucker, T. Zwitter, B. Anguiano, G. S. Da Costa, E. Hyde, J. Horner, P. R. Kafle, D. M. Nataf, W. Reid, D. Stello, Y.-S. Ting and R. F. G. Wyse, *The GALAH survey: properties of the Galactic disc(s) in the solar neighbourhood*, **476**, 5216 (2018).
- [149] R. A. Wittenmyer, S. L. Martell, J. Esdaile, S. Sharma and D. Stello, *The HERMES K2 Follow-up Program at the Anglo-Australian Telescope*, in *American Astronomical Society Meeting Abstracts #227*, American Astronomical Society Meeting Abstracts, Vol. 227 (2016) p. 138.16.
- [150] R. C. Johnson, *The Structure and Origin of the Swan Band Spectrum of Carbon*, Philosophical Transactions of the Royal Society of London Series A **226**, 157 (1927).
- [151] L. van der Maaten and G. Hinton, *Visualizing Data using t-SNE*, Journal of Machine Learning Research **9**, 2579 (2008).
- [152] J. Sperauskas, L. Začs, W. J. Schuster and V. Deveikis, *The Binary Nature of CH-Like Stars*, **826**, 85 (2016).
- [153] J. Bergeat, A. Knapik and B. Rutily, *The pulsation modes and masses of carbon-rich long period variables*, **390**, 987 (2002).

- [154] T. Lloyd Evans, *Carbon stars*, Journal of Astrophysics and Astronomy **31**, 177 (2010).
- [155] P. Battinelli and S. Demers, *Variability of halo carbon stars*, **544**, A10 (2012).
- [156] P. Battinelli and S. Demers, *The variability of carbon stars in the Sagittarius dwarf spheroidal galaxy*, **553**, A93 (2013).
- [157] P. Battinelli and S. Demers, *Miras among C stars*, **568**, A100 (2014).
- [158] B. Margon, T. Kupfer, K. Burdge, T. A. Prince, S. R. Kulkarni and D. L. Shupe, *The Binary Dwarf Carbon Star SDSS J125017.90+252427.6*, **856**, L2 (2018).
- [159] D. S. P. Dearborn, J. Liebert, M. Aaronson, C. C. Dahn, R. Harrington, J. Mould and J. L. Greenstein, *On the nature of the dwarf carbon star G77-61*, **300**, 314 (1986).
- [160] L. J. Whitehouse, J. Farihi, P. J. Green, T. G. Wilson and J. P. Subasavage, *Dwarf carbon stars are likely metal-poor binaries and unlikely hosts to carbon planets*, **479**, 3873 (2018).
- [161] J. Farihi, A. R. Arendt, H. S. Machado and L. J. Whitehouse, *Evidence for halo kinematics among cool carbon-rich dwarfs*, **477**, 3801 (2018).
- [162] T. T. Hansen, J. Andersen, B. Nordström, T. C. Beers, V. M. Placco, J. Yoon and L. A. Buchhave, *The role of binaries in the enrichment of the early Galactic halo. II. Carbon-enhanced metal-poor stars: CEMP-no stars*, **586**, A160 (2016).
- [163] C. Abia, H. M. J. Boffin, J. Isern and R. Rebolo, *IY Hya - A new super Li-rich carbon star*, **245**, L1 (1991).
- [164] I.-J. Sackmann, R. L. Smith and K. H. Despain, *Carbon and eruptive stars: surface enrichment of lithium, carbon, nitrogen, and  $^{13}C$  by deep mixing.*, **187**, 555 (1974).
- [165] P. C. Keenan and W. W. Morgan, *The Classification of the Red Carbon Stars.*, **94**, 501 (1941).
- [166] C. Barnbaum, R. P. S. Stone and P. C. Keenan, *A Moderate-Resolution Spectral Atlas of Carbon Stars: R, J, N, CH, and Barium Stars*, **105**, 419 (1996).
- [167] A. Alksnis, A. Balklavs, U. Dzervitis, I. Eglitis, O. Paupers and I. Pundure, *General Catalog of Galactic Carbon Stars by C. B. Stephenson. Third Edition*, Baltic Astronomy **10**, 1 (2001).
- [168] Y. Komiya, T. Suda, H. Minaguchi, T. Shigeyama, W. Aoki and M. Y. Fujimoto, *The Origin of Carbon Enhancement and the Initial Mass Function of Extremely Metal-poor Stars in the Galactic Halo*, **658**, 367 (2007).
- [169] T. Masseron, J. A. Johnson, B. Plez, S. van Eck, F. Primas, S. Goriely and A. Jorissen, *A holistic approach to carbon-enhanced metal-poor stars*, **509**, A93 (2010).

## Bibliography

---

- [170] V. M. Placco, C. R. Kennedy, S. Rossi, T. C. Beers, Y. S. Lee, N. Christlieb, T. Sivarani, D. Reimers and L. Wisotzki, *A Search for Unrecognized Carbon-Enhanced Metal-Poor Stars in the Galaxy*, **139**, 1051 (2010).
- [171] C. Abate, O. R. Pols, R. G. Izzard and A. I. Karakas, *Carbon-enhanced metal-poor stars: a window on AGB nucleosynthesis and binary evolution. II. Statistical analysis of a sample of 67 CEMP-s stars*, **581**, A22 (2015).
- [172] J. Yoon, T. C. Beers, V. M. Placco, K. C. Rasmussen, D. Carollo, S. He, T. T. Hansen, I. U. Roederer and J. Zeanah, *VizieR Online Data Catalog: Carbon-enhanced metal-poor (CEMP) star abundances (Yoon+, 2016)*, VizieR Online Data Catalog **183** (2017).
- [173] Gaia Collaboration, A. G. A. Brown, A. Vallenari, T. Prusti, J. H. J. de Bruijne, C. Babusiaux, C. A. L. Bailer-Jones, M. Biermann, D. W. Evans, L. Eyer and et al., *Gaia Data Release 2. Summary of the contents and survey properties*, **616**, A1 (2018).
- [174] J. Bovy, *galpy: A python Library for Galactic Dynamics*, **216**, 29 (2015).
- [175] H. Koppelman, A. Helmi and J. Veljanoski, *One Large Blob and Many Streams Frosting the nearby Stellar Halo in GaiaDR2*, **860**, L11 (2018).
- [176] R. D. McClure and A. W. Woodsworth, *The binary nature of the barium and CH stars. III - Orbital parameters*, **352**, 709 (1990).
- [177] A. Jorissen, S. Van Eck, H. Van Winckel, T. Merle, H. M. J. Boffin, J. Andersen, B. Nordström, S. Udry, T. Masseron, L. Lenaerts and C. Waelkens, *Binary properties of CH and carbon-enhanced metal-poor stars*, **586**, A158 (2016).

## Appendix A

### Naslov prvega dodatka



# Razširjeni povzetek v slovenskem jeziku

Razširjeni povzetek v slovenskem jeziku naj bo dolg vsaj 10 strani. Vključuje naj tudi slike, tabele in enačbe, ki so nujne za razumevanje besedila povzetka.